An Estimation of the Impact of Climate Change on Solar Resources

For Photovoltaic and Concentrating Solar Power Applications

Isabelle Huber

München 2012

An Estimation of the Impact of Climate Change on Solar Resources

For Photovoltaic and Concentrating Solar Power Applications

Diplomarbeit
an der Fakultät für Physik
der Ludwig-Maximilians-Universität
München

vorgelegt von
Isabelle Huber
aus Ulm

München, den 14. April 2012

Erstgutachter: Prof. Dr. Bernhard Mayer, *Meteorologisches Institut* (LMU)
Zweitgutachter: Dr. Luca Bugliaro, *Institut für Physik der Atmosphäre* (DLR)

Contents

Acknowledgements

This thesis would have never been possible without the continuous support of Bernhard Mayer, *Ludwig-Maximilians-Universität* (LMU), and Luca Bugliaro, *Deutsches Zentrum für Luft- und Raumfahrt* (DLR). Their sharing of expertise as well as their patience are deeply appreciated.
I owe my special gratitude to Michael Ponater (DLR) and Hella Garny (DLR) who were there with help and advice when unexpected problems with the global climate model data arose. I am particularly thankful that they set up and tested new climate model simulations for this work.
Further thanks go to Philipp Stier, *University of Oxford*, for furnishing the aerosol data set, and to Claudia Emde (LMU) and Kaspar Graf (DLR) for their patient help in programming questions. Finally, I would like to express my gratitude to all members of department 3 of the DLR *Institute of Atmospheric Physics* for many fruitful discussions.

Abstract

Solar power plants convert the energy of solar radiation into electrical energy. There are two different technologies that are "fueled" by two distinct radiation quantities: photovoltaic panels use global horizontal irradiance (GHI) to produce electricity whereas concentrating solar power plants are fueled by direct normal irradiance (DNI). Therefore, these two radiation quantities are an important factor when selecting suitable sites for solar power generation. Global climate model (GCM) simulations provide a projection of the future amount of global horizontal irradiance, but climate models are not designed to compute direct irradiances. In this work a method was developed to add direct irradiance to the output of global climate model simulations: after the model simulations radiative transfer calculations were performed with the modeled atmosphere data.

A composite of clouds modeled by a DLR version of the GCM ECHAM4 (Stenke *et al.*, 2009) and aerosols modeled by an ECHAM5 version (Kloster *et al.*, 2006) that was interactively coupled to the aerosol module HAM (Stier *et al.*, 2005) was chosen as input for the radiative transfer calculations. In order to produce cloud data that is suitable for offline calculations of direct irradiance, a new method was implemented in the ECHAM4 radiation code. ECHAM4 now calculates online an effective cloud optical depth that describes all clouds of the cloud-covered part of a model grid box.

The calculations produced a data set of global horizontal and direct normal irradiances for the years 1995 - 1999 and 2035 - 2039. The temporal resolution is 6-hourly and the horizontal resolution is approximately 3.75° latitude x 3.75° longitude. The data set has been named ISMAD (**I**rradiances at the **S**urface derived from **M**odeled **A**tmosphere **D**ata).

According to the ISMAD data set highest local noon irradiances are located in the Saharan region. A comparison between future (2035 - 2039) and past (1995 - 1999) 5-yearly mean values reveals a significant reduction of direct normal irradiance in West and Southern Africa (-23 % and -20 % respectively) due to an increased aerosol optical depth. In the Saharan region the future DNI is 11 % smaller than the corresponding past value (not significant). In Australia ISMAD provides higher future irradiances (GHI 5 % and DNI 7 %, not significant). A reduction of clouds could be identified as the cause of this increase. Globally, the ISMAD method projects a reduction of GHI (-2 %) and DNI (-5 %).

1 Introduction: Why an Estimation of Future Irradiances?

Climate change concerns coupled with increasing oil prices and the resulting need to transform industries leads governments to support renewable energies. By early 2010, more than 100 countries had implemented some type of policy target and/or promotion policy related to renewable energy; this compares with 55 countries in early 2005. In both Europe and the United States, renewables accounted for over half of the newly installed power capacity in 2009. In the same year, renewables comprised one quarter of the global power capacity from all sources and delivered 19 % of all global electricity supply. [1] The growth of renewable energy experiences a continuing upward trend (Renewable Energy Policy Network for the 21st Century, 2010).

This development in the energy sector leads to new questions and challenges. In contrast to conventional energy sources like fossil fuels, the electricity production by solar and wind power plants cannot be controlled by burning more or less fuel and thereby adjust the energy production to the consumption. Their electricity production varies in time due to the high natural variability of their "fuels" solar radiation and wind. Power plant operators, who need to know the future energy yield of their power plants, and electrical grid providers (who have to stabilize the grid) are required to address this issue.

The question of the "fuel" variability was handed from economy to science and gave rise to the new scientific field of the so-called energy meteorology whose main challenge is to provide radiation and wind maps with reasonable temporal and spatial resolutions. For the purposes of a power plant operator, there are two different reasonable map resolutions: On the one hand, short-term information about the solar and wind resources is important to be able to negotiate at the energy stock market, where production surpluses can be sold and bottlenecks can be bridged by additional purchases. Spatial resolutions down to the size of the power plant and temporal resolutions down to hours and minutes for the next hours ("intra-day") or the next day ("day-ahead") are required. Energy meteorologists apply for instance weather forecast models or cloud cameras to provide such data. On the other

[1] counting as renewables: traditional biomass (13 %, growing slowly or even declining in some regions), hydropower (3.4 %, growing modestly), other renewables like modern biomass, wind, solar, geothermal and biofuels (2.6 %, growing very rapidly in developed countries and some developing countries).

hand, the site selection for solar or wind power plants demands knowledge about how sunny or windy the designated spots are in the long term. This information is needed as input for power plant simulations that project the future energy yield, depending on the site-conditions and the technical specifications of the power plant. For solar energy applications long-term radiation data sets are provided by several data bases: The *European Solar Radiation Atlas* (586 ground stations in Europe) (Scharmer *et al.*, 2000) and *meteonorm* (>2400 ground stations, global) (Meteonorm, 2012) derive their data from ground measurements. Examples of data sets derived from satellite-based measurements are *Satellight* (Foyntonont *et al.*, 1997), SOLEMI (Mayer *et al.*, 2004), and ISIS (Lohmann, 2006). Typically, these data sets provide radiation quantities for time periods over several years with an hourly temporal resolution. Spatial resolutions highly differ by region and data base.
There are two types of solar power plants which are fueled by two different radiation quantities: Photovoltaic panels are fueled by the so-called global irradiance, i.e. the radiation incident from all directions on the panel. In contrast, concentrating solar power systems use the direct irradiance that is the radiation coming from the direction of the Sun only. Not every data base provides information about the direct irradiance.

Figure 1.1: Left side: photovoltaic panel. Right side: concentrating solar power system.

What all data bases do have in common is that the provided data is derived from measurements. Applying measured radiation data as input to power plant simulations and thus for the projection of the future energy yield implies the assumption that the future global or direct irradiance will be the same as in the past. Taking climate change into account makes this assumption questionable.

This work aims to provide an estimation of future solar energy relevant radiation quantities. Information about the future development of global horizontal irradiance (GHI) is nothing new, as GHI is standard output of global climate model simulations. But direct normal irradiance (DNI) is not provided by global climate model runs because climate modelers are

interested in energy budgets, and direct irradiance - as only a part of the total radiative energy - is not relevant to them. In this work a method was developed to derive global as well as direct irradiance from global climate model (GCM) data: radiative transfer calculations were performed on atmospheric data provided by global climate models. We distinguish between online and offline calculations. The term "online calculation" refers to a calculation that is performed by a GCM during its run. In contrast, the term "offline calculation" refers to a calculation that is done independently of the GCM run, but using data produced by the GCM run as input. Global and direct irradiances at the Earth's surface depend on the amount of clouds, aerosols, gases etc. in the atmosphere. Such information about the atmosphere is calculated online by a GCM. The atmospheric data that had been calculated online were taken to perform offline calculations of global and direct irradiance.
A global data set of GHI and DNI for the years 1995-1999 and 2035-2039 was produced and regional 5-yearly mean values of the future time period were compared to the corresponding 5-yearly mean values of the past time period. It was not aimed at producing a data set that is suitable for power plant simulations and that could be used instead of measurement-derived irradiances. The spatio-temporal resolution of the climate model atmospheric data is not high enough for this purpose and modeled data cannot replace measurement-derived data sets. No model perfectly reproduces the system being modeled. When modelling future time periods, additional uncertainties arise from the need to make an assumption about the future emission scenarios. Thus, the objective of this work is to provide an estimation of future changes of GHI and DNI that in addition to power plant-simulations can be useful for the site selection of solar power plants.

This work is structured as follows: It starts with an introduction to radiative transfer theory, photovoltaics and concentrating solar power (chapter 2). In chapter 3, the method of this work is explained: We take a closer look at the global climate models and the simulation set-ups that produced the atmospheric data used for the offline radiative transfer calculations, and these atmospheric data are presented. A method to calculate online 2D cloud properties suitable for offline calculations of direct irradiance is introduced. Next, the offline calculations are described. In order to check if the offline solution method of the radiative transfer equation is consistent with the method applied for the online calculations, the offline calculated GHI is compared to the online calculated GHI. The offline calculated GHI and DNI for the years 1995-1999 are then compared to irradiance data derived from satellite-measurements (Lohmann, 2006, ISIS). The data set produced by the offline calculations is presented and discussed in chapter 4. Chapter 5 finally contains a summary and an outlook to possible further studies.

2 Physical Background: Radiative Transfer Theory

To write a chapter about the physical background of radiative transfer is quite challenging: Radiative transfer theory applies results from various areas of physics as electromagnetism, optics, quantum mechanics, atomic and molecular physics, solid state physics and thermodynamics and statistics. Any attempt to present this work's physical background in detail within the framework of a diploma thesis must fail. Consequently, the aim of this chapter is to simply provide an overview of the basic concepts of radiative transfer that are needed in this work. For details, it has to be referred to textbooks. For the sake of fluent reading well-known equations and facts won't be referenced. In order to present the basic concepts of radiative transfer, in the following the Sun's radiation is accompanied from its origin in the Sun over its journey through the Earth's atmosphere to its absorption in a solar power plant. But first we take a look at what energy and in particular radiative energy are in physical terms.

2.1 Radiative energy

Energy exists in many different forms, e.g. as heat, chemical or electrical energy. Even mass is known as energy since Albert Einstein stated $E = mc^2$ in 1905 and light as electromagnetic radiation is a form of energy, too. An important property of radiation is its ability to transfer energy. The axiomatic **law of conservation of energy** says that its total amount in an isolated system remains constant over time. It can neather be created nor be destroyed, it can only be transformed. In the public discussion the term energy is commonly used to refer to electrical energy. This is an expression for potential energy caused by the electrical force described by Coulomb's law and energy newly derived from it (like the kinetic energy of electrons in a conductor). An advantage of energy in its electrical state is that it can easily be transformed into other kinds; electricity is a very versatile form of energy. As an example: when a lamp is plugged in, potential energy in the socket transforms into kinetic energy of the electrons in the cable, which partly turns into radiation in the bulb. Electrical energy is usable energy. This is the reason why power plants convert other than electrical

forms of energy into electrical energy.
Nearly all energy on Earth is brought here by the Sun's radiation.[1] Fossil fuels for instance stored the energy of the Sun's radiation as chemical energy. Burning them is an exothermic reaction and sets the energy free again (and produces CO_2). Wind as kinetic energy of air particles originates from pressure differences in the atmosphere that are a result of air temperature differences caused by the Sun's radiation etc.

Physics knows different ways to describe radiation. In radiative transfer as applied in this work, the simplest and therefore best description of radiation is that of a beam of photons. A photon's energy content $e(\nu)$ is determined by the frequency ν of the corresponding electromagnetic wave via the relationship

$$e(\nu) = h\nu \quad [\mathrm{J}]\,, \tag{1}$$

where $h = 6.62606957 \,\mathrm{x}\, 10^{-34}\,\mathrm{Js}$ denotes Planck's constant. h has units of physical action, i.e., energy [J] times time [s]. The frequency of the wave is connected to its wavelength λ by

$$\nu = \frac{c}{\lambda} \quad [\mathrm{s}^{-1} = \mathrm{Hz}]\,, \tag{2}$$

where $c = 3 \,\mathrm{x}\, 10^8\,\mathrm{ms}^{-1}$ denotes the photon's velocity through vacuum.
To describe all photons unambiguously at time t the photons' distribution in the six dimensional ($\mathbf{r}$, $\mathbf{\Omega}$, ν)-space is needed. Three coordinates of the position vector $\mathbf{r}$ give the photon position in geometrical space, two angles characterize the flight direction $\mathbf{\Omega}$ (the absolute value of the photons' velocity $\mathbf{v}$ is given by the speed of light c) and the frequency ν determines the photon's energy by equation (1). A differential expression for the directions a photon at $\mathbf{r}$ could fly to is needed in order to define the photons' distribution function. Therefore, consider a sphere with radius $\tilde{r}$ in the photon's local spherical ($\tilde{r}$, ϑ, φ)-coordinate system, see figure 2.1. The **solid angle** Ω is defined by

$$\Omega = \frac{A}{\tilde{r}^2} \quad [\mathrm{m}^2\mathrm{m}^{-2} = \mathrm{sr}]\,, \tag{3}$$

where A denotes an area on the sphere. Ω is a measure for all the directions from $\mathbf{r}$ into space that cross A. The division by $\tilde{r}^2$ cancelles out the dependency of A on the radius of the sphere. The full solid angle, i.e. $A = 4\pi\tilde{r}^2$, is $4\pi \approx 12.57\,\mathrm{sr}$. The differential expression for

[1] other "sources" are geothermal energy (= energy that originates from the original formation of the planet, from radioactive decay of minerals and from volcanic activity) and tidal energy (= kinetic energy of the oceans generated by periodic variations in gravitational attraction exerted by celestial bodies).

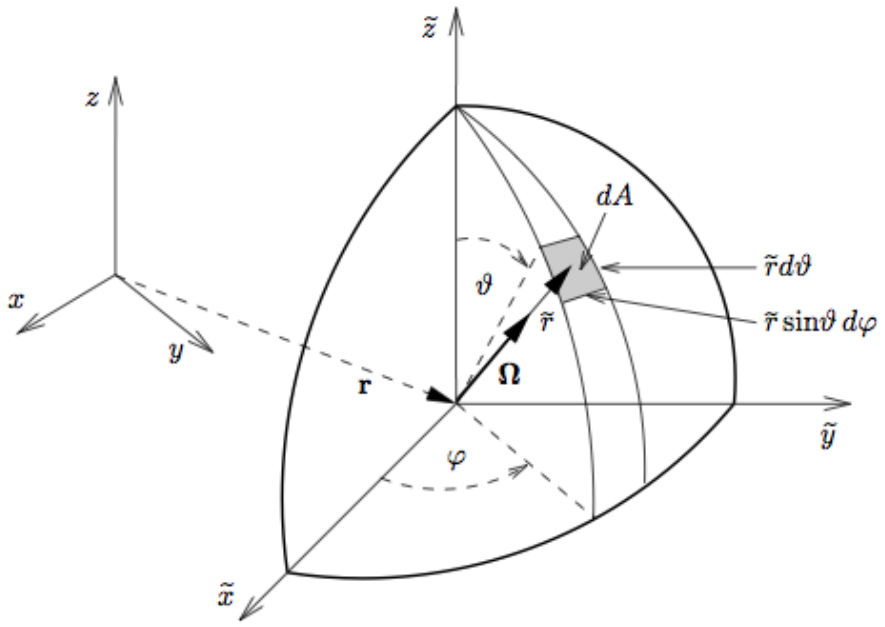

Figure 2.1: Position vector $\mathbf{r}$ and solid angle Ω. Definition of the local spherical $(\tilde{r}, \vartheta, \varphi)$-coordinate system and the direction $\mathbf{\Omega}$.
Source: Zdunkowski *et al.* (2007).

the directions a photon at $\mathbf{r}$ could fly to is described by the differential solid angle element

$$d\Omega = \frac{dA}{\tilde{r}^2} = \frac{1}{\tilde{r}^2}\,\tilde{r}^2\, sin\vartheta\, d\vartheta\, d\varphi = sin\vartheta\, d\vartheta\, d\varphi\,. \tag{4}$$

Here, $dA = \tilde{r}^2\, sin\vartheta\, d\vartheta\, d\varphi$ is the differential area element on the sphere with radius $\tilde{r}$. The distribution function of photons $f(\nu, \mathbf{r}, \mathbf{\Omega}, t) = f_\nu(\mathbf{r}, \mathbf{\Omega}, t)$ can now be defined as

$$N_\nu(\mathbf{r}, \mathbf{\Omega}, t)\, d\nu = f_\nu(\mathbf{r}, \mathbf{\Omega}, t)\, dV\, d\Omega\, d\nu\,, \tag{5}$$

where $N_\nu\, d\nu$ represents the number of photons at time t contained within the volume element dV centered at $\mathbf{r}$, flying into a direction within the solid angle element $d\Omega$ about the flight direction $\mathbf{\Omega}$, with frequencies within the interval $(\nu, \nu + d\nu)$. We are not interested in the number of the photons but in the energy they transport. For this reason the **radiance** $I_\nu(\mathbf{r}, \mathbf{\Omega}, t)$ is defined by

$$I_\nu(\mathbf{r}, \mathbf{\Omega}, t) = ch\nu f_\nu(\mathbf{r}, \mathbf{\Omega}, t) \tag{6}$$

as the product of the energy density $h\nu f_\nu(\mathbf{r}, \mathbf{\Omega}, t)$ and the velocity c. From this equation it can be seen that the monochromatic radiance is expressed in units [$\mathrm{Wm^{-2}sr^{-1}Hz^{-1}}$]. The

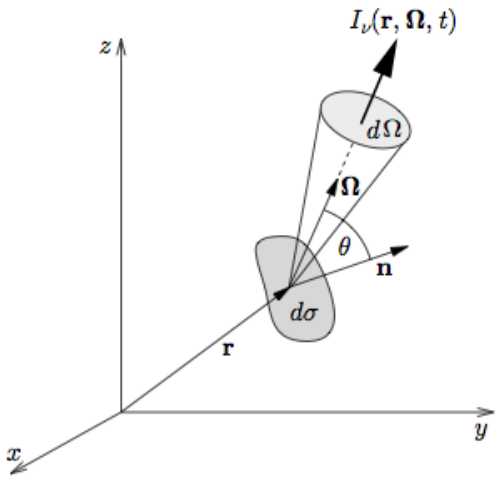

Figure 2.2: Radiative energy streaming through the infinitesimal surface element $d\sigma$ with surface normal $\mathbf{n}$ into the solid angle element $d\Omega$ around the flight direction $\mathbf{\Omega}$ of the photons. Source: Zdunkowski *et al.* (2007).

physical meaning of the radiance can be illustrated with the help of the energy relation

$$u_\nu(\mathbf{r}, \mathbf{\Omega}, t)\, d\nu = I_\nu(\mathbf{r}, \mathbf{\Omega}, t)\, cos\theta\, d\Omega\, d\sigma\, d\nu\,. \tag{7}$$

$u_\nu\, d\nu$ is the radiant energy contained within the frequency interval $(\nu, \nu + d\nu)$ streaming during dt at $\mathbf{r}$ through the surface element $d\sigma$ with unit surface normal $\mathbf{n}$ into a direction within solid angle element $d\Omega$ around $\mathbf{\Omega}$. It is important to take into account the angle θ between the surface normal $\mathbf{n}$ and the flight direction $\mathbf{\Omega}$ (see figure 2.2) because the beam of photons coming from direction $-\mathbf{\Omega}$ "sees" the surface smaller than it is, if $\mathbf{n}$ and $\mathbf{\Omega}$ are not parallel. For the photons only that part of a surface element counts that is normal to their flight direction, i.e. $cos\theta\, d\sigma$. Radiance is a function depending on the orientation of the surface (independent only if the radiation field is isotropic).
All matter with temperatures above the theoretical temperature of absolute zero ($= 0\,\mathrm{K}$) emits radiation. For the idealized case of black body radiation, the radiance is described by the **Planck function**

$$B_\nu(T)\, d\nu = \frac{2h\nu^3}{c^2}\,(e^{h\nu/kT} - 1)^{-1}\, d\nu\,. \tag{8}$$

This function contains three fundamental constants of nature: h is Planck's constant, c is the speed of light and $k = 1.380662 \times 10^{23}\,\mathrm{JK}^{-1}$ is the Boltzmann constant. B_ν represents the energy emitted by a black unit surface area per unit time interval within a cone of solid angle $\Omega_0 = 1\,\mathrm{sr}$ vertical to the emitting surface in the frequency range between ν and $\nu + d\nu$.[2] The Planck function only depends on the temperature T of the black body and

[2]A black body is an idealized object that is realized by a cavity and the radiation field inside the cavity is

on the frequency interval. The Planck function gives a distribution for the frequencies at which the body emits radiation. According to the theorem for the change of variables in an integral, the Planck function expressed in wavelength terms is

$$B_\lambda(T)\,d\lambda = \frac{2hc^2}{\lambda^5}\,(e^{hc/\lambda kT} - 1)^{-1}\,d\lambda \tag{9}$$

and now has units [$\mathrm{Wm^{-2}}\mu\mathrm{m^{-1}sr^{-1}}$] or [$\mathrm{Wm^{-2}nm^{-1}sr^{-1}}$]. Figure 2.3 shows Planckian black body curves for various temperatures. With increasing temperature the maxima of the curves are shifted towards smaller wavelengths. This phenomenon is known as Wien's displacement law. For the Planck curves as a function of frequency (that is proportional to a photon's energy) holds: the higher the body's temperature, the higher the energy of the photons that the body emits mostly.

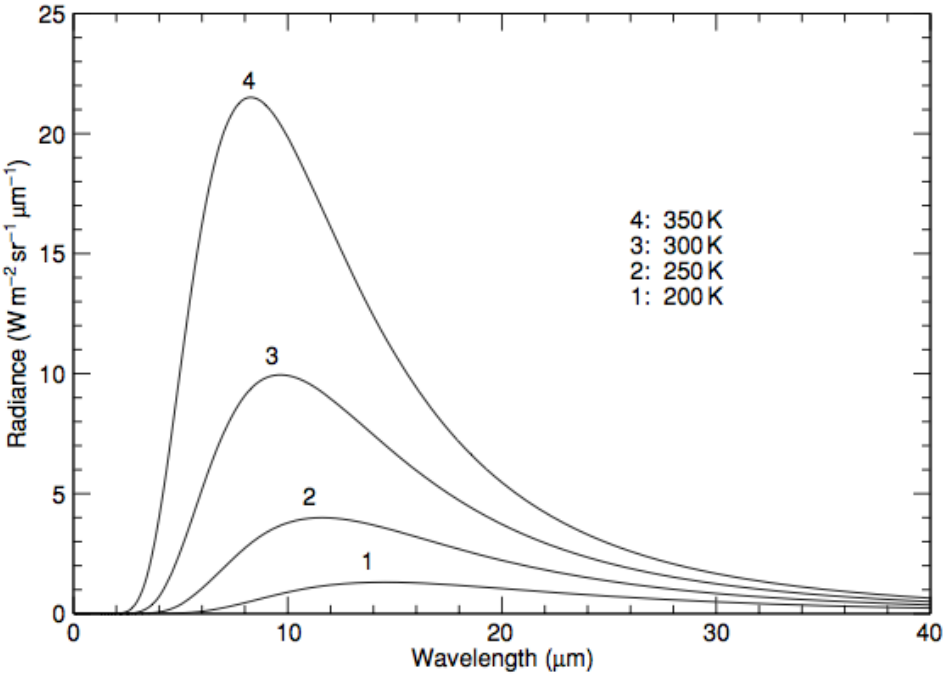

Figure 2.3: Planckian black body curves for various temperatures.
Source: Zdunkowski *et al.* (2007).

Integration of the radiance over the upper hemisphere of a surface gives the **(spectral) irradiance** (or spectral flux density) E_ν that describes the radiant energy coming from all

considered for the calculations. This field is stationary, isotropic and homogeneous (in thermodynamic equilibrium). Translation of these qualities of the radiation field inside the cavity to an emitting black body surface leads to the description in the text.

directions of that halfspace

$$E_\nu(\mathbf{r},t) = \int_{2\pi} I_\nu(\mathbf{r},\mathbf{\Omega},t)\, cos\theta\, d\Omega\,. \tag{10}$$

Irradiance again depends on the orientation of the surface. If one is not interested in the spectral resolution, integration over the frequencies gives the **(integrated) irradiance** (or flux density)

$$E(\mathbf{r},t) = \int_0^\infty E_\nu(\mathbf{r},t)\, d\nu \tag{11}$$

that describes the total radiant energy incident on a surface and is the quantity we are interested in. It is common to abbreviate the spectral and the integrated irradiance just as irradiance. Which quantity is really meant then by the term "irradiance" should be clear from the context. Let us consider an important special case: parallel radiation falls in perpendicular to a surface ($\cos\theta = 1$) and leads to the radiance $I_{\perp,\nu}$, spectral irradiance $E_{\perp,\nu}$ and integrated irradiance $E_\perp$. As parallel radiation comes from one single direction, $I_{\perp,\nu}$ and $E_{\perp,\nu}$ have the same value (but they differ by units). For a rotation of the surface such that there is the angle ϑ_0 between the surface's first and second position (and in such a way that the radiation is still incident on the same side of the surface), the radiance $I_{\perp,\nu}$, the spectral irradiance $E_{\perp,\nu}$ and the integrated irradiance $E_\perp$ on the surface's second position are

$$\begin{aligned} I_{\vartheta_0,\nu} &= I_{\perp,\nu}\, \cos\vartheta_0 \\ E_{\vartheta_0,\nu} &= E_{\perp,\nu}\, \cos\vartheta_0 \\ E_{\vartheta_0} &= E_\perp\, \cos\vartheta_0 \quad . \end{aligned} \tag{12}$$

In the last section it was highlighted that radiation is a form of energy. It can be described as a beam of photons, each photon carrying a certain amount of energy. The quantities radiance and irradiance were derived from photons flying on or through a surface. Planck's law was presented. In order to present the transfer of solar radiation through the Earth's atmosphere, we now accompany a beam of photons from their emission by the Sun to their absorption by a solar power plant (photovoltaic or concentrating) on the Earth's surface.

2.2 Emission by the Sun

In the core of the Sun, energy is set free by nuclear fusion, mainly through a series of steps called the p-p (proton-proton) chain. This process converts hydrogen ^{1}H into helium ^{4}He, i.e. mass is converted into other forms of energy (for details, see textbooks on nuclear and particle physics/astrophysics). The energy set free in the Sun's core travels through many successive layers to the Sun's surface, the photosphere. Most of that energy leaves the about

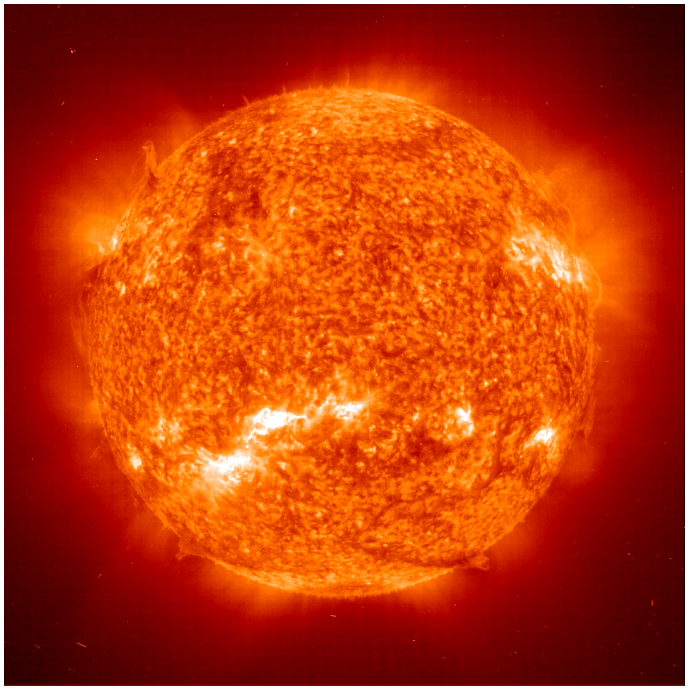

Figure 2.4: Photosphere of the Sun, about $6000K$ hot. Source: <URL: http://apod.nasa.gov/apod/image/9812/eithe_981211_big.gif> (Accessed 7/10/2011).

6000 K hot photosphere as electromagnetic radiation, as described by Planck's law. When leaving the Sun, some photons may be absorbed by colder gases like O_2, Na, He and others in the outer region of the Sun. This produces absorption lines in the black body spectrum (Fraunhofer lines). For those photons flying into the solid angle

$$\Omega_E(t) = \frac{A_E}{r_{SE}^2(t)} \tag{13}$$

now the journey to Earth begins (see figure 2.5). $r_{SE}(t)$ denotes the Sun-Earth distance. $A_E = \pi r_E^2$ is the Earth's cross-section with $r_E \approx 6370\,\text{km}$ the mean radius of the Earth. During the about eight minutes of their journey through empty space to Earth the photons keep flying in the same direction with velocity c. Due to the big Sun-Earth distance they arrive as an approximately parallel beam at the top of the Earth's atmosphere (TOA) and lead to the integrated irradiance $S(t)$ on a surface normal to their flight direction. The temporal mean value of $S(t)$ is known as solar constant $S_0 \approx 1360\,\text{Wm}^{-2}$. For each point on Earth defined by its latitude and longitude equation (12) can be applied to calculate the local horizontal irradiance I_{TOA} with ϑ_0 the angle between the local zenith and the direction of the Sun (solar zenith angle). The Earth orbits the Sun elliptically with a velocity $\approx 30\,\text{kms}^{-1}$ while rotating around a tilted axis. The annual mean distance from Sun to Earth is one astronomical unit ($\approx 150\,\text{x}\,10^6\,\text{km}$). The solar zenith angle and thus I_{TOA} depend besides

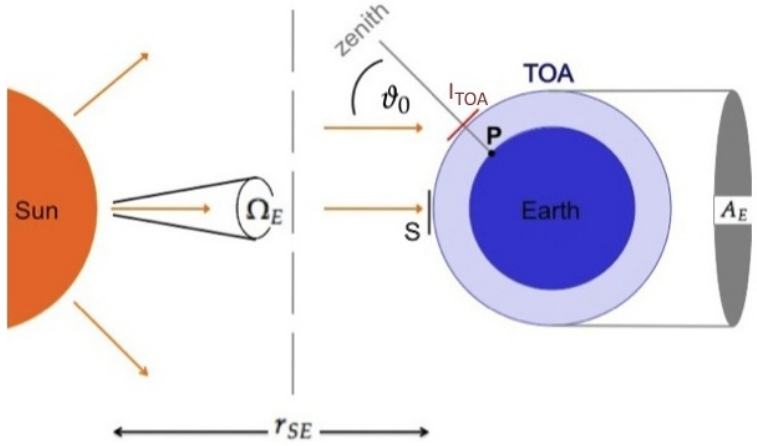

Figure 2.5: Illustration of Sun-Earth geometry.

annual variations additionally on the time of the day as they are defined on the daily rotating coordinate system of the Earth. Figure 2.6 illustrates the annual and diurnal variations

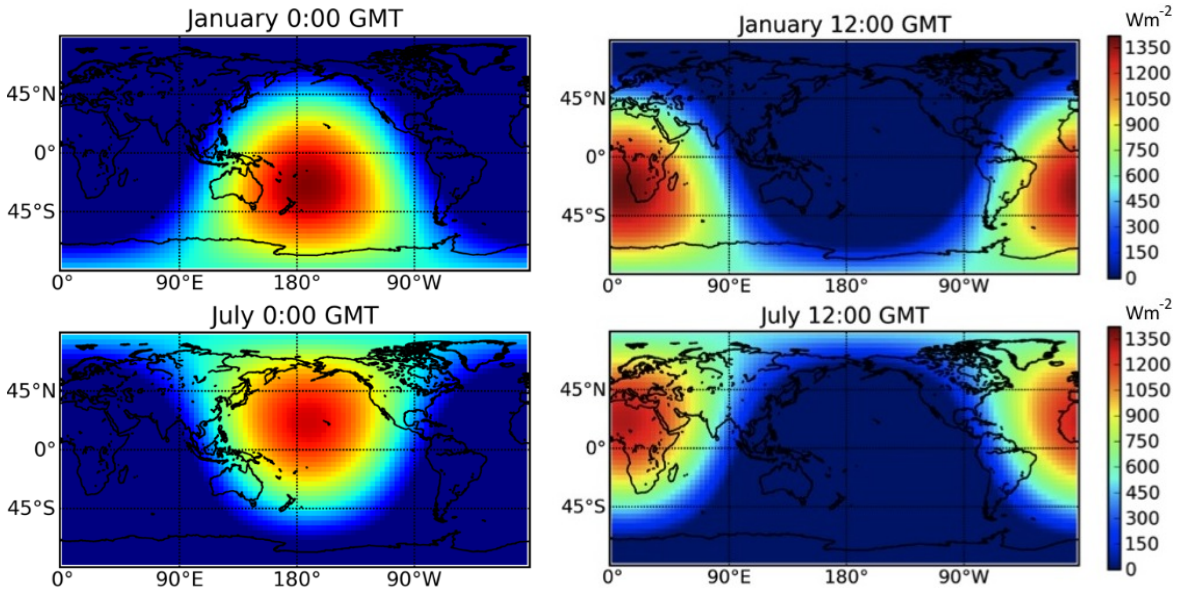

Figure 2.6: ECHAM4 Irradiance at TOA for January and July 1st 1996 at 0:00 and 12:00 GMT.

of the horizontal integrated irradiances by showing maps of modeled I_{TOA}-distributions for January and July, 00:00 and 12:00 GMT. Due to the Earth's elliptical orbit with smallest Sun-Earth distance in January, the maximal I_{TOA} is larger in January (1412 Wm^{-2}) than in July (1324 Wm^{-2}). The tilt of the Earth's rotational axis leads to an annual periodic movement of the maximal value of I_{TOA} from South to North and back, which leads for instance to the European seasons with winter in the months around January and summer in the months

around July. The rotation of the Earth causes the diurnal movement of the irradiance distribution from East to West.
There are also other (non-annual) periodic variations in $S(t)$ that are not caused by Sun-Earth geometry and are subject to research: space-based radiometric measurements in the past three decades show an eleven-year solar cycle with peak-to-peak amplitude of order 0.1 % and variations of order 0.2 % associated with the Sun's 27-day rotation period (Fröhlich & Lean, 1998).

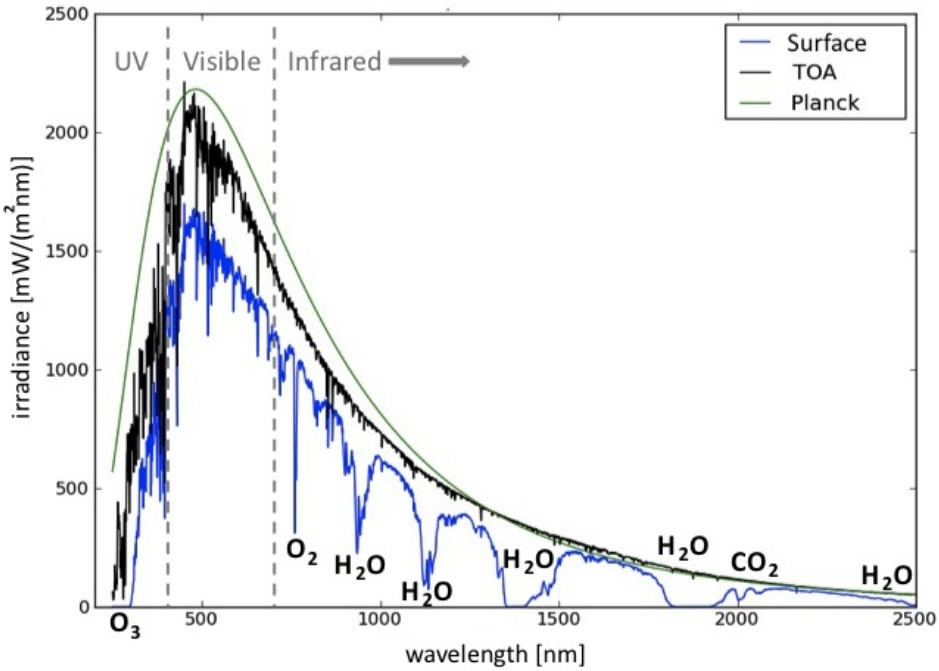

Figure 2.7: The figure shows the horizontal spectral irradiances for a solar zenith angle $\vartheta_0 = 30°$.
Green line: irradiance of a 6000 K hot black body at Sun-Earth distance.
Black line: the actual irradiance at TOA following Kurudz (1992).
Blue line: global horizontal irradiance at the surface for an atmosphere containing only gases (no clouds or aerosols); RTE was solved with discrete ordinate method algorithm provided by libRadtran (Mayer & Kylling, 2005), spectral resolution LOWTRAN (Pierluissi & Peng, 1985).

The black graph in figure 2.7 shows the horizontal (spectral) irradiance $I_{TOA,\nu}$ for a solar zenith angle $\vartheta_0 = 30°$. The structural difference to the irradiance of a 6000 K hot black body at Sun-Earth distance (green graph) is caused by the Fraunhofer lines. The systematic difference is due to the effective temperature of the Sun being a bit smaller than 6000 K. Considering the Fraunhofer lines and requiring that the total energy emitted by the Sun be the same as that of a black body, one finds that the Sun's effective temperature is 5778 K

(Thomas & Stamnes, 1999). The solar spectrum reaches from about 200 nm in the UV spectral region to about 4000 nm in the infrared. Its maximum is located in the visible part of the electromagnetic spectrum ($\approx 400 - 700$ nm). The blue graph in the figure is explained in the next section.

In the last section the horizontal irradiance I_{TOA} at the top of the atmosphere was presented. Its spectral composition roughly follows that of a 6000 K hot black body, i.e. most energy is delivered by photons of frequencies within the visible band of the spectrum. For each point (lat,lon) on Earth the magnitude of I_{TOA} mainly depends on the time of the day and the time of the year.

2.3 Scattering and absorption in the Earth's atmosphere

The solar radiation I_{TOA} now enters the Earth's atmosphere where it may interact with atmospheric particles. In this section the particles of the atmosphere, the interaction between them and solar radiation, and the mathematical description of radiative transfer through the atmosphere are presented.

2.3.1 The atmosphere

The Earth's atmosphere (from Greek atmos "vapors" and sphaira "sphere") is a mixture of gases, suspended solid and liquid particles surrounding the Earth in equilbrium between diffusion into space and gravity holding them back (weather dynamics are neglected here). Density and pressure of the atmosphere decrease with increasing altitude, with no definite boundary between the atmosphere and outer space. The average atmospheric pressure at sea level is about 1 atmosphere (atm) = 1013.25 hPa (1 hPa = 10^2 Pascal). Four atmospheric layers can be distinguished by their temperature gradient. Beginning from ground level these layers are the troposphere, the stratosphere, the mesosphere and the thermosphere. The troposphere extends to about 10 km height (depending on the latitude as the Earth is not a perfect sphere), temperature decreases with altitude. It contains about 80 % of the atmosphere's mass. The troposphere is the most turbulent part of the atmosphere (Greek: tropos "turning", "mixing"); most weather takes place here. The stratosphere derives its name from the layering effect produced by the lack of vertical mixing. It extends from about 10 km to 50 km height (again depending on the latitude). Temperature increases with height. The troposphere and stratosphere together contain about 99.9 % of our atmosphere's mass. The atmosphere beyond the stratosphere (mesosphere and thermosphere) is very thin

and interactions with radiation can be neglected for our purpose.
The description of atmospheric particles is complicated because there are so many of them. It is neither possible nor useful to consider any single particle separately. Therefore, the particles constituting the atmosphere are classified as gases, aerosols (suspensions of liquid or solid particles except for cloud particles and precipitation) and cloud particles. Each of these classes is further divided into subclasses in such a way that the microphysical properties of the elements of each subclass are similar. Then, for every subclass effective microphysical properties per atmospheric volume element are translated into macroscopic optical properties in order to quantify their influence on radiation.

2.3.2 Interaction between radiation and matter

Generally, the interaction between radiation and matter can be emission, absorption, elastic and inelastic scattering, depending firstly on the wavelength of the radiation and secondly on the matter's microphysical properties. Between solar radiation and matter contained within the atmosphere mainly absorption and elastic scattering take place.
Absorption takes place whenever a photon with energy content $e(\nu)$ meets matter that is able to take this amount of energy (for explanation see textbooks on quantum mechanics, atomic and molecular physics, solid state physics, quantum electrodynamics). If we consider a whole bunch of molecules ($N \gtrsim 10^{23}$) the macroscopic quantity "temperature" can be defined and absorption by the single molecules leads to an increase in temperature, i.e. radiative energy transforms into heat (see textbooks on thermodynamics and statistics).
Elastic scattering refers to a change of the radiation direction (but no change of energy). The change of direction is described by the **scattering phase function** $P(\mathbf{\Omega}' \rightarrow \mathbf{\Omega})$, see figure 2.8. The scattering phase function is a probability density distribution for a scattering process from the incident direction $\mathbf{\Omega}'$ into the direction $\mathbf{\Omega}$. If the scattering angle $\Theta < 90^\circ$ one speaks about forward scattering, if $\Theta > 90^\circ$ one speaks about backward scattering. The asymmetry parameter g (Zdunkowski *et al.*, 2007, equation (6.40)) describes the asymmetry between forward and backward scattering of the scattering distribution. $g = 0$ in the case of isotropic scattering, i.e. forward and backward scattering occur with the same probability. $g = 1$ or $g = -1$ for only forward or only backward scattering respectively.
Scattering mainly depends on the relation between the particle size and the wavelength. This relation is called size parameter

$$x := \frac{2\pi r}{\lambda} \,. \tag{14}$$

For particles far smaller than the wavelength ($x < 0.002$) scattering processes are negligible; for $x > 2000$ scattering can be described relatively easy by geometric optics (Petty,

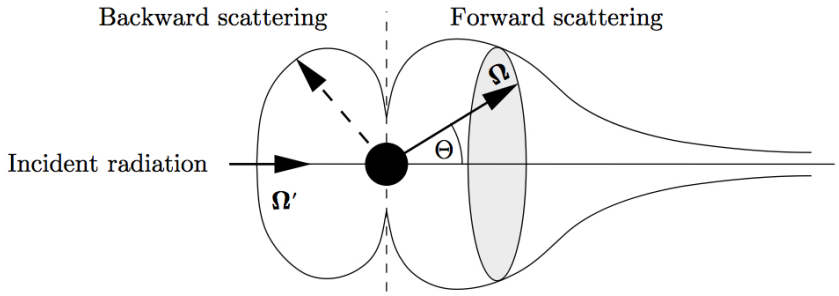

Figure 2.8: Illustration of the scattering phase function $P(\mathbf{\Omega}' \rightarrow \mathbf{\Omega})$. Source: Zdunkowski *et al.* (2007).

2006). Unfortunately, most atmospheric particles fall in between these two extremes and more complex methods are needed. Very small randomly oriented particles can be described within the framework of Raighley theory. **Raighley scattering** is symmetric and highly wavelength dependent (the scattering cross section $\propto \lambda^{-4}$). Radiation of smaller wavelengths is scattered more efficiently than radiation of bigger wavelengths; blue light is scattered more than red light. Raighley scattering of visible radiation by atmospheric molecules makes the sky blue and the Sun red. But clouds and aerosol particles like haze do not look blue but white, so another form of scattering, independent of the wavelength, does take place here. It can be described by Mie theory. Mie theory is valid for spherical particles of arbitrary size, like droplets in a water cloud. **Mie scattering** is asymmetric in forward direction. Scattering gets really complicated when particles are too big for Raighley theory and at the same time do not fulfill the condition of being spherical required by Mie theory, such as ice crystals in ice clouds. The scattering behavior of ice clouds has therefore either to be calculated seperately for each different crystal shape, measured in the laboratory or it has to be somehow else approximated.

2.3.3 GHI and DNI

The incoming radiation may be multiply scattered within the atmosphere and could then reach the surface from any direction. Therefore, it is distinguished between direct radiation which is the radiation coming from the direction of the Sun and diffuse radiation that is the radiation coming from any other direction. The sum of both is called global radiation, compare to figure 2.9. Global radiation incident on a horizontal surface is named global horizontal irradiance (GHI). Accordingly defined is the direct horizontal irradiance (DHI). Direct normal irradiance (DNI) is direct radiation incident on a surface normal to the direction of the Sun and can be calculated with DHI and the solar zenith angle ϑ_0 according

to equation (12).

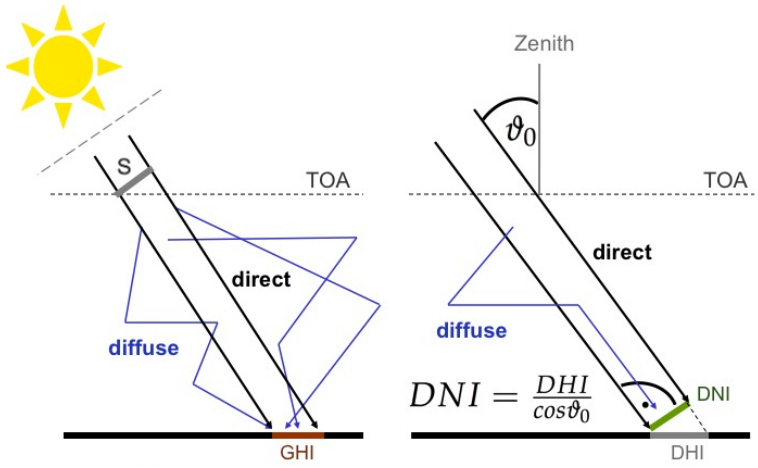

Figure 2.9: Illustration of global horizontal irradiance (GHI) and direct normal irradiance (DNI).

2.3.4 Mathematical description of radiative transfer

To make things easier for the following description of the optical properties of the atmosphere and the radiative transfer equation we make two approximations:

Plane-Parallel Approximation: The atmosphere over each point on Earth (lat,lon) is assumed to be plane and horizontally homogeneous. The microphysical properties of the particles in the atmosphere are only variable along the z-axis (in the direction of the zenith) but not horizontally. The radiation - although possibly having a horizontal component in the flight direction - experiences no horizontal variability of the atmosphere. In a plane-parallel atmosphere the only spatial variable is z. The direction of the radiation is defined by the zenith angle ϑ with respect to the z-axis and by the azimuth angle φ counted from an arbitrary origin (compare to figure 2.1; the only difference to that figure is that the position vector $\mathbf{r}$ is now the position coordinate z and the x- and y-axes are now meaningless). The length of the radiation path through the layer depends on $cos\,\vartheta =: \mu$. The path element ds is related to dz by $ds = -dz/\mu$ (the radiation path s is counted positive in the direction of the radiation; $s = 0$ at TOA). The plane-parallel approximation can be made because the vertical variations of all radiative quantities usually dominate over the horizontal variability. This does not hold in the case of radiative transfer for solar positions near or below the horizon ($85° \lesssim \vartheta_0 \lesssim 95°$).

Quasi-Static Approximation: It is assumed that the atmosphere does not undergo any variations in time while the radiation travels through it. This makes radiative transfer

independent of time and is justified by the big value of the speed of light c compared to the "reaction" times of the atmosphere.

The decrease or extinction of the radiance $I(z + dz)$ pathing along ds with direction $\mathbf{\Omega}$ through an atmospheric layer between $z + dz$ and z in a plane-parallel, quasi-static atmosphere is

$$dI = -k_{ext}(z)\ I(z + dz)\ ds\ . \tag{15}$$

The proportionality constant k_{ext} is the **extinction coefficient** that as the sum of the absorption coefficient k_{abs} and the scattering coefficient k_{sca} accounts for absorption and scattering within the atmospheric layer. For details see e.g. Zdunkowski *et al.* (2007, section 1.6). Solution of equation (15) yields the **Lambert-Beer law**

$$I(z) = I(z + dz) \exp\left(-\frac{\tau(z)}{\mu}\right) \quad \text{with} \quad \tau(z) = \int_z^{z+dz} k_{ext}(z')\ dz'\ . \tag{16}$$

$\tau(z)$ denotes the **optical depth** of the layer. Here, it is neglected that radiaton could be scattered **into** the direction $\mathbf{\Omega}$. Though, the Lambert-Beer law is a good approximation to calculate direct radiances coming from the Sun with direction $\mathbf{\Omega_0}$. The direct radiance I_{dir} at the surface at a height z_{Sur} above sea level can be calculated by

$$I_{dir}(z_{Sur}) = I_{TOA} \exp\left(-\frac{\tau}{\mu}\right) \tag{17}$$

with

$$\tau = \int_{z_{Sur}}^{z_{TOA}} k_{ext}(z)\ dz\ . \tag{18}$$

So direct radiation is relatively easy to calculate. As we are interested not only in direct but also in global radiation, we need to calculate the diffuse radiation, too. To obtain the radiance in any direction $\mathbf{\Omega}$ the **radiative transfer equation** (RTE) has to be solved. The RTE can be derived from a budget equation for the number of photons within a volume (similar to the continuity equations for mass in hydrodynamics, for volume in phase space in statistics, for probability in quantum mechanics etc.), for details see Zdunkowski *et al.* (2007); or it can be derived on the basis of geometric reasoning in the manner described by Chandrasekhar (1960). With $d\tau/\mu = -k_{ext}\, ds$ the RTE for a plane-parallel, quasi-static atmosphere reads

$$\mu \frac{d}{d\tau} I(\tau, \mu, \varphi) = I(\tau, \mu, \varphi) - I_{dif} - I_{dir} \tag{19}$$

with

$$I_{dif} = \frac{\omega_0}{4\pi} \int_0^{2\pi} \int_{-1}^{1} P(\mathbf{\Omega}' \rightarrow \mathbf{\Omega})\ I(\tau, \mu', \varphi')\ d\mu' d\varphi' \tag{20}$$

being the diffuse radiance that was scattered at least once before and is scattered from an

arbitrary direction other than the direction of the direct solar beam into the direction $\mathbf{\Omega}$ and

$$I_{dir} = \frac{\omega_0}{4\pi} P(\mathbf{\Omega_0} \rightarrow \mathbf{\Omega}) \; I_{TOA} \; exp\left(-\frac{\tau}{\mu_0}\right) \tag{21}$$

being the direct radiance that is scattered from the direction $\mathbf{\Omega_0}$ of the unscattered solar beam into the direction $\mathbf{\Omega}$. μ_0 is the cosine of the solar zenith angle ϑ_0.
ω_0 denotes the **single scattering albedo** that gives the scattering fraction with reference to the whole extinction

$$\omega_0 = \frac{k_{sca}}{k_{ext}} \; . \tag{22}$$

The RTE is an integro-differential equation that cannot be solved analytically. But there exist different approximative solution methods that are based on distinct simplifications of the problem. A very exact solution can be calculated by the discrete ordinate method that yields direction-resolved radiances. Computationally less expensive are the so-called two-stream methods where the radiation between two layers is assumed to move either in downward or upward direction ($\mu = 1$ or $\mu = -1$). Therefore, two-stream methods do not calculate radiances but irradiances. Two-stream approximations often yield unsatisfactory results because in these methods the strong forward peak of the phase function of clouds and aerosols is not accounted for (for explanation see e.g. Zdunkowski *et al.* (2007)). A distinct improvement is achieved by utilizing a delta-scaled phase function (Zdunkowski *et al.*, 2007, equation (6.1)). When solving the RTE with a two-stream method, the optical depth, the single scattering albedo and the asymmetry parameter yield sufficient information to calculate irradiances.
As the interaction between radiation and matter is wavelength dependent, all quantities defined above are. The index ν was left out for the sake of clear presentation. This means that in order to obtain integrated irradiances, in principle the RTE has to be solved for every wavelength ("line-by-line"). As this is very time consuming and not feasible for many applications, band parameterizations are applied: the solar spectrum is devided into a certain number of subbands and an average transmissivity is considered for each wavelength interval. A challenge in formulating band parameterization methods is that the absorption coefficient of atmospheric gases is highly wavelength dependent. The most accurate band parameterization method is the so-called correlated-k approximation (Lacis & Oinas, 1991; Yang *et al.*, 2000).

2.3.5 Optical properties of the atmosphere

It was already stated that for the description of the optical properties of the atmosphere, atmospheric particles are divided into classes (gases, aerosols and clouds) and further sub-

Gas	**Chemical Symbol**	$\mathbf{V_i/V = p_i/p}$	**Molar Mass** ($g\,mol^{-1}$)
Nitrogen	N_2	0.7808	28.013
Oxygen	O_2	0.2095	31.999
Argon	Ar	0.0093	39.948
Carbon Dioxide*	CO_2	$0.0004 = 400ppm$	44.010
Dry Air		1.0000	28.965
		ppm	
Neon	Ne	18	20.183
Helium	He	5.2	4.003
Methane*	CH_4	1.8	16.043
Krypton	Kr	1.1	83.80
Dihydrogen*	H_2	0.56	2.016
Nitrous Oxide*	N_2O	0.32	44.013
Carbon Monoxide*	CO	0.090	28.011
Xenon	X	0.087	131.30
Ozone*	O_3	0.040	47.995
Additionally in traces: SO_2, NO_2			

Table 2.1: Composition of tropospheric, water vapor free air ("dry air") for the year 2000. Gases labeled by * increased significantly due to anthropogenic action compared to pre-industrial times. The value of V_{CO_2}/V was about 280 ppm at pre-industrial times, V_{CH_4}/V was 0.7 ppm. Source: Kraus (2004).

classes. Then, for each subclass macroscopic optical properties (τ, g and ω_0) can be calculated with effective microphysical properties.

Atmospheric gases are divided into subclasses by their molecular structure. Table 2.1 shows the composition of dry, i.e. water vapor free, air. Apart from water vapor (H_2O) that is highly variable in space and time from 0 to 4 Vol% the concentrations of the atmospheric gases are nearly constant (Kraus, 2004). Gases have sizes of $\approx 10^{-4}\,\mu$m (Petty, 2006). Their scattering behavior can be described within Raighley theory, i.e. scattering by gases is highly wavelength dependent and the phase function is symmetric ($g \approx 0$). The blue graph in figure 2.7 shows the global horizontal irradiance at the surface for an atmosphere containing only gases (no aerosols or clouds). Some radiation is scattered back into space, which explains that the irradiance at the surface is proportionally smaller than at TOA. The structural difference between the irradiance at TOA and at the surface is due to absorption. For the most important absorption bands the chemical symbols of the absorbing gases are illustrated in the figure. For wavelengths smaller than 300 nm nearly all photons are absorbed by ozone and oxygen. In the infrared region water vapor and carbon dioxide are the most important absorbers.

Clouds are divided firstly into water and ice clouds. The distribution of both highly de-

pends on time and location. Clouds nearly do not absorb in the solar region of the electromagnetic spectrum. But multiple scattering within clouds enlarges the photon path and thereby the probabilty of absorption by gases. This way clouds may lead to higher absorption. The scattering properties of water clouds are mainly influenced by the effective size of the cloud droplets and can be described by Mie theory. The size of the single droplets may vary from about 5 to 50 μm (Petty, 2006). A typical value for the asymmetry parameter g is 0.85. The scattering behavior of ice clouds mainly depends on size and shape of the ice crystals. The ice crystals reach sizes of an order of magnitude larger than the water droplets in water clouds; depending on temperature and supersaturation of the air they may be shaped like plates, columns, needles, dendrites etc. Ice clouds are more efficient scatterers than water clouds with a typical asymmetry parameter of 0.8. Figure 2.10 shows

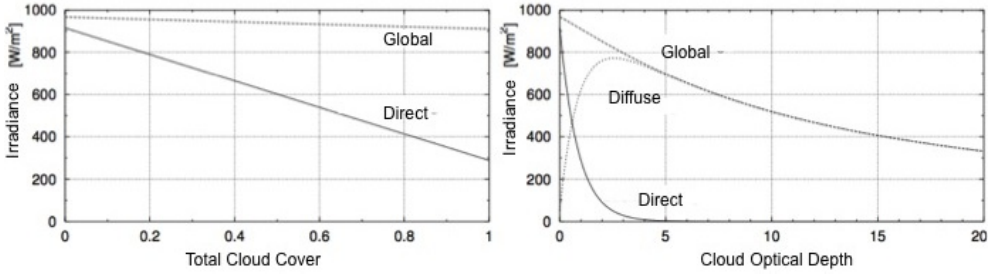

Figure 2.10: Dependency of global, diffuse and direct horizontal irradiances on clouds. Left panel: Dependency on the total cloud cover. Right panel: Dependency on the cloud optical depth. Source: (Lohmann, 2006, modified).

the impact of a water cloud on direct, diffuse and global horizontal irradiances at the surface for a solar zenith angle $\vartheta_0 = 30^\circ$ in a midlatitude summer atmosphere (for details see Lohmann (2006)). The plot on the right hand side shows the dependency on the cloud optical depth τ. The optical depth given here is its value at 550 nm and is scaled for other wavelengths accordingly. The global and the direct irradiance decrease exponentially with increasing optical depth τ. The direct irradiance becomes smaller faster than the global irradiance and vanishes for $\tau \gtrsim 5$ because the radiation is scattered out of the direction $\mathbf{\Omega_0}$ by the cloud particles. Therefore, the diffuse irradiance increases at first ($\tau \lesssim 2.5$). The first increase of the diffuse irradiance does not fully compensate the decrease of the direct irradiance, as with the longer path of the scattered radiation through the atmosphere absorbtion and scattering by atmospheric particles become more probable. Thus, the graph of the diffuse irradiance converges to the graph of the global irradiance for $2.5 \lesssim \tau \lesssim 5$ to become identical for $\tau \gtrsim 5$. On the left hand side of the figure global and direct irradiances are plotted against the total cloud cover c_{tot} for a cloud with optical depth $= 1$. c_{tot} denotes the fraction of the sky that is covered by the cloud. The global and direct irradiance decrease linearly in c_{tot}. As the optical depth influences the direct irradiance much more than the

global irradiance, the direct irradiance decreases more rapidly than the global irradiance with increasing c_{tot}.

Aerosols are commonly divided into subclasses by their size which ranges between $\approx$ 0.1 and 1 μm. Their concentrations are variable in space and time. The wavelength dependence of their scattering behavior is weak, the phase function is strongly asymmetric (Petty, 2006). Aerosol particles influence the radiation directly, by scattering and absorption (Angstroem, 1962; McCormic & Ludwig, 1967), as well as indirectly, by the modification of cloud properties (Twomey, 1974; Graßl, 1975; Twomey, 1977; Albrecht, 1989; Hansen *et al.*, 1997; Lohmann & Kärcher, 2002). Figure 2.11 shows the dependency of direct, diffuse and

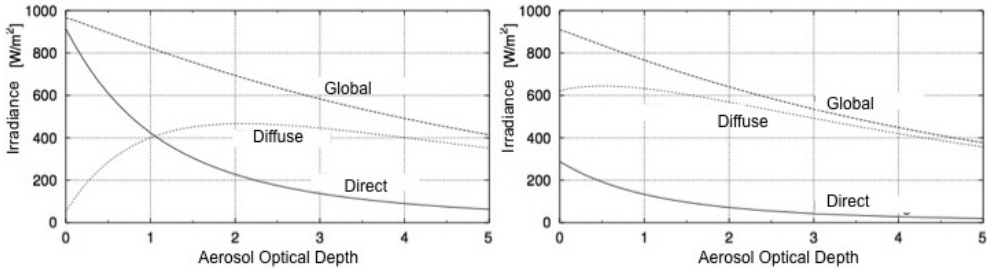

Figure 2.11: Dependency of global, diffuse and direct horizontal irradiances on the aerosol optical depth. Left panel: for an atmosphere without clouds. Right panel: for an atmosphere with a water cloud of cloud optical depth = 1. Source: (Lohmann, 2006, modified).

global horizontal irradiance on aerosol optical depth for a cloud-free (left panel) and a cloudy (right panel) midlatitude summer atmosphere ($\vartheta_0 = 30°$). Qualitatively, the irradiances in both plots show the same behavior as the irradiances in figure 2.10: Global and direct irradiances decrease exponentially. Diffuse irradiance increases at first, without fully compensating the loss of direct irradiance and then converges to the graph of the global irradiance.

Large influence on solar irradiances at the surface have - besides the solar zenith angle - clouds, aerosols, gases, surface albedo and altitude above sea level. The surface albedo is the relation between reflection at the surface and absorption by the surface, i.e. it is the single scattering albedo of the lowest atmosphere level (with $g = -1$). The reflected radiation may then be backscattered from the atmosphere to the surface and thereby modify irradiances at the surface. The altitude above sea level has to be taken into account because the atmosphere is geometrically and thereby optically thinner for high elevations. Figure 2.12 shows modeled horizontal irradiances at TOA (I_{TOA}) and at the surface (GHI). The blue patterns of very high extinction on the bottom map are a result of clouds. Although the dependency of surface irradiance on cloud and aerosol optical depth is similar, it is

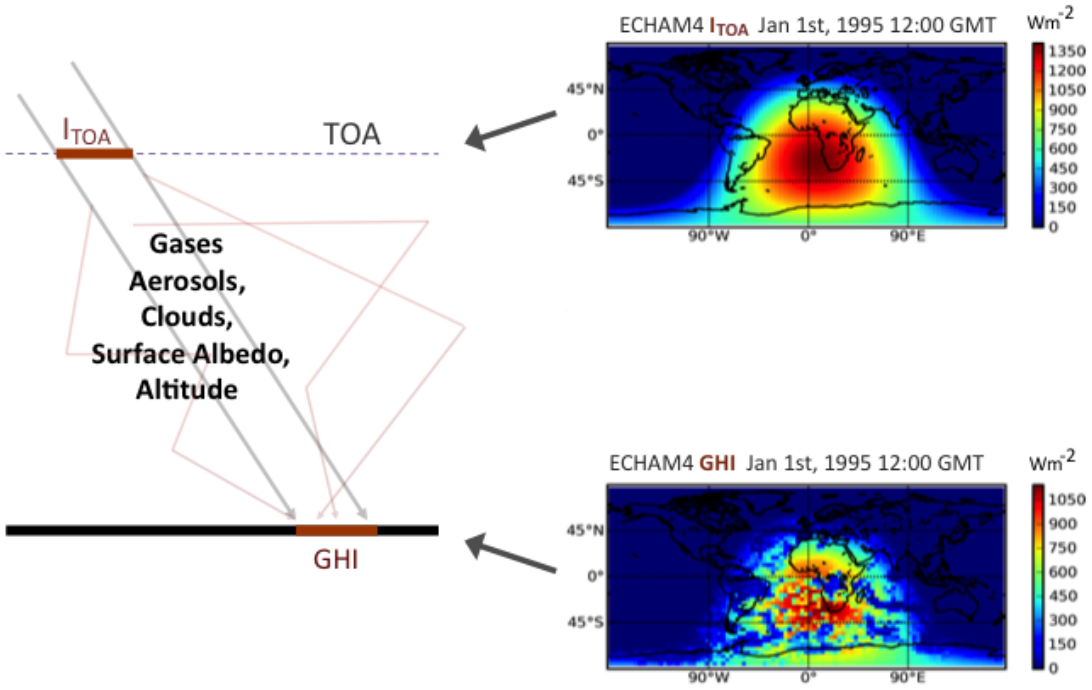

Figure 2.12: Gases, aerosols, clouds, surface albedo and altitude above sea level mainly influence how much solar radiation reaches the surface.

clouds that modify irradiances most because actual cloud optical depths are larger than actual aerosol optical depths.

2.4 Absorption by a solar power plant

The photons that reach the surface after passing through the atmosphere can be transformed into electrical energy by photovoltaic or concentrating solar power plants. Photovoltaic panels can use global horizontal irradiance, concentrating solar power systems transform direct normal irradiance into electrical energy.

2.4.1 Photovoltaics

Photovoltaic (PV) power generation employs solar panels composed of a number of solar cells (photo diodes). A solar cell converts radiative energy directly into electricity. Most solar cells are made of doped semiconductors arranged to give a p-n junction. The junction creates an electric field. Photons incident on the junction with $e(\nu)$ equal or greater than

the material's energy band gap generate free charge carriers (electrons and holes) in the semiconductor. These are separated by the field and thereby a current is induced when the PV cell is connected in a circuit (for detailes see textbooks on solid-state physics or physical electronics). The classical material for solar cells is crystalline silicon. The energy band gap of crystalline silicon is such that the majority of the photons within the visible part of the spectrum, i.e. the energetic maximum of the solar spectrum (see figure 2.7), has suitable energies to be absorbed. Photovoltaic panels based on crystalline silicon cells are encountering competition in the market by panels that employ so-called thin-film solar cells (TFSC). These are solar cells that are made by depositing one or more thin layers of photovoltaic material on a substrate. Many different photovoltaic materials are deposited with various deposition methods on a variety of substrates. Generally speaking, TFSC are less efficient but are also less expensive to produce. Solar panels are fueled by radiation from (nearly) any direction, i.e. solar panels can use direct and diffuse radiation. But which is usable radiation depends on

1. the photovoltaic material - which frequencies can be converted to electricity?
2. the inclination of the panel, some panels may be solar tracked - how is the surface orientated on which the radiation is incident?

The answers to 1. and 2. are various due to the variety of materials and constructions of solar panels. Therefore, the radiative quantity generally relevant for photovoltaic applications is the global horizontal irradiance. The radiation quantity that is relevant for the specific photovoltaic application may then be approximated with the given GHI.

2.4.2 Concentrating solar power

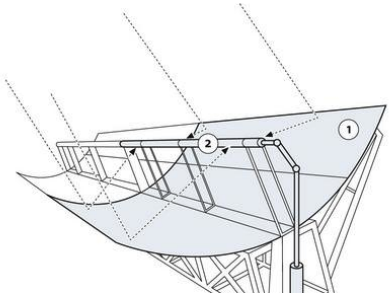

Figure 2.13: Illustration of the concentration of solar direct radiation by a parabolic through mirror system.

Concentrating solar power (CSP) plants use mirror systems to concentrate radiation and thereby produce heat. This heat can be used in a conventional power plant (i.e. a steam turbine connected to an electrical power generator) to generate electricity. The most common CSP technology is parabolic through systems, see figure 2.13. A parabolic through

consists of a linear parabolic reflector (1) that concentrates the parallel direct radiation onto a receiver positioned along the reflector's focal line. The receiver is a tube filled with a working fluid that absorbs the photons and heats up (2). The fluid is pumped through the solar field to the conventional power plant where the heat is transformed into electricity. The reflectors of a CSP parabolic through plant are tracked from East to West every day such that they are always oriented towards the Sun. This is necessary because the mirror geometry only works with parallel radiation. It is thus the direct normal irradiance that fuels CSP power plants.

Operating a CSP plant needs energy for the motors of the fluid pumps, the tracking system etc. This energy decreases the efficiency of the power plant and is called parasitic load. For a "common" parabolic through plant the minimum DNI that compensates the parasitic load such that operating the power plant pays off is assumed to be $200\,\mathrm{Wm}^{-2}$ (Meyer *et al.*, 2009).

3 Method: Calculation of Irradiances with Modeled Atmospheric Data

In this chapter the method developed in this work to calculate direct normal and global horizontal irradiances with atmospheric data produced by global climate models is described. It is distinguished between online calculations that are calculations performed by a climate model during a climate simulation, and offline calculations that are calculations using climate model data but independent of the simulation. The chapter starts with a short introduction to global climate models and the models used here are described together with the simulation set-ups before presenting the atmospheric data produced by these simulations. A new method is introduced to calculate 2D cloud properties online that are suitable to be used for offline calculations of direct irradiance. The execution of the offline calculations is explained. The calculations produced a data set of direct normal and global horizontal irradiances for the years 1995 - 1999 and 2035 - 2039. The data set has been named ISMAD (**I**rradiances at the **S**urface derived from **M**odeled **A**tmosphere **D**ata). A consistency check between the online and the offline calculations follows: the GHI calculated within this work is compared to the online GHI (DNI cannot be compared as GCMs do not compute direct irradiance). The chapter closes with a comparison between ISMAD and measurement-derived GHI and DNI for the years 1995 - 1999.

3.1 Model descriptions and simulation set-ups

The atmospheric data for the radiative transfer calculations were taken from runs of two versions of the GCM ECHAM (**EC**MWF-model, **HAM**burg version). The fundament of ECHAM is a global meteorological forecast model developed at the European Centre for Medium-Range Weather Forecasts (ECMWF) in Reading, England. The ECMWF-model has been modified for climate research at the Max Planck Institute for Meteorology (MPI) in Hamburg and was named ECHAM. Two different model generations and various versions of them are currently in use: ECHAM4 since 1996 (described in Roeckner *et al.* (1996)) and ECHAM5 since 2003 (Roeckner *et al.*, 2003).

3.1.1 Global climate models

GCMs are systems of differential equations (equations of motion plus radiative transfer equation ...). To "run" a model, the atmosphere is divided into a 3D grid and the equations are solved for each grid box with boundary conditions depending on the surrounding boxes, incoming solar radiation, emissions etc. The dynamic part of a climate model represented by the hydrodynamic equations can be coupled to complementary modules that consider physical or chemical processes and sub-grid scale dynamics within the climate system. The interactive coupling to a chemistry module allows for instance to consider chemical reactions of trace gases.
In global models the horizontal dimensions are often accounted for in a spectral way: the variation of some variable with latitude and longitude is expressed as a truncated series of spherical harmonics. The highest wave number is a measure for the model resolution. An advantage of spectral models is that they provide a model domain representing the cyclic character of the horizontal distribution with isotropic coverage of the Earth's surface, i.e. the sphere. Moreover, partial derivatives of wave fields can be calculated exactly, rather than by means of the finite difference approach (used in grid models). The results are converted back to grid space after the calculations and stored as variables of (lat,lon).
When running a GCM the computational time needed for the calculations has to be taken into account. Therefore, it is not possible to choose arbitrarily small grid boxes or to couple a GCM to arbitrarily many complementary modules (they are "expensive"). Radiation algorithms used by GCMs have to be really fast: two-stream methods with very low spectral resolutions. Because it is not possible to choose arbitrarily small grid boxes, processes like cloud formation occur on a too small scale to be resolved by climate models (to resolve single clouds a box size of about 5 km x 5 km would be required). Such sub-grid scale processes have to be physically parameterized. Parameterizations are empirical approximations based on large-scale (resolved) variables. They are evaluated by comparing observable quantities that result from these parameterizations to climatological data sets. The parameterizations of clouds is particularly challenging because only few observations about their vertical structure are available. Before a climate model simulation is started a tuning process is performed with present-day climatological data sets. "Tuning" means that, within the uncertainty of the simulated vertical cloud profile, low (water) and high (ice) clouds are modified individually by adjusting the respective physical processes (e.g. conversion of cloud droplets to rain, sedimentation of ice crystals). Such an adjustment results in the desired global radiation balance and leads to reasonable distributions of total cloud cover and precipitation in accordance with climatological data sets. This means that the vertical structure of clouds remains uncertain, but nevertheless modeled radiation - that is calculated with the uncertain clouds - can be in good agreement with observations as well as the horizontal distribution of clouds.

Climate models only simulate global horizontal irradiance, but no direct irradiance. The reason for this is that climate modelers are interested in energy budgets. Direct irradiance - as only a part of the whole radiative energy - is not relevant.
Climate models are widely applied to simulate the climate over many years, mainly to project climate change. GCMs can not predict the weather at a certain place and certain time, but mean values over several years and regions do provide reasonable information. As climate modelers are interested in time means, the standard output variables of GCMs are integrated over the output interval. As an example: A model may have an internal time step of 24 minutes. This means that the equations are solved every 24 (modeled) minutes. The output interval may be 6 hours. Then the mean value of the data that was calculated every 24 minutes within the last 6 hours is stored every 6 hours. As we want to use modeled data to perform radiative transfer calculations, instantaneous data is needed because irradiances calculated with a mean atmosphere are not the same as mean irradiances of an instantaneous atmosphere. However, it is not totally trivial to store instantaneous climate model data for the following reason: Different atmospheric quantities are calculated at different times within one time step; e.g. in the ECHAM4 GCM (and probably in other GCMs as well) radiation is calculated first, clouds are calculated last. Radiation of the time step t is calculated with atmospheric data of the time step $t-1$. The radiation modifies the atmosphere (e.g. temperature decreases and a cloud forms) and the modified atmosphere is that of the time step t. So radiation of the time step t is not calculated with the atmosphere of the time step t, the radiation first has to "produce" the new atmosphere. This does not matter when integrating over time, but it does when using instantaneous data.

3.1.2 ECHAM4

In this work the data about clouds, water vapor content, surface albedo and altitude above sea level are taken from a transient simulation (Garny, 2011) of the coupled chemistry-climate model ECHAM4.L39(DLR)/CHEM/ATTILA (E39CA). E39CA is based on the spectral GCM ECHAM4. The model name affix "L39(DLR)" indicates an enhanced vertical resolution from 19 to 39 layers added at the German Aerospace Center (DLR, *Deutsches Zentrum für Luft- und Raumfahrt*) (Land *et al.*, 1999). "CHEM" denotes that the chemistry module CHEM (Steil *et al.*, 1998) was coupled to the general circulation model (Hein *et al.*, 2001). The former semi-Lagrangian advection scheme was replaced by the fully Lagrangian advection scheme ATTILA (Reithmeier & Sausen, 2002) which improved the simulated water vapor (Stenke *et al.*, 2009). The spectral horizontal resolution of the model is T30, corresponding to approximately $3.75^\circ \times 3.75^\circ$ on the transformed latitude-longitude grid. Longitudes are equidistant, the distances in latitudes start with 3.75° at the equator and get a bit smaller towards the poles (due to the transformation from spectral space to a Gaussian (lat,lon)-

grid). The grid uses 96 longitudes and 48 latitudes what divides the Earth horizontally in 4608 grid boxes. In the vertical, the model consists of 39 layers, extending from the surface's altitude above sea-level - given as surface pressure - to the uppermost layer centered at 10 hPa. The internal time step, i.e. the times for which the physical processes are calculated, is 24 minutes.
The radiation algorithm used by E39CA to solve the RTE is a very fast two-stream code using only two spectral bands to simulate the complete solar spectral range (0.2 - 0.68 μm and 0.68 - 4.0 μm). The radiation code is based on the scheme developed by Morcrette (1991) for the numerical weather prediction model, cycle 44, of the ECMWF. Roeckner *et al.* (1996) provides a good overview. Details of the code can be found in the ECMWF code documentation (IFS, 2008, chapter 2.2). The solar zenith angle is calculated according to (Paltridge & Platt, 1976) with a correction due to the curvature of the Earth (Roeckner *et al.*, 1996, equation (111)). In contrast to the delta-Eddington two-stream method described by Zdunkowski *et al.* (2007) that was used for the calculations in this work, the E39CA radiation code obtains irradiances not through the solution of a system of linear equations in matrix form. Rather, the upward and downward irradiances are calculated for each layer with the reflectances $R_{top,i}$ at the top of the layers and the transmissions $T_{bot,i}$ through the bottoms of the layers. E39CA diagnoses a fractional cloud cover c_i for each layer to parameterize sub-grid scale clouds. $R_{top,i}$ and $T_{bot,i}$ are a weighted sum of the reflectance/transmittance of the layer's cloudy (cld) and clear sky (=no clouds but aerosols and gases, clr) fraction:

$$R_{top,i} = c_i \, R_{cld,i} + (1 - c_i) \, R_{clr,i} \tag{23}$$

$$T_{bot,i} = c_i \, T_{cld,i} + (1 - c_i) \, T_{clr,i} \; . \tag{24}$$

For the calculation of the reflectances and transmittances within the cloudy part of a layer the delta-Eddington approximation is used.
Coefficients for the gaseous absorption are derived from the HITRAN database (Rothmann & et al., 1992). Rayleigh scattering is included via a parametric expression of optical thickness (simply depending on layer pressure and solar zenith angle) (IFS, 2008, equations (2.29), (2.30)). The cloud radiative properties are a function of the cloud water/ice path. The indirect aerosol effect, i.e. the aerosol-cloud interaction, is not considered in the model.

The transient simulation of E39CA (Garny, 2011) spans the years 1960 to 2049. The simulation is designed to model past and future development of the atmospheric system in a consistent manner.
Before 1999, boundary conditions are deduced from observations: The concentrations of greenhouse gases (CO_2, CH_4, N_2O) are based on the values given in IPCC (2001). The 11-year solar cycle and the quasi-biennal oscillation (QBO, quasi-periodic oscillation of the

equitorial zonal wind between easterlies and westerlies in the tropical stratosphere with a mean period of about two years) are prescribed to resemble observed natural variability. The three major volcanic eruptions (Agung 1963, El Chichon 1982 and Pinatubo 1991) are taken into account by enhanced stratospheric aerosol abundances and additional radiative heating.
After 1999, the boundary conditions for the simulation follow future scenarios: The concentrations of greenhouse gases follow the SRES A1B scenario given by IPCC (2001). The natural boundary conditions are extrapolated by repeating the solar cycle and the QBO periodically. It is assumed that no volcanic events occur in the future.
Apart from the volcanic eruptions considered before 1999, the evolution of aerosols is not considered. The simulation uses only a prescribed aerosol climatology (Tanré *et al.*, 1984) as input for computing the radiative transfer: monthly mean values that are the same for every year with a very rough horizontal resolution (T10).

The atmosphere data from the described E39CA simulation were chosen as input for the offline radiative transfer calculations of this work for the following reasons. Firstly, ECHAM4 is a widely applied general circulation model that has often proven to perform reasonably well. A comparison of ECHAM4 zonal mean values of total cloud cover to observational data was performed by Wild *et al.* (1998) and revealed a very good agreement for low and midlatitudes. Global horizontal irradiances calculated online with the ECHAM4 clouds show as well very good agreement for low and midlatitudes. The second reason for the choice of the E39CA simulation is that for this simulation 12-hourly instantaneous atmosphere data had already been stored (they had been produced to perform radiative transfer calculations of global irradiance in the UV spectral band) and this work was originally intended to use them.
During this study it turned out that these data could not be used because the instantaneous vertical cloud properties were not consistent with the instantaneous horizontal cloud data (see section 3.2.3) that are additionally required for the calculation of direct irradiances. Thanks to the support of Michael Ponater (DLR) and Hella Garny (DLR) it was possible to identify the cause for the inconsistency (see section 3.2.3) and to produce new consistent data. The E39CA simulation was tested and run again for the years 1995 - 1999 and 2035 - 2039. It would have been preferable to obtain data of a wider time range, but the time limit that is set to a diploma thesis did not allow to invest more time in the production of the atmospheric data. Nevertheless, the need to run the simulation once again yielded advantages as well: A new method to calculate online a column optical depth of the cloud covered part of a grid box could be implemented in the GCM radiation code what simplified the offline calculations of direct irradiance substantially. The temporal resolution of the atmospheric data could be improved from 12-hourly to 6-hourly instantaneous values.

In the following the described simulation of the chemistry-climate model E39CA will be referred to as ECHAM4.

3.1.3 ECHAM5

ECHAM4 only uses an aerosol climatology (Tanré *et al.*, 1984). As GHI and particularly DNI are highly influenced by aerosols (see figure 2.11), the temporal evolution of aerosols should be considered for the offline radiative transfer calculations. Evolving aerosol data are provided by interactively coupled aerosol-climate models. The time-integrated standard output of such a simulation can be used because aerosols are less variable than clouds.
The coupled ECHAM5 - HAM - MPI-OM - HAMMOC5 model (Kloster *et al.*, 2006) was chosen, consisting of the following interactively coupled models: the GCM ECHAM5 (Roeckner *et al.*, 2003), the atmospheric aerosol module HAM (Stier *et al.*, 2005) and an ocean general circulation (MPI-OM) and ocean biochemistry (HAMOCC5) module. The microphysical aerosol module HAM includes the components sulfate, black carbon, particulate organic matter, sea salt and mineral dust. Emissions of mineral dust for instance are coupled to the GCM by being a function of wind speed, soil moisture and snow cover; sea salt emissions depend on wind speed and sea ice cover etc. The spectral horizontal resolution is T63 (corresponding to 1.8° x 1.8°). In the vertical the model consists of 19 layers.
The aerosol model HAM was evaluated in an ECHAM5-HAM simulation by Stier *et al.* (2005). The simulated global average of aerosol optical depth (0.14) was found to be in very good agreement with estimates from remote sensing products: AERONET derived a global average optical depth of 0.14 and the MODIS-MISR composite provides a value of 0.16. Another ECHAM5-HAM aerosol optical depth evaluation by Roelofs *et al.* (2010) for a site in the Netherlands revealed that the monthly mean values of aerosol optical thickness are consistent within 20 % with AERONET measurements.

The model simulation that provided the aerosol data for this work spans the years 1860 - 2100 (Stier *et al.*, 2006). The same as in ECHAM4 greenhouse gases and optical depths of stratospheric aerosols from volcanic eruptions are prescribed due to observations in the 20th century. After 2000 emissions are based on the SRES A1B scenario and it is assumed that no high-reaching volcanic eruptions take place (like in ECHAM4). In the following the described ECHAM5 - HAM - MPI-OM - HAMMOC5 simulation is abbreviated as ECHAM5.

3.1.4 Combination of global climate model data

To combine data from different model runs as done in this work can be problematic. Comparing the two models, we notice that both apply the same emission scenario (A1B), i.e. the emission boundary conditions for which the equations are solved in the two models are the same. That means that a basic condition to combine the data is fulfilled. In ECHAM4 clouds and aerosols do not interact (no indirect aerosol effect). This could mean that it is possible to add the ECHAM5 aerosols as a kind of climatology to ECHAM4 (the same way the ECHAM4 aerosols are used). But is it totally true that clouds and aerosols do not interact in some way in ECHAM4? In ECHAM4 the clouds are tuned in present-day climate to achieve a balanced radiation budget at TOA. So the amount of present-day aerosols used for the tuning in fact can influence the clouds by reflecting radiation. More reflection by aerosols leads to less clouds due to the tuning. When adding different aerosols after the model simulation, this tuning effect on clouds is missing. Sometimes it is difficult to totally understand the possible influence one quantity could have on another within a climate model, as climate models are programmed as complex many thousend lines long codes that evolved from older codes and no researcher is involved in all parts of it. Erich Roeckner, the author of ECHAM description reports, once said at a presentation at DLR: "Nobody knows everything about ECHAM" (Michael Ponater (DLR), personal communication). A priori we can not exactly know how good the combination of the ECHAM4 clouds and ECHAM5 aerosols works for the offline radiative transfer calculations. Therefore, a comparison of the data produced with the combined atmospheric data to measurement-derived data was performed that is presented in section 3.5.

3.2 Presentation of the atmospheric data

In this section the GCM atmospheric data used for the radiative transfer calculations is presented together with further data, methods and assumptions that have to be applied/made in order to obtain complete input for the calculations. It is focused on differences between future (2035 - 2039) and past (1995 - 1999) five-yearly mean values in order to identify changes of the atmospheric data that may lead to differences between future and past irradiances.

3.2.1 Local noon data

Amongst the atmospheric data it is clouds that influence GHI and DNI most. ECHAM4 provides cloud data with a 6-hourly temporal resolution (00:00, 06:00, 12:00 and 18:00 GMT).

Bugliaro *et al.* (2006) showed that UV daily doses (irradiances of the UV band integrated over daytime) can be better approximated when having knowledge of cloud optical properties during noontime than in the morning or in the evening. In other words, irradiances at noontime do tell most about the whole day behavior (at least in the UV).
In the last part of this work the mean values of the irradiances of the future (2035 - 2039) are compared to their past mean values (1995 - 1999). If the means of the 6-hourly resolved data would be calculated in the usual way (unweighted sum of all time steps / number of time steps), it would not be accounted for the fact that the irradiances at the local noontime contain more information about the daily doses than the irradiances in the morning or in the evening (or at night of course). As it is meaningful to compare radiation data that provide most information about the whole day behavior, the following procedure has been selected: For any point on Earth (lat,lon) we consider that time $\in$ {00:00, 06:00, 12:00 and 18:00 GMT} that is closest to the local noontime. Figure 3.1 illustrates the composition of "local noon" data by showing the 1995 - 1999 mean solar zenith angle for each ECHAM4 box (lat,lon). For every day we now have one map with "local noon" data instead of four maps for any time step.

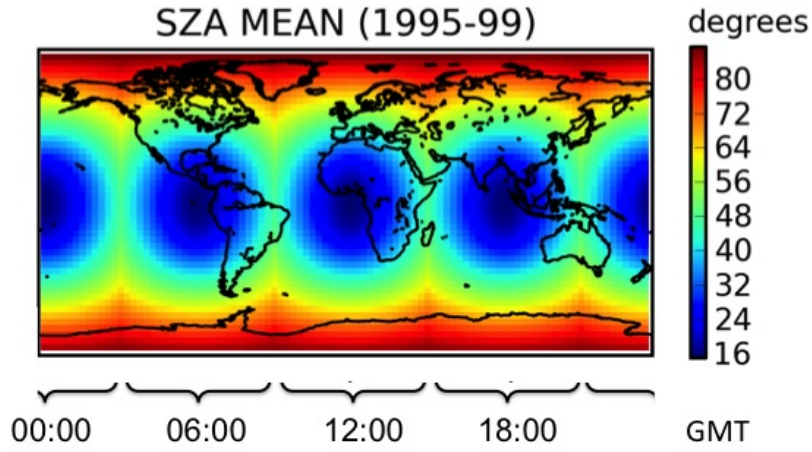

Figure 3.1: Illustration of the composition of a "local noon" data map.

Another advantage of taking local noon data is that irradiances which are calculated with large solar zenith angles are not considered (at least for low latitudes). As stated above, the plane-parallel approximation that is used in the later radiative transfer calculations is not correct in the case of large solar zenith angles. That we still have this case for high latitudes is not problematic because sites at high latitudes are not suitable for solar power generation anyway.

3.2.2 Atmospheric gases

Five standard profiles for radiatively relevant atmospheric gases are used, depending on the time of the year and on latitude: a winter and summer atmosphere for mid and high latitudes and a tropical atmosphere (all provided by Anderson *et al.* (1986)). They contain vertical profiles of pressure, temperature, and particle concentrations of air, water vapor, ozone, carbon dioxide etc. Variability of the composition of dry i.e. water vapor-free air is very low (Kraus, 2004). Variabilty in ozone concentrations for instance influences the global and direct irradiance at the surface only $\ll 1\%$ (Lohmann, 2006). Water vapor instead is highly variable (0 - 4 Vol%, Kraus (2004)). Therefore, the water vapor of the standard profile is replaced by ECHAM4 water vapor, i.e. the standard vertical profile is scaled such that vertical integration yields the ECHAM4 vertically integrated water vapor.
The top map of figure 3.2 shows the ECHAM4 (1995 - 1999) mean local noon column-integrated water vapor content in units [molecules cm^{-2}]. The mean values of the local noon water vapor column denoted by X were calculated for each grid box (lat,lon) by

$$\mathrm{Mean}_{1995-99}(X(\mathrm{lat,lon})) = \frac{1}{n}\sum_{k=1}^{n} X(t_k, \mathrm{lat,lon}) \tag{25}$$

with n being the number of daily time steps t_k between January, 1st 1995 and December, 30th 1999 (all model months have 30 days in ECHAM4). The 1995 - 1999 global mean value is $7.49 \,\mathrm{x}\, 10^{22}$ molecules cm^{-2}. This value was calculated as an area-weighted mean of the (1995 - 1999) means of all ECHAM4 boxes. Highest water vapor column values are located around the equator where solar insolation is biggest. The absolute difference between the (2035 - 2039) and the (1995 - 1999) mean values

$$\mathrm{AD\,(2035\text{-}39,\ 1995\text{-}99)} = \mathrm{Mean}_{(2035-39)} - \mathrm{Mean}_{(1995-99)} \tag{26}$$

and the relative difference

$$\mathrm{RD\,(2035\text{-}39,\ 1995\text{-}99)} = \begin{cases} \frac{AD\,(2035-39,1995-99)}{\mathrm{Mean}_{(1995-99)}} \cdot 100 & \text{if} \quad \mathrm{Mean}_{(1995-99)} > 0 \\ \\ \frac{\mathrm{AD\,(2035\text{-}39,\ 1995\text{-}99)}}{10^{-6}} \cdot 100 & \text{else} \end{cases} \tag{27}$$

are illustrated on the second and third map. The 2035 - 1939 global mean value is with $8.03 \,\mathrm{x}\, 10^{22}$ molecules cm^{-2} 7 % higher than the 1995 - 1999 global mean. Most significant differences up to about 20 % are found on the poles. The significance of differences between

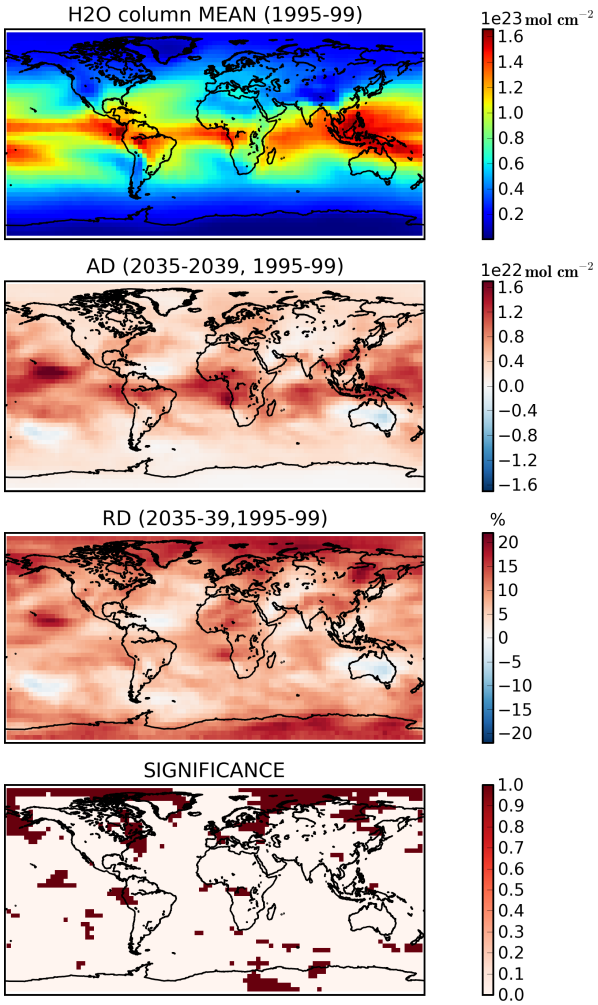

Figure 3.2: ECHAM4 local noon water vapor column.
Top panel: (1995 - 1999) mean values. Second from the top: Absolute difference (AD) between future (2035 - 2039) and past (1995 - 1999) mean values. Third from the top: Relative difference (RD) between future and past mean values. The bottom map illustrates where differences are significant.

the future and past 5-yearly means was calculated by

$$\text{Significance} = \begin{cases} 1 & \text{if} \quad \left| \text{Mean}_{2035-39} - \text{Mean}_{1995-99} \right| \\ & \qquad > \; 2\left(\text{STD}_{2035-39} + \text{STD}_{1995-99}\right) \\ 0 & \text{else} \end{cases} \tag{28}$$

with STD denoting the standard deviation of the 5-yearly means calculated against annual means. The 1995 - 1999 standard deviation is for instance

$$\mathrm{STD}_{1995-99} = \sqrt{\frac{1}{5}\sum_{y=1995}^{1999}\left(\mathrm{Mean}_y - \mathrm{Mean}_{1995-99}\right)^2}\,. \tag{29}$$

All mean values, differences and significances within this work were calculated accordingly. The water vapor column is generally larger in the future than in the past. The reason for this behavior can most probably be found in global warming.

The optical properties of the presented atmosphere are obtained as follows: Rayleigh scattering properties are calculated according to Bodhaine *et al.* (1999), and a correlated-k method introduced by Fu & Liou (1992) is applied to consider the highly wavelength dependent absorption coefficient of the atmospheric gases with only six spectral bands.

3.2.3 Clouds

In ECHAM4 clouds are parameterized for each of the 3D grid boxes (lat,lon,layer) in the following way:
Firstly the cloud cover c_i is determined for each layer i as a function of relative humidity (Ponater *et al.*, 2002, and (Sundqvist, 1978) therein). Within the cloud covered part the air is assumed to be saturated with water vapor.
Secondly the optical properties (extinction coefficient, asymmetry parameter and single scattering albedo) of the cloud within the cloud covered part of the layer are obtained by Mie calculations with the diagnosed liquid/ice water content and droplet/ice sphere effective radius (the effective radius is a function of liquid/ice water content itself) (Roeckner *et al.*, 1996). As Mie calculations overestimate the asymmetry parameter g for scattering by non-spherical ice particles, g for ice clouds is corrected to ≈ 0.8. Thus, for each layer ECHAM4 provides an optical thickness for water and ice clouds respectively with different scattering and absorption properties. These are used to calculate mixed phase optical properties that account for water and ice clouds at the same time (IFS, 2008, equations (98)-(100)). The mixed phase cloud optical depth of the layer i is denoted by τ_i.
As the storage of complete 3D profiles of the cloud cover c_i and optical depth τ_i at each time step is not feasible, Bernhard Mayer (LMU) introduced a method in the ECHAM4 1960-2049 simulation to calculate a 2D effective optical depth (unpublished). This 2D effective optical depth provides sufficient cloud information for the offline calculation of global irradiances. This effective optical depth that is suitable for offline calculations of global irradiance is here referred to as global effective optical depth τ_{glob} in order to distiguish it from the of-

fline effective optical depth τ_{oln} and the effective optical depth τ_{eff} that will be presented after τ_{glob}.
The global effective optical depth per layer $\tau_{glob,i}$ is defined by the transmission T of global radiation through the layer:

$$T(\tau_{glob,i}) = c_i \cdot T(\tau_i) + (1 - c_i) \cdot T(\tau_i = 0)\,, \tag{30}$$

where c_i denotes the cloud cover of the layer i and τ_i is the mixed-phase optical depth within the cloudy part. ECHAM4 calculates first the transmission $T(\tau_i)$ through the with c_i cloud covered part that contains a cloud with optical depth τ_i plus the transmission $T(\tau_i = 0)$ through the clear-sky fraction and then finds a $\tau_{glob,i}$ for which the above condition is fulfilled. In other words, the effective optical depth $\tau_{glob,i}$ is the optical depth of a layer containing a homogeneous cloud which would lead to the same transmission as the inhomogeneous (only partly cloud covered) model layer.
According to equation (18) adding all effective optical thicknesses $\tau_{glob,i}$ yields the total effective optical depth

$$\tau_{glob} = \sum_{i=1}^{39} \tau_{glob,i} \tag{31}$$

that describes the optical depth of a homogeneous atmosphere.
This effective optical depth τ_{glob} can be used for offline calculations of global irradiance as it is defined by the condition that the transmitted GHI be the same as the GHI calculated by the ECHAM4 radiation code. But for the calculation of direct irradiance it is not possible to make the assumption of a homogeneous atmosphere. As an example: Consider a global effective optical depth of 5. This leads to a direct irradiance of $0\,\mathrm{Wm}^{-2}$ at the surface, see figure 2.10. But if the atmosphere is not completely cloud covered, the direct irradiance would of course be > 0, no matter how large the cloud optical depth within the cloud covered part is. Therefore, for the calculation of DNI the total cloud cover has to be considered.

Total cloud cover

In ECHAM4, the total cloud cover c_{tot} is a function of the 39 cloud covers c_i per layer according to the maximum random overlap assumption (MRO) as described e.g. in Räisänen (1997). The assumption is that the cloud fractions of adjacent layers overlap maximally while cloud fractions of layers seperated by a cloudless layer overlap randomly. It is meaningful to assume that clouds are contiguous in the vertical because cloud formation is often a convective process.

The basic idea to calculate direct irradiances with the global effective optical depth τ_{glob} and

the total cloud cover c_{tot} was to compute another effective optical thickness offline (τ_{oln}) which describes the optical thickness of the with c_{tot} cloud covered part of the atmosphere by requiring that the GHI calculated offline with τ_{glob} be the same as the GHI calculated offline with τ_{oln} and c_{tot}:

$$\mathrm{GHI}(\tau_{oln}, c_{tot}) = \mathrm{GHI}(\tau_{glob})\,. \tag{32}$$

For the calculation of $\mathrm{GHI}(\tau_{oln}, c_{tot})$ the independent column approximation (ICA) was assumed:

$$\mathrm{GHI}(\tau_{oln}, c_{tot}) = c_{tot} \cdot \mathrm{GHI}(\tau_{oln}) + (1 - c_{tot}) \cdot \mathrm{GHI}(\tau = 0)\,. \tag{33}$$

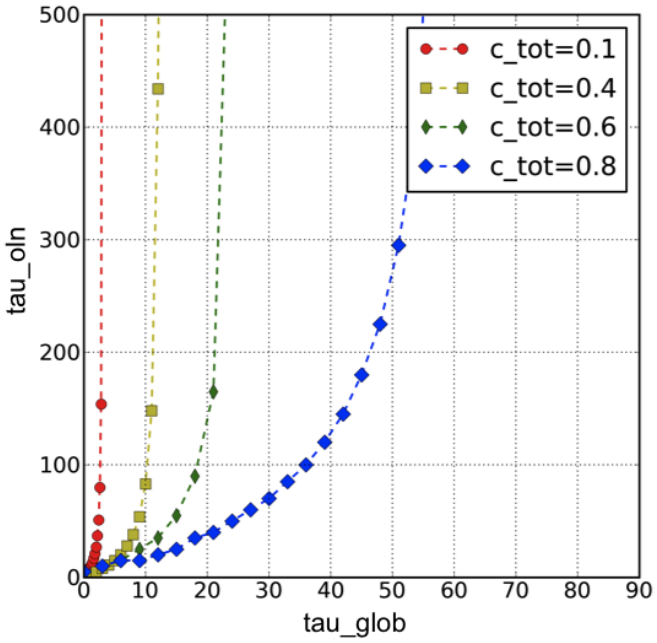

Figure 3.3: Relation between offline effective optical depth τ_{oln} and global effective optical depth τ_{glob} for different values of total cloud cover c_{tot}. The RTE was solved using a two-stream method (Mayer & Kylling, 2005, "rodents") and the correlated-k band parameterization by Fu & Liou (1992).

Figure 3.3 illustrates the relation between the offline effective optical depth τ_{oln} and the global effective optical depth τ_{glob} for various values of the total cloud cover c_{tot}. τ_{oln} (that describes the optical depth of the cloud covered fraction of the atmosphere) increases exponentially with increasing τ_{glob} (that describes the optical depth of a homogeneous atmosphere). The smaller the total cloud cover c_{tot} the faster τ_{oln} increases. This behavior is caused by the fact that the extinction of only the cloud covered part of the atmosphere (described by τ_{oln}) has to account for the extinction of the complete homogeneous atmosphere described by τ_{glob}.

The presented procedure to compute an offline effective optical depth with the global effec-

tive optical depth and the total cloud cover would have allowed to calculate offline direct irradiances, if the following inconsistency between τ_{glob} and c_{tot} would not have been detected: the c_i used for the online calculation of τ_{glob} are not the same c_i that were used for the online calculation of the total cloud cover c_{tot}. The two c_i differ because they are from different model time steps. As was stated in section 3.1.1, this problem can arise when extracting instantaneous climate model output because within a time step the model works with two values of each modeled quantity: the value of the time t and the value of the time $t-1$. Thus, the total cloud cover and the effective optical depth were not consistent and direct irradiance could not be calculated with the data produced by this ECHAM4 run (1960 - 2049).
A new ECHAM4 run was set up for the years 1995 - 1999 and 2035 - 2039. The need to set up a new run yielded the advantage that a modified global effective optical depth that is better suitable for the calculation of direct irradiances could be implemented. This new effective optical depth was used for the offline radiative transfer calculations in this work and is described next.

Effective optical depth

The effective optical depth per layer $\tau_{eff,i}$ is defined by the transmission through the total cloud cover fraction of each layer:

$$T(\tau_{eff,i}) = \frac{c_i}{c_{tot}} \cdot T(\tau_i) + \left(1 - \frac{c_i}{c_{tot}}\right) \cdot T(\tau_i)\,, \tag{34}$$

where c_i denotes the cloud cover of the layer i and τ_i is the optical depth within the cloudy part. c_{tot} is the total cloud cover. The model now calculates first the transmission with c_i and τ_i and then finds a τ_{eff} for which the above condition is fulfilled. The procedure is the same as for the calculation of the global effective optical depth τ_{glob} described above with the only difference that the effective optical depth τ_{eff} does not assume a homogeneous atmosphere, but describes like the offline effective optical depth only the extinction within the cloud covered fraction c_{tot} of the atmosphere. The 2D effective optical depth τ_{eff} is according to equation (18) obtained by a summation over all layers:

$$\tau_{eff} = \sum_{i=1}^{39} \tau_{eff,i}\,. \tag{35}$$

GHI and DNI were calculated offline once with τ_{glob} and once with τ_{eff} for all grid boxes at a single time step (January, 1st 12:00 GMT). A comparison between the global mean values revealed that both methods lead to the same GHI ($180\,\mathrm{Wm}^{-2}$), but provide strongly different values of DNI: the DNI calculated with τ_{glob} ($98\,\mathrm{Wm}^{-2}$) is due to assuming a ho-

mogeneous atmosphere 24 % smaller than the DNI calculated with τ_{eff} and c_{tot} (122Wm^{-2}). This difference illustrates the necessity of using the effective optical depth τ_{eff} instead of τ_{glob} for offline calculations of direct irradiance. The RTE was solved for an atmosphere like described above containing ECHAM4 clouds and ECHAM4 aerosols (Tanré *et al.*, 1984) applying a two-stream method provided by *libRadtran* (Mayer & Kylling, 2005, "rodents") and a correlated-k band parameterization (Kato *et al.*, 1999).

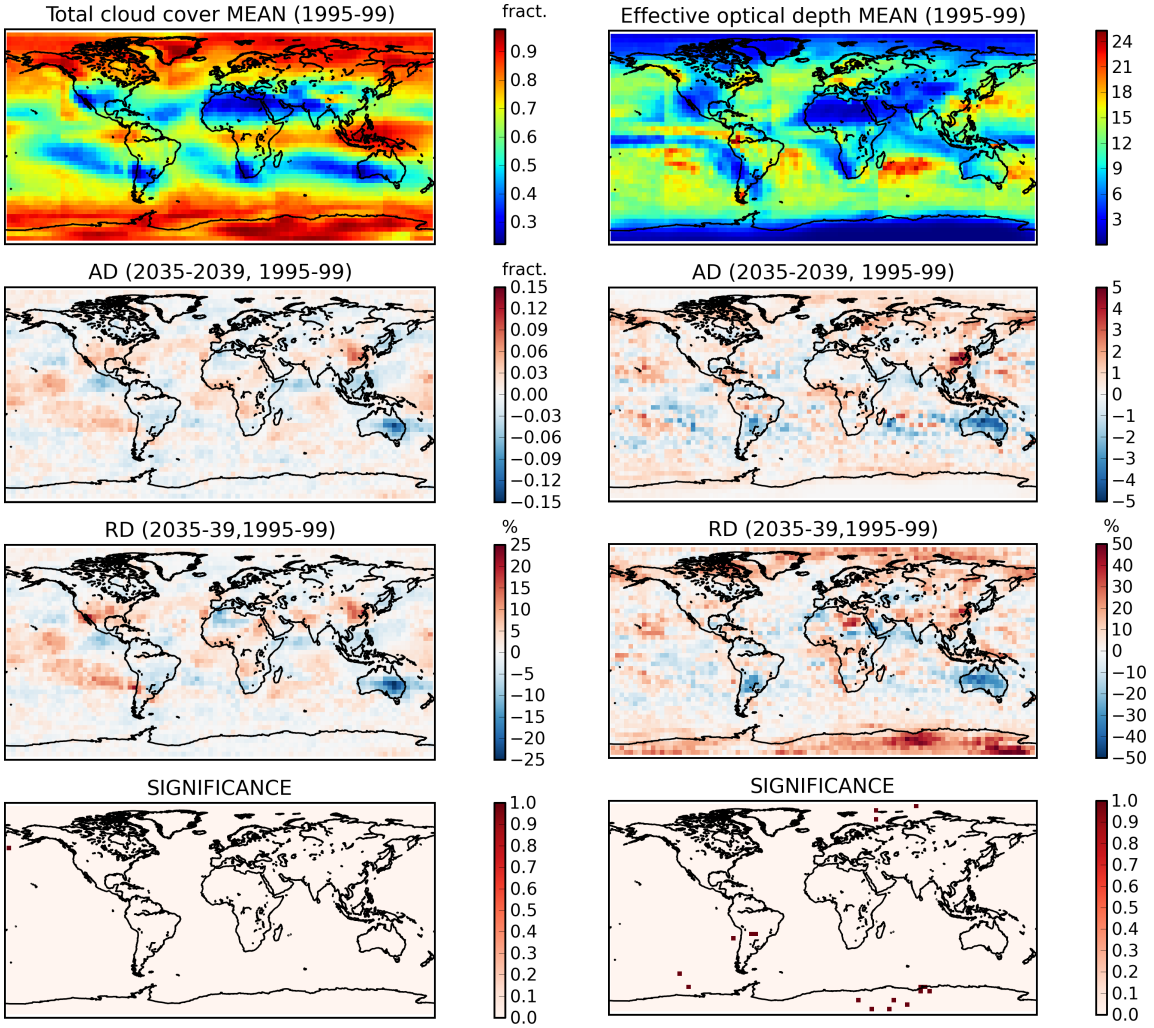

Figure 3.4: Same as in figure 3.2 for total cloud cover (left panel) and effective optical depth (right panel).

The top maps of figure 3.4 illustrate the 1995 - 1999 mean value of the total cloud cover (left side) and effective optical depth (right side). Mean values are calculated as defined in equation (25). Be careful with the interpretation of the mean effective optical depth: Due to the definition of the mean value a small effective optical depth does not necessarily indicate that clouds are thin; the mean was calculated with the values of all time steps, i.e. time steps with no clouds ($c_{tot} = 0$, $\tau_{eff} = 0$) are considered as well and may lead to

small mean values of τ_{eff} although clouds - when there - may be thick. A small τ_{eff} can be interpreted as thin clouds in the case of large c_{tot} and changes of τ_{eff} can be interpreted as changes of the cloud thickness in the case of no or opponent changes of c_{tot}.
Generally speaking, the cloud cover at midlatitudes is lower than it is around the equator and for high latitudes. In contrast, the effective optical depth (top right map) is lowest at high latitudes. This indicates that there are many, but thin clouds at high latitudes. Very low values of c_{tot} (as well as of τ_{eff}) are located over the Saharan region. The second and third maps from the top show the absolute and relative differences between the 2035 - 2039 and the 1995 - 1999 mean values (defined in equations (26) and (27)). The 2035 - 2039 global mean value of the total cloud cover (0.662) is slightly larger than the corresponding past value (0.660) (the future global mean of τ_{eff} is with 10.88 as well bigger as the corresponding past value of 10.77). The most noticeable difference between future and past clouds is located over Australia: the 2035 - 2039 mean cloud cover is up to 25 % smaller than in the past time period, but changes are not significant.

c_{tot} and τ_{eff} only provide 2D (lat,lon) information about clouds, but no information about the vertical distribution. Thus, to calculate irradiances at the surface an assumption about the vertical distribution has to be made. For the radiative transfer calculations all clouds are assumed to be located between 3 and 4 km.
A sensitivity study of GHI on cloud geometrical properties in Wapler (2007) shows that height and geometrical thickness of clouds have relatively small influence on GHI: For a solar zenith angle of 30° a variation in height between 200 and 7000 m leads to 1.5 % less GHI for $\tau = 2$ and up to 3.5 % less GHI for $\tau = 20$. Variations in geometrical thickness between 200 and 5000 m cause 1 % less GHI for $\tau = 2$ and up to 5 % less GHI for $\tau = 20$. Changes in the vertical profile within a cloud (for a constant total optical depth and constant height and geometrical thickness) have less influence with less than 0.1 % for $\tau = 2$ and less than 1 % for $\tau = 20$.
The optical properties of clouds in the offline calculations were adjusted to the ECHAM4 mixed-phase cloud optical properties and therefore not 6 spectral bands like for atmospheric absorption (Fu & Liou, 1992), but only 2 spectral bands (the same as in ECHAM4) are considered. In other words, the offline solution method solves the RTE for every of the 6 spectral bands defined in Fu & Liou (1992) with ECHAM4 cloud properties that are constant within the range of each of the two ECHAM4 spectral bands.

3.2.4 Aerosols

In the main offline calculations of GHI and DNI ECHAM5 aerosols are used. They include sulfate, black carbon, particulate organic matter, sea salt and mineral dust. They are given as monthly means of total column optical depth (at 550 nm), i.e. as the sum of the

optical depths of the five kinds and of the 19 model layers. The horizontal resolution is 1.8° x 1.8°. To adjust the aerosol data to the ECHAM4 cloud data with horizontal resolution 3.75° x 3.75° a first order conservative remapping (Jones, 1999) was performed.

Figure 3.5 illustrates the 1995 - 1999 mean of the aerosol optical depth on the remapped

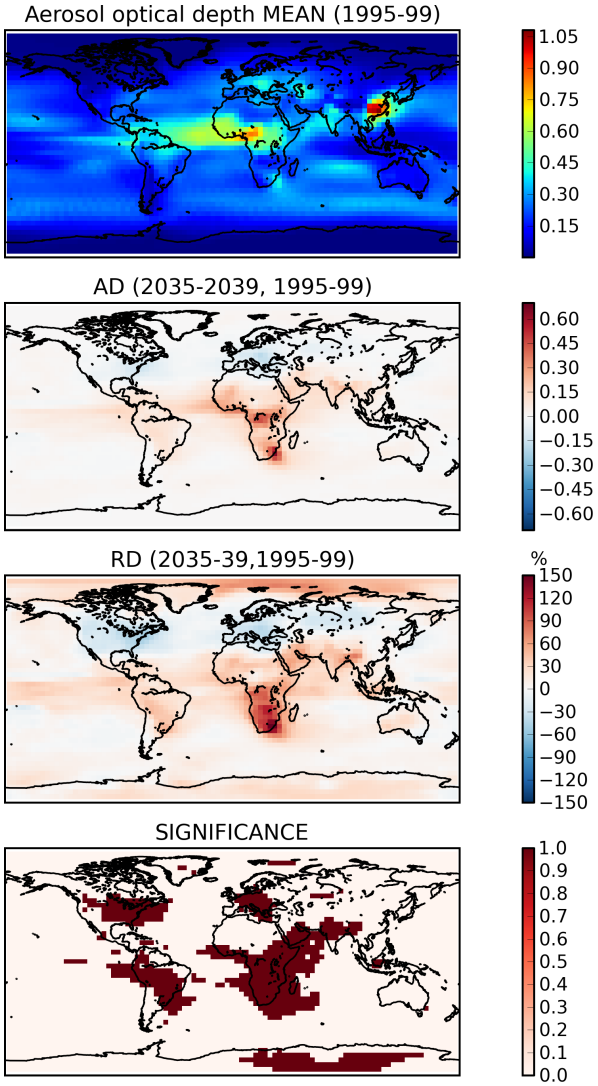

Figure 3.5: Same as in figure 3.2 for ECHAM5 aerosol optical depth.

grid (top map), and absolute and relative differences between the future and past 5-year periods (second and third map). The predominant features of the mean map are the Saharan dust plume extending into the Atlantic and Asian regions with strong anthropogenic pollution (Stier *et al.*, 2005). The 2035 - 2039 global mean optical depth is with 0.25 14 % larger than the 1995 - 1999 global mean of 0.22. The future aerosol optical depth is significantly bigger over Southern, East and West Africa, South America and India, whereas it is significantly smaller over North America and Europe. The most noticeable change of the

aerosol optical depth is found over Southern Africa with up to 150 % higher future values. The global mean sulfate and black carbon emissions increase from the 1990's to the 2030's mainly due to fossil fuel burning. In the same time period the global particulate organic matter emissions increase, dominated by the contribution from vegetation fires. For details, see Stier *et al.* (2006).

As the ECHAM5 aerosols are given as 2D total optical depth, the vertical resolution and the component (dust, sea salt etc.) resolution are lost. Hence, an assumption about the missing information has to be made. The desert aerosol profile provided by Hess *et al.* (1998) is applied, which gives a vertical and component resolution. The desert profile is chosen because it is desert areas that are most relevant for solar power generation and thus it is aimed for the irradiance calculations to be most accurate in these regions.

3.2.5 Surface albedo and altitude

Figure 3.6 shows the ECHAM4 mean surface albedo (of both spectral bands) for the years 1995 - 1999 and absolute and relative differences between the 2035 - 2039 and 1995 - 1999 mean values. The reflection of solar radiation is strongest for ice covered surfaces and deserts. The future 2035 - 2039 global mean albedo is smaller (0.155) than the past 1995 - 1999 global mean (0.160). Most changes between future and past values occur around the poles, where ice is melting and thereby the surface albedo decreases. For the here used definition of significance (equation (28)) some decreases on Greenland and the North pole are significant. The ECHAM4 surface altitude above sea level is shown in figure 3.7. Highest grid box averaged altitudes up to about 5 km are of course found in the Tibetean plateau region. The wavelike patterns over the oceans are owed to the fact that ECHAM4 is a spectral model. In the case of surface altitude $z_{Sur} < 0$, z_{Sur} was set to zero for the radiative transfer calculations in this work.

Summing up the last sections, we have for every of the 4608 ECHAM4 grid boxes and every 6-hourly time step from 1995 to 1999 and 2035 to 2039 (= 14400 time steps) an atmosphere profile considering the ECHAM4 water vapor, ECHAM4 clouds between 3 and 4 km height that are described by the effective optical depth τ_{eff} and the total cloud cover c_{tot}, ECHAM5 aerosols vertically distributed according to the OPAC desert aerosols, ECHAM4 surface albedo and altitude. These data were presented as local noon data because that is how this work's results are presented later. The comparison between future and past mean values revealed decreases of the cloud amount over Australia and a strong increase of aerosols mainly over Southern Africa. Next, the offline radiative transfer calculations are described.

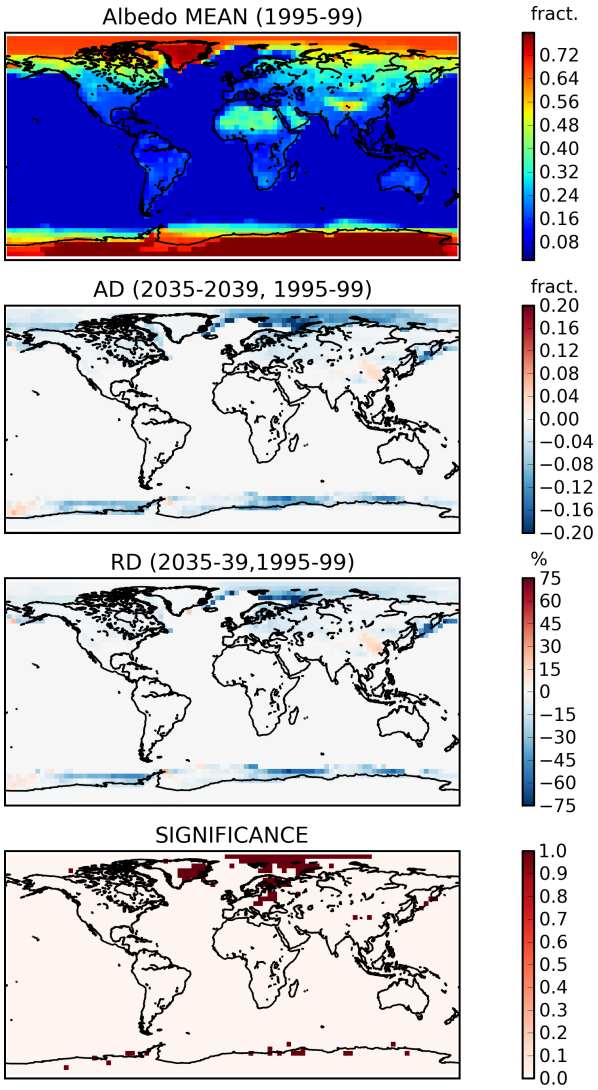

Figure 3.6: Same as in figure 3.2 for ECHAM4 surface albedo.

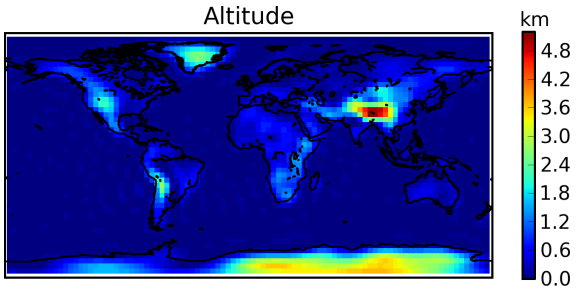

Figure 3.7: ECHAM4 altitude.

3.3 The radiative transfer calculations

The radiative transfer calculations were performed with the help of *libRadtran* (**lib**rary for **rad**iative **tran**sfer), a software package providing a suite of tools and data sets concerning radiative transfer (Mayer & Kylling, 2005). Amongst others, libRadtran contains the above mentioned standard atmospheres (Anderson *et al.*, 1986), the correlated-k method by Fu & Liou (1992), tables for the Raighley scattering properties by Bodhaine *et al.* (1999) and the OPAC desert aerosol profile (Hess *et al.*, 1998). LibRadtran's main tool is the uvspec program that computes radiances and irradiances for user specified input: the user can give atmospheric data to uvspec and then has various options to tell uvspec how to do the radiative transfer calculations on these data. The above specified atmosphere data were given to uvspec. As the correlated-k band parameterization by Fu & Liou (1992) was chosen, the horizontal irradiance at TOA is then taken from a libRadtran internally defined file specific for the band parameterization. The solar zenith angle is calculated for each grid box (lat,lon) and each time step t using the algorithm by Blanco-Muriel *et al.* (2001).
The *rodents*-algorithm (**RO**berts **D**elta-**E**ddingto**N** **T**wo-**S**tream) is applied to solve the radiative transfer equation. This algorithm was implemented in *libRadtran* by Robert Buras (LMU) following the delta-Eddington two-stream method described in Zdunkowski *et al.* (2007). The choice of this RTE solution method together with the band parameterization by Fu & Liou (1992, only 6 spectral bands) was motivated by:

1. It is aimed to simulate the ECHAM4 radiation code (two-stream, delta-Eddington approximation for the cloud covered fraction of the layers, only 2 spectral bands) as close as possible. It was already stated that the vertical properties of GCM clouds are not necessarily realistic. Nevertheless the GHI that ECHAM4 calculates with these uncertain clouds is good (Wild *et al.*, 1998). Hence, it is not meaningful to perform offline calculations that are most accurate for the given atmosphere (e.g. with a descrete ordinate solution method together with a higher resolved band parameterization like the correlated-k method by Kato *et al.* (1999, 31 bands)), but to perform offline calculations that yield the same GHI as the online calculations. A consistency check between the online calculation of GHI and offline calculations of GHI shows good agreement for the offline solution method described above (see section 3.4).

2. The solution method has to be fast as the calculations are performed for each 6-hourly time step for the years 1995-1999 and 2035-2039 (= 14000 time steps) and for every grid box (4608). This makes about 66 million calls to uvspec. Calculations with a two-stream method and a band parametrization with only 6 bands are less "expensive" than calculations using a discrete ordinate method solution method or a higher number of spectral bands.

Appendix A1 contains a uvspec input file template as used for the calculation of GHI and DHI for a single ECHAM4 box at a time t. Output of uvspec is the sum of the irradiances of the single spectral bands. If $0 < c_{tot} < 1$, the calculations were once performed for a cloudy atmosphere with cloud optical depth τ_{eff} and once for a clear sky atmosphere. The mean irradiance (GHI or DHI) of the whole box is calculated applying the independent column approximation (ICA):

$$E = c_{tot} \cdot E(\tau_{eff}) + (1 - c_{tot}) \cdot E(\tau_{eff} = 0) \ , \tag{36}$$

where $E(\tau_{eff})$ and $E(\tau_{eff} = 0)$ denote the irradiances calculated with and without the cloud in the atmosphere respectively. c_{tot} is the total cloud cover. This way GHI and DHI at the surface are calculated out of climate model atmosphere data. In order to obtain DNI, equation (12) is applied.

To handle the about 66 million calculations a loop over the time steps of a year and all grid boxes was programmed in the script language python (see Appendix A2: Python loop for one year). The calculations were performed on the eight core computer lx002 at DLR. The calculations of one model year needed about 10 days. As up to seven years could be started parallel (one CPU was left for other users), 20 days were sufficient to calculate irradiances for 10 years. A global data set for GHI and DNI at the surface was produced for the years 1995 - 1999 and 2035 - 2039. The horizontal resolution is about 3.75° latitude x 3.75° longitude. The temporal resolution is 6-hourly. The data set has been named ISMAD (**I**rradiances at the **S**urface derived from **M**odeled **A**tmosphere **D**ata).

3.4 Consistency check

This section contains a consistency check between the offline calculations (= the radiative transfer calculations performed after the GCM run) and the online calculations (= the radiative transfer calculations performed by the ECHAM4 radiation code during the model run, described in section 3.1.2): the offline calculated GHI is compared to the online calculated GHI (no DNI is produced by ECHAM4).
The offline calculations in this section differ from the calculations described above in two points:

1. The ECHAM4 aerosol climatology (Tanré *et al.*, 1984) is used instead of the ECHAM5 aerosols. The aerosols are given as total aerosol optical depth. The same way as

for ECHAM5 aerosols, the vertical distribution and scattering and absorption properties are assumed to be those of the OPAC desert profile. The reason for taking the ECHAM4 aerosols here is that the consistency of the two radiation codes shall be checked. Therefore, deviations due to using different aerosols are not wanted.

2. A -20 minutes time shift relative to ECHAM4 time is done. In fact, a comparison between single time step maps of the offline and online calculations (not shown) revealed best match for this time shift. The reason for this behavior can probably be found in the difficult synchronisation of data within a model time step, see section 3.1.1. A comparison of the offline and online solar zenith angles at TOA (not shown) reveals a -24 minutes difference what corresponds exactly to the internal model time step. So the GHI stored at time t is most probably the radiation of the time $t - 24\,\text{min}$. What leads to the four minutes shift between TOA and the surface could not be identified.

Moreover, different RTE solution methods and distinct band parameterizations were tested. GHI maps (not shown) for a single time step (January, 1st 1995) were calculated applying three different methods: a discrete ordinate method (Mayer & Kylling, 2005, "disort") combined with the band parameterization by Fu & Liou (1992) (DF), the *rodents* algorithm combined with the method by Fu & Liou (1992) (RF) and *rodents* together with another correlated-k method with higher band number provided by Kato *et al.* (1999, 31 bands) (RK). For all three methods the cloud optical properties were the same as used by ECHAM4 (mixed-phase, constant within the two ECHAM4 spectral bands). The differences between the offline calculated GHI global mean values and the ECHAM4 online calculated GHI global means revealed that all three methods lead to a few percent larger values (all $< 6\,\%$) than the ECHAM4 online calculated global mean value ($175\,\text{Wm}^{-2}$). The method RF was chosen because it is computationally less expensive than DF or RK.
For the RF method offline radiative transfer calculations were performed for every time step of the year 1995. Figure 3.8 shows the 1995 mean GHI as calculated online (top map) and offline with the RF method (second map from the top). The two mean value maps look quite similar apart from those grid boxes located in the Tibetean plateau. The reason for deviations there is very simple: In the offline calculations set-up clouds are generally located between 3 and 4 km above sea level. As the surface altitudes in the Tibetean plateau reach up to about 5 km, the clouds are "beneath the ground" and not seen by the radiation. Hence, the offline calculated irradiances are too large. Unfortunately, the consistency check calculations were started at the same time as the main calculations of this work such that we will meet this problem again when presenting the results of the main calculations. The four maxima along the equator are a result of considering only four time steps a day. Single white dots in the offline calculated GHI map are caused by missing values. For the same reason single dark dots can be seen on the two bottom maps illustrating the absolute

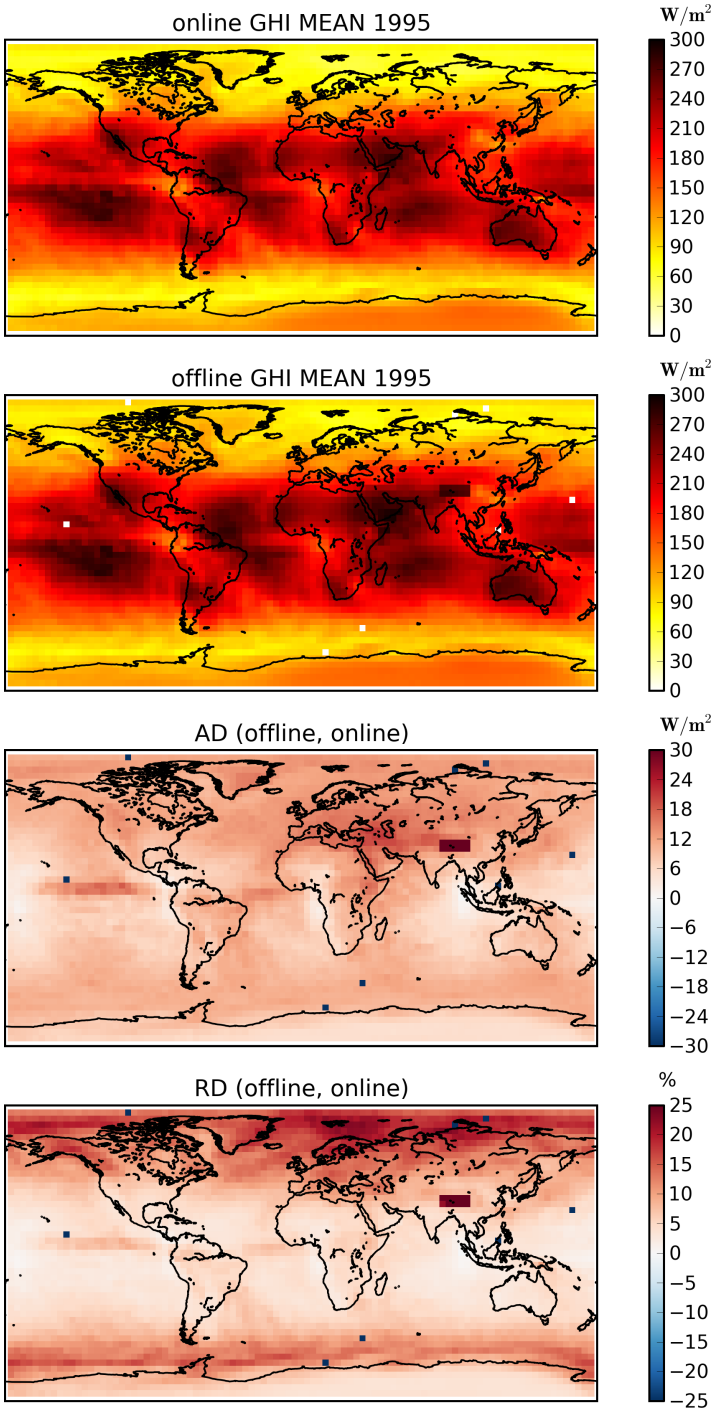

Figure 3.8: Comparison between online and offline calculated global horizontal irradiance (GHI): maps.

and relative differences between the offline and online calculated GHI. The global mean value of the offline GHI is 183 Wm^{-2} and thus 5 % higher than the online calculated GHI (174 Wm^{-2}). Global mean values were calculated as an area-weighted mean of all grid

boxes. Relative differences are smaller for low latitudes than for high latitudes.

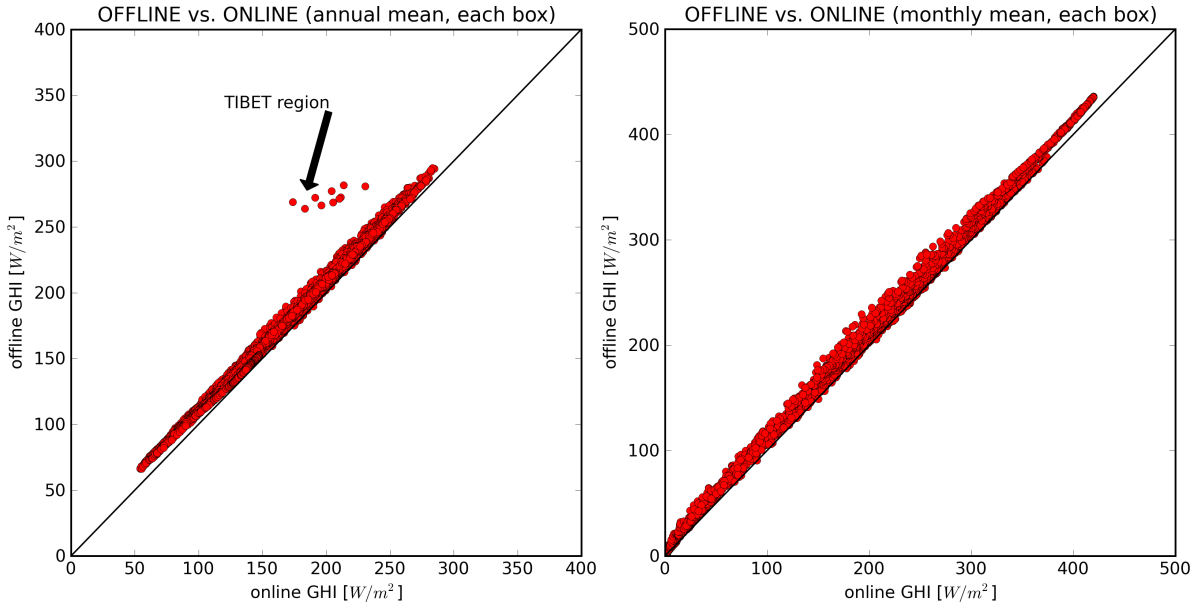

Figure 3.9: Comparison between online and offline calculated global horizontal irradiance (GHI): scatter plots. Left side: The offline calculated 1995 mean values of each ECHAM4 box are plotted versus their online calculated counterparts. Right side: Monthly mean values of each box offline vs. online.

The left panel of figure 3.9 shows the annual means of each box as scatterplot offline versus online. The small systematic deviation of the offline calculations towards larger values and the problem with the Tibet region calculations is illustrated once again. The right panel of the figure shows a scatterplot of monthly mean values. The value range of the offline and online calculations is wider due to considering seasonal variations of GHI by monthly values. In the monthly mean scatterplot the Tibet region problem is contained in the general deviations.

The systematic deviation of the offline GHI towards bigger values may be caused by the different cloud overlap assumptions made by the online and offline calculations: The offline calculations use the total cloud cover that is calculated according to the maximum random overlap (MRO) assumption. For the online calculations kind of a random overlap (RO) is assumed, when the total transmission to the ground is calculated by a combination of layer-averaged transmissions T_i and reflectances R_i (see section 3.1.2). Different cloud overlap assumptions may lead to different irradiances at the ground although the averaged transmittances through each layer may be the same. As the MRO assumption yields a smaller total cloud cover c_{tot} than the RO assumption (for the same cloud covers per layer c_i), this could be an explanation for the offline GHI being bigger than the online GHI.

The offline radiation algorithm is found to be consistent with the ECHAM4 radiation code apart from a small systematic deviation towards larger values: The offline calculated GHI is 5 % bigger than the online calculated GHI. The relative difference between offline and online calculated global irradiance is smaller than 5 % for low latitudes (not considering Tibet region), but higher for high latitudes (up to 25 %). Maybe this deviation makes the offline calculated GHI even more realistic than the ECHAM4 GHI, because the high absorption in clouds in ECHAM4 is - at least at higher latitudes - not supported by observational data (Wild *et al.*, 1998).

3.5 Comparison to measurement-derived irradiances

The ISMAD data of the past (1995 - 1999) is compared to a measurement based data set (Lohmann, 2006, ISIS). ISIS (**I**rradiances at the **S**urface derived from **IS**CCP cloud data) is a data set containing GHI and DNI for the years 1984 - 2004 that was generated by performing radiative transfer calculations on satellite-retrieved cloud data. Its temporal resolution is 3-hourly, spatial resolution is 2.5° x 2.5° at the equator. Latitudes are equidistant, longitude intervals enlarge towards higher latitudes such that the grid box areas remain approximately constant (280 km x 280 km).
For the ISIS calculations the same atmospheric standard profiles had been used as in this work (Anderson *et al.*, 1986), but different to this study measurement derived water vapor and ozone columns were included. Solar zenith angles were calculated following the Astronomic Almanach (1950 - 2050). Tropospheric aerosols (sulfate, dust, black carbon, sea salt) were considered via climatologic monthly mean column optical depth with a horizontal resolution of 4° x 5° based on aerosol transport models (NASA-GISS data set, Tegen *et al.* (1997)). The total aerosol optical depth of the NASA-GISS climatology is shown in figure 3.10. A comparison of the annual mean NASA-GISS aerosol optical depth to the 1995 - 1999 mean ECHAM5 aerosol optical depth (figure 3.5, top map) reveals differences in distribution and magnitude. ECHAM5 aerosols reach highest values up to around 1.0 over East Asia and up to about 0.8 over North Western Africa. This compares to an optical depth of approximately 0.4 and 0.2 for the same regions in the NASA-GISS data set. ECHAM5 models a Saharan dust plume that reaches far into and over the Altlantic with optical depth from about 0.5 to 0.6, where the NASA-GISS data set provides values around only 0.1. Over central Africa we find higher ECHAM5 values (around 0.5) than NASA-GISS values (< 0.2), too. Hence, we expect ISMAD irradiances to be smaller than ISIS irradiances for these regions (Central Africa, East Asia). Stratospheric aerosols (caused by high reaching volcanic eruptions) were included through monthly mean optical depths derived from satellite measurements with a zonal resolution of 7.5° (Sato *et al.*, 1993). Between 1995 and

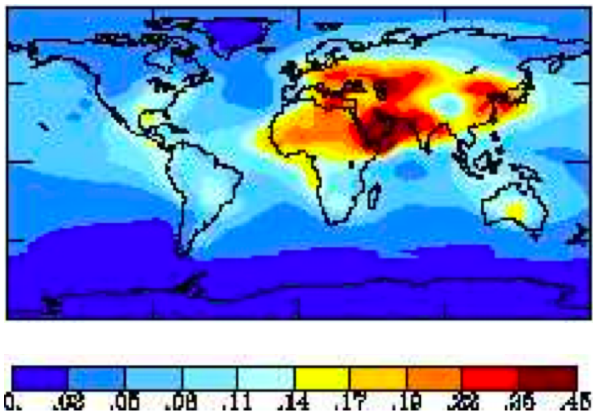

Figure 3.10: Annual mean aerosol optical depth of NASA-GISS aerosol climatology (Tegen *et al.*, 1997) used for ISIS calculations of irradiances.

2000 - four years after the last bigger volcanic eruption (Pinatubo 1991) - they have values of only < 0.02 and have negligibly small influence on irradiances.
The surface albedo is a satellite derived monthly mean. Cloud properties were taken from data provided by the International Satellite Cloud Climatology Project (ISSCP). Within this project data of up to five geostationary and two polar orbiting satellites are combined to give a global 3-hourly cloud data set. 15 different cloud types are distinguished (by height, water or ice cloud, optical depth range) and for each cloud type optical properties and fractional cloud cover c_i are given. Between 55°N and 55°S the data is provided by geostationary satellites, for higher latitudes data of polar orbiting satellites is taken. The maximal satellite zenith angle for each grid box is 72.5°. The radiative transfer equation was solved for a plane-parallel atmosphere using the two-stream method by Kylling *et al.* (1995). For direct radiation the Earth's spherical geometry is considered by including a correction factor for the solar zenith angle (Chapman factor) that leads to bigger direct irradiances at large solar zenith angles compared to non-spherical calculations like in the ISMAD method. A correlated-k band parameterization method was used (Kato *et al.*, 1999, 31 bands). The irradiance for a ISIS box is calculated with the irradiances $E_{cld,i}$ of the box fractions c_i that are covered with a cloud of type i and the irradiance E_{clr} of the clear-sky part of the box applying the independent column approximation:

$$E = \sum_{i=1}^{15} c_i \, E_{cld,i} + (1 - \sum_{i=1}^{15} c_i) \, E_{clr} \; . \tag{37}$$

ISIS itself has been validated against ground measurements: a comparison of multi-year monthly mean values with ground measurements (89 stations, highest station density in Europe and West USA) revealed that ISIS GHI fits very well (the slope of the regression line is 1.0), ISIS DNI tends to be slightly too small (slope of the regression line = 0.83). The reason for underestimated direct irradiances may be found in the cloud retrieval by

geostationary satellites: The satellite zenith angle increases towards higher latitudes what can lead to an overestimation of the cloud cover of 10 - 15 % (Lohmann, 2006, (Rossow & Garder, 1993; Wielicki & Parker, 1992) therein). Overestimated cloud cover leads to underestimated irradiances. As DNI is more sensitive to cloud cover than GHI, particularly direct irradiances are underestimated and we expect ISMAD irradiances to be higher than ISIS irradiances at midlatitudes, where ISCCP clouds are retrieved under high satellite zenith angles. In desert regions another effect can additionally lead to underestimated irradiances: Dust storms are recognised as clouds by the ISCCP cloud retrieval (Lohmann, 2006; Stubenrauch *et al.*, 1999). Thus, when including extra aerosols into the radiation calculations as done in the ISIS calculations, the extinction of the atmosphere is overestimated and the resulting irradiances become too small.
To compare ISMAD and ISIS data, the temporal and spatial resolution of ISIS had to be adjusted. ISIS is stored as ASCII-files, one file for each grid box containing a time column and a column of the corresponding irradiances. In order to adjust the ISIS horizontal resolution (2.5° x 2.5° at the equator, equidistant latitudes, longitude intervals enlarge towards high latitudes) to the ISMAD resolution (3.75° x 3.75° at the equator, equidistant longitudes, latitude intervals get smaller towards the poles), the ISIS data was in a first step written on a NetCDF-file with equidistant latitudes and longitudes (2.5° x 2.5°). The irradiance value for a grid box on the equidistant grid is that of the ISIS box with the same latitude and the longitude closest to that of the the new grid. Then, the ISIS irradiances on the created NetCDF-file were conservatively remapped on the ISMAD grid (Jones, 1999). 6-hourly values were extracted that correspond to the temporal resolution of the ISMAD data set (00:00, 06:00, 12:00, 18:00 GMT). Both 6-hourly resolved data sets, ISIS as well as ISMAD, were transformed to build local noon data (see section 3.2.1).

3.5.1 At the grid box-scale

At first, ISMAD and ISIS irradiances for single grid boxes are compared in order to reveal systematic differences between them. Figure 3.11 shows maps of ISIS local noon 1995 - 1999 mean values of global horizontal irradiance (left side) and direct normal irradiance (right side), as well as absolute differences (AD) and relative differences (RD) between ISMAD and ISIS irradiances (relative to ISIS). The bottom maps show where differences are significant. On the ISIS GHI mean map (top left map) four maxima along the equator can be identified which are caused by the composition of local noon data. This pattern cannot be seen on the DNI map (top right map), because the term $1/cos\vartheta_0$ in the calculation of DNI (compare to equation (12)) makes DNI vary less than GHI with the solar zenith angle. The ISIS GHI global mean value is 526 Wm^{-2}. The global mean of DNI is 335 Wm^{-2} (be aware

of that these are local noon values).

On the maps illustrating the differences between ISMAD and ISIS various patterns can be noticed, over land as well as over sea. As we are interested in irradiances for solar power generation, it is focused on differences between ISMAD and ISIS over land.

Firstly, we meet again the Tibet region problem where ISMAD irradiances are too high due

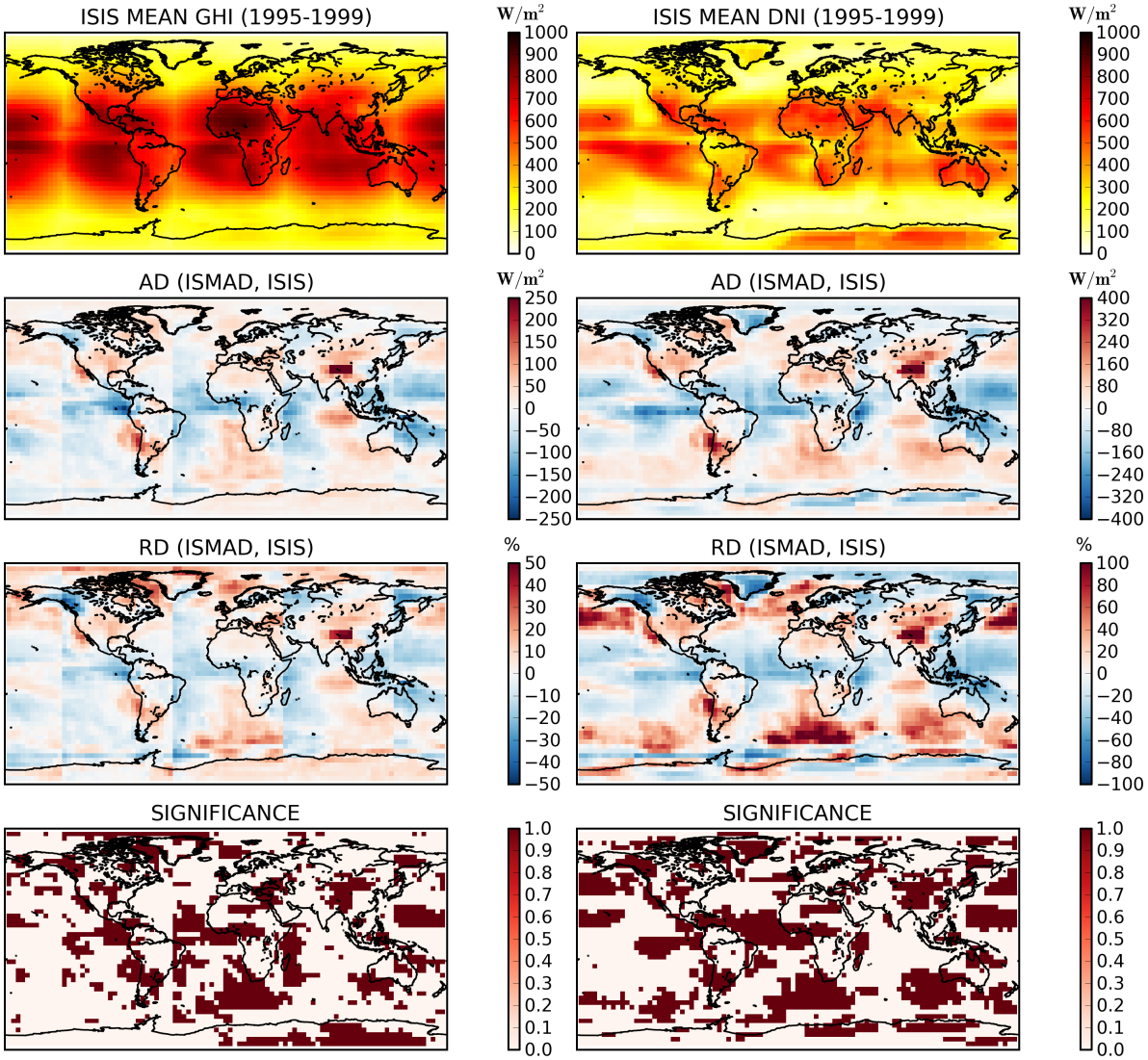

Figure 3.11: Grid box-resolved comparison of ISIS and ISMAD local noon data. Left side: Global horizontal irradiance; right side: Direct normal irradiance.

to the missing clouds. Secondly, for regions at midlatitudes, like Europe or USA, ISMAD irradiances tend to be higher than ISIS irradiances. As stated above this is probably an ISIS problem, as the ISCCP cloud retrieval overestimates the cloud amount for high satellite zenith angles which is the case when geostationary satellites retrieve clouds at midlatitudes. Thus, ISIS underestimates irradiances at midlatitudes. Lohmann (2006) compared

the ISCCP cloud cover to the cloud cover of the European Cloud Climatology (ECC, satellite based, resolution 1 km x 1 km, Meerkötter *et al.* (2004)). ISCCP cloud cover was found to lay 14 % over the ECC values, with even bigger differences over land. A comparison of ISCCP cloud cover to SYNOP (Surface SYNOPtic Observations) showed that ISCCP cloud cover over France is 6 % too high (Lohmann, 2006). As GHI and in particular DNI are very sensitive to cloud cover, ISIS GHI and particularly DNI are most likely too low over Europe. Moreover, Wild *et al.* (1998) showed that ECHAM4 cloud cover is in good agreement with data based on surface observations (Warren *et al.*, 1996) for mid- and low latitudes. The global mean of ECHAM4 cloud cover is with 0.60 in better agreement with surface observations (Warren *et al.*, 1996, 0.61) than the ISCCP global mean cloud cover with 0.63 (Wild *et al.*, 1998). This indicates that ISMAD irradiances are at midlatitudes probably better than ISIS irradiances.

Next, we can identify smaller ISMAD irradiances where the ECHAM5 aerosol optical depth used in the ISMAD calculations is larger than the NASA-GISS aerosol optical depth used by the ISIS method. This is particularly the case for the Saharan dust plume over Africa extending into the Atlantic and for anthropogenic pollution over East Asia. Stier *et al.* (2005) compared ECHAM5-HAM aerosol optical depths to measurement based optical depths (e.g. AERONET, MODIS(over water)-MISR(over land) composite) and showed that ECHAM5 aerosols tend to be too small over central Africa, but likely too big over East Asia. This means that ISMAD irradiances are probably better than ISIS irradiances in Africa but maybe too small in East Asia.

Finally, the DNI relative difference map illustrates that at high latitudes the ISMAD method computes smaller DNI than the ISIS method. The reason for this behavior lays probably in the different RTE solution methods applied by ISIS and ISMAD. ISIS applies a pseudo-spherical correction for the calculation of direct irradiances what leads to bigger values for high solar zenith angles, i.e. for high latitudes.

Generally, differences in GHI are smaller than differences in DNI. The cause for this is simply that direct irradiance is more sensitive to clouds and aerosols than global irradiance (see chapter 2), and thus differences between ISMAD and ISIS clouds and aerosols have stronger impact on direct irradiance.

Although figure 3.11 revealed various systematic differences between ISMAD and ISIS irradiances, global mean values do agree well: the global mean of ISMAD global horizontal irradiance is 517 Wm^{-2}. This value is only 2 % smaller than the ISIS global mean (526 Wm^{-2}). ISMAD DNI is with 325 Wm^{-2} as well only slightly smaller than ISIS DNI with 335 Wm^{-2} (3 %).

3.5.2 At the regional scale

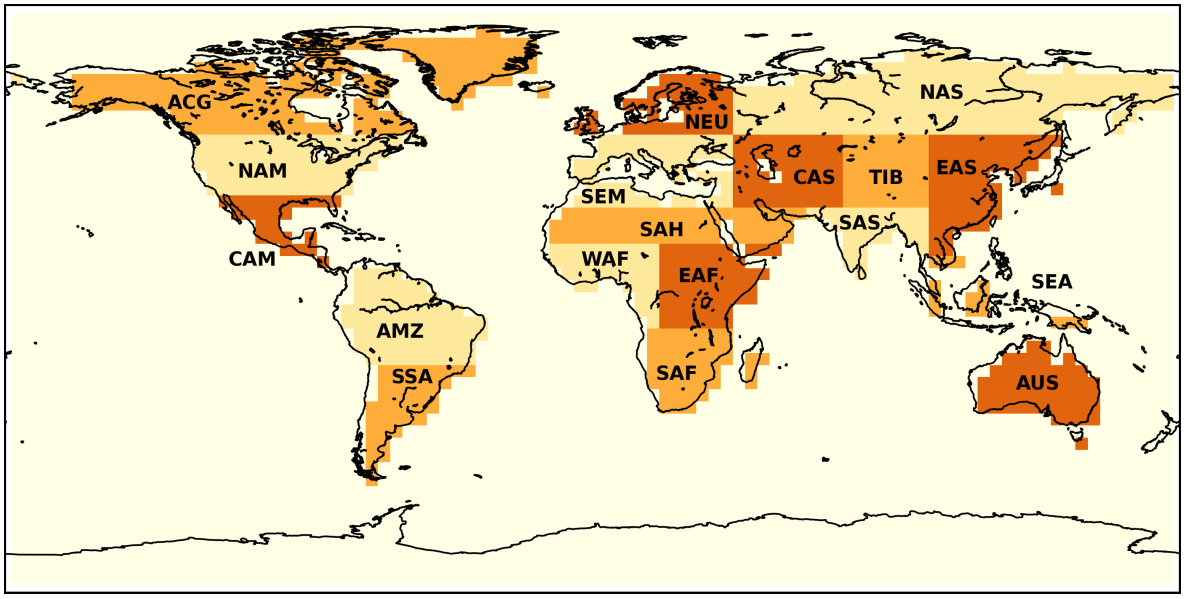

Figure 3.12: Illustration of the regions used for the calculation of regional mean values.

ACG	Alaska, Canada and Greenland
AMZ	Amazonia
AUS	Australia
CAM	Central America
CAS	Central Asia
EAF	East Africa
EAS	East Asia
NAM	North America
NAS	Northern Asia
NEU	Northern Europe
SAF	Southern Africa
SAH	Sahara
SAS	South Asia
SEA	Southeast Asia
SEM	Southern Europe and Mediterranean
SSA	Southern South America
TIB	Tibetan Plateau
WAF	West Africa

Regional mean values of ISMAD and ISIS irradances are compared, as ISMAD is derived from climate model data and climate models are designed to provide information about the atmosphere not on the grid box- but on the regional scale. We divide the Earth's continents

into 18 regions roughly following the arrangement done in IPCC (2007), see figure 3.12. Ocean regions are not considered because they are not relevant for solar power generation.

Figure 3.15 shows maps of ISIS regional mean values of global horizontal and direct normal irradiance (top maps), the relative difference of ISMAD to ISIS (relative to ISIS, middle maps) and significances (bottom maps). A comparison in numbers is given in table 3.1 for global horizontal irradiance and in table 3.3 for direct normal irradiance. The DNI table has an extra column that gives information about the percentage of days with DNI $> 200\,\mathrm{Wm}^{-2}$. As explained in chapter 2, for a "common" parabolic through power plant $200\,\mathrm{Wm}^{-2}$ is the threshold value to run the plant. d denotes the 1995-1999 percentage of days suitable for CSP operation derived from ISIS. Δd denotes the absolute difference between the ISMAD percentage of days with DNI $> 200\,\mathrm{Wm}^{-2}$ and the ISIS percentage of days with DNI $> 200\,\mathrm{Wm}^{-2}$ ($d_{ISMAD} - d_{ISIS}$).

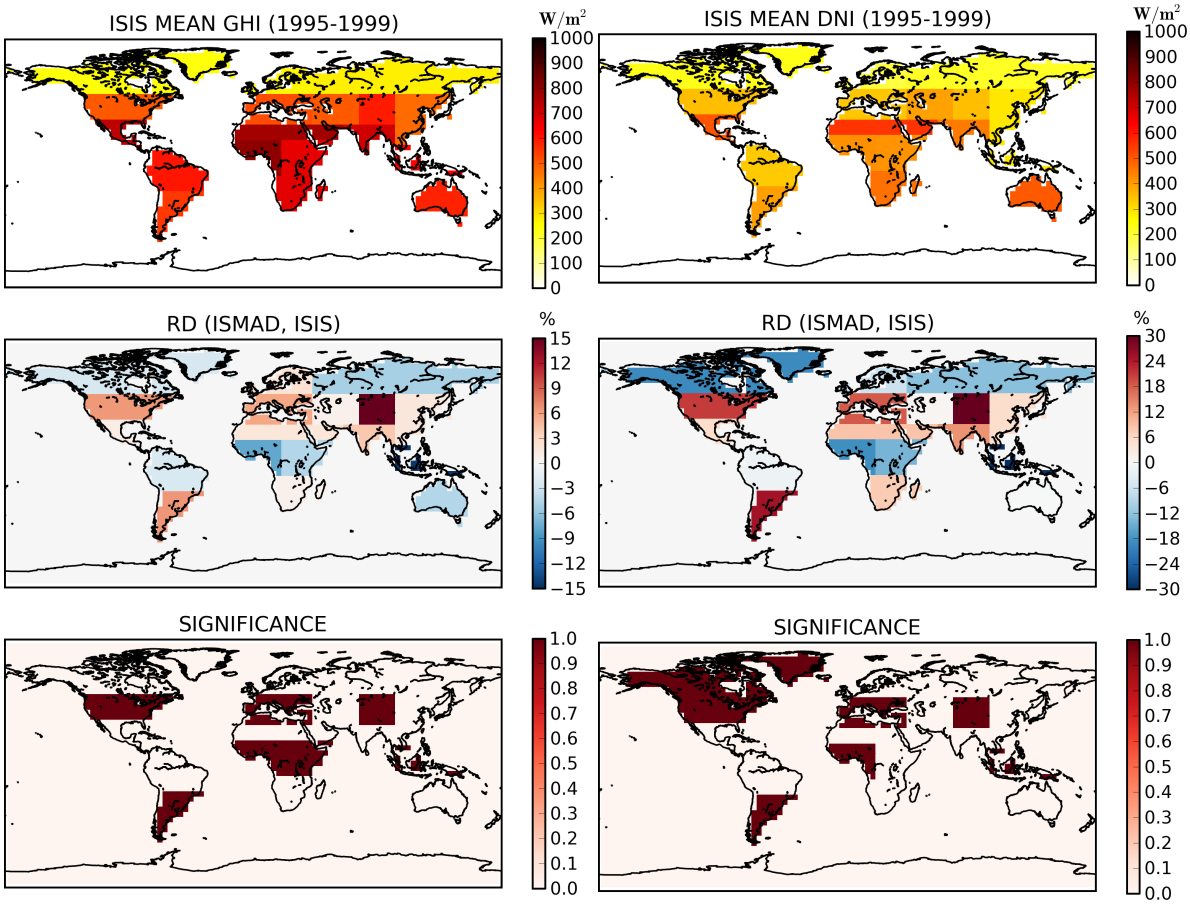

Figure 3.13

Figure 3.14

Figure 3.15: Comparison of ISIS and ISMAD local noon irradiances with regional resolution. Left panel: global horizontal irradiance; right panel: Direct normal irradiance.

The patterns revealed by the grid box-resolved comparison in the last section can of course again be found here. A first view at the relative differences between ISMAD and ISIS again shows that on the Tibetean Plateau ISMAD irradiances are irreasonably too high due to the missing clouds there. For the following comparison between ISMAD and ISIS the Tibet region is therefore not considered.
For ten of the 17 regions ISMAD global horizontal irradiance is bigger than ISIS global irradiance. For Southern South America (7 %), Southern Europe and Mediterranean region (6 %) and North America (6 %) differences are significant. For the same ten regions ISMAD direct irradiances as well are higher than their corresponding ISIS values. The deviations are about three times stronger, and again it is Southern South America (25 %), North America (21 %), and Southern Europe and Mediterranean region (18 %) where differences are significant. All these regions have in common to be located at midlatitudes where the ISIS method tends to underestimate irradiances.
Smaller values for ISMAD irradiances compared to ISIS irradiances are found on the one hand side for regions at high latitudes (ACG and NAS), on the other hand side for Central Africa and South-East Asia: ISMAD GHI in South-East Asia is 14 % smaller than ISIS GHI, in West Africa ISMAD GHI is 8 % smaller and in East Africa 4 % (all significant). In South-East Asia we find even 33 % less DNI for ISMAD than for ISIS (significant), in West Africa 18 % (significant), in East Africa 14 % (not significant). The differences in Africa are most probably caused by the higher ECHAM5 aerosol optical depth applied by the ISMAD method compared to the NASA-GISS aerosol climatology used by ISIS. The reason for the differences in South-East Asia could not clearly be identified, but at least partly this may be a result of the different horizontal resolutions of ISIS and ISMAD: The ISIS horizontal resolution is originally higher than the ISMAD resolution and may thereby better account for the small (compared to model resolution) South-East Asian islands. ECHAM4 calculates with averaged properties of each grid box. It is always problematic if a grid box contains land and sea like the ECHAM4 grid boxes of South-East Asia because atmospheric properties over land may strongly differ from the properties over sea and "averaging" leads to bad results.
Notable differences in the number of days with DNI $> 200\,\mathrm{Wm}^{-2}$ were found: For all regions apart from the South Europe and Mediterranean region, ISMAD counts less days suitable for CSP operation than ISIS does.

Globally, the ISMAD and ISIS irradiances agree well: ISMAD global horizontal irradiance is only 2 % smaller than ISIS global irradiance; ISMAD direct normal irradiance is 3 % smaller than the global ISIS value. But on the regional and grid box-scale significant differences occur. Most differences could be identified to be most probably either a result of the distinct aerosols used by the ISMAD and ISIS method or to come from underestimated ISIS

GHI (1995-1999)							
		ISMAD		ISIS			
Region	Month	Mean $[W/m^2]$	STD $[W/m^2]$	Mean $[W/m^2]$	STD $[W/m^2]$	AD $[W/m^2]$	RD [%]
ACG	**annual**	**242.73**	**2.65**	**249.04**	**3.61**	**-6.31**	**-3**
AMZ	**annual**	**588.14**	**5.02**	**602.95**	**5.85**	**-14.87**	**-2**
AUS	Jan	642.76	45.10	725.83	14.25	-83.07	-11
	Feb	581.70	68.40	682.92	27.64	-101.22	-15
	Mar	600.18	46.04	634.21	21.87	-34.03	-5
	Apr	517.22	41.34	529.99	19.98	-12.77	-2
	May	450.37	26.68	421.96	22.50	28.41	7
	Jun	389.76	22.37	373.94	11.95	15.82	4
	Jul	357.33	20.36	389.29	21.36	-31.96	-8
	Aug	473.94	28.35	494.48	12.75	-20.54	-4
	Sep	591.11	38.59	610.98	16.72	-19.87	-3
	Oct	685.54	74.95	691.71	12.89	-6.17	-1
	Nov	727.92	26.27	729.30	21.78	-1.38	0
	Dec	684.01	35.83	723.60	10.70	-39.59	-5
	annual	**558.49**	**19.53**	**584.06**	**5.69**	**-25.57**	**-4**
CAM	Jan	600.25	39.30	567.07	20.95	33.18	4
	Feb	690.43	42.31	653.10	23.74	37.33	6
	Mar	817.10	42.12	769.18	13.71	47.92	6
	Apr	861.00	18.22	854.15	33.94	6.85	1
	May	872.75	38.95	894.27	19.06	-21.52	-2
	Jun	795.18	44.07	853.97	18.74	-58.79	-7
	Jul	795.58	42.76	830.66	14.63	-35.08	-4
	Aug	829.14	36.15	804.71	24.85	24.43	3
	Sep	715.06	37.44	742.28	17.16	-27.22	-4
	Oct	732.32	55.79	682.95	18.42	49.37	7
	Nov	599.78	27.25	597.39	22.92	2.39	0
	Dec	571.29	58.52	534.98	16.22	36.31	7
	annual	**739.99**	**6.71**	**732.06**	**8.59**	**7.93**	**1**
CAS	**annual**	**507.33**	**6.16**	**503.20**	**4.19**	**4.13**	**1**
EAF	**annual**	**639.62**	**10.56**	**669.00**	**3.76**	**-29.38**	**-4**
EAS	**annual**	**484.47**	**9.37**	**476.26**	**5.75**	**8.21**	**2**
NAM	**annual**	**536.46**	**7.59**	**503.90**	**5.35**	**32.56**	**6**
NAS	**annual**	**263.72**	**5.07**	**277.71**	**4.83**	**-13.99**	**-5**
NEU	**annual**	**274.22**	**6.05**	**268.17**	**7.35**	**6.05**	**2**
SAF	**annual**	**683.90**	**17.25**	**678.67**	**6.30**	**5.23**	**1**

Table 3.1: Comparison of ISMAD and ISIS global horizontal irradiance for the years 1995 - 1999.
Notes:
- Be aware of that these are daily local noon data (for explanation see section 3.2.1).
- The abbreviations of the regions are explained in figure 3.12 on page 60.
- The absolute difference (AD) is ISMAD - ISIS. The relative difference (RD) is (ISMAD - ISIS) / ISIS.
- Mean, standard deviation (STD) and significance are defined in section 3.2.2.
- Significant differences are illustrated by red colored cells, if ISMAD GHI is bigger than ISIS GHI; blue colored cells for ISMAD GHI smaller than ISIS GHI.

GHI (1995-1999)							
		ISMAD		ISIS			
Region	Month	Mean $[W/m^2]$	STD $[W/m^2]$	Mean $[W/m^2]$	STD $[W/m^2]$	AD $[W/m^2]$	RD [%]
	Jan	645.66	14.85	606.50	8.40	39.16	6
	Feb	743.91	22.29	705.66	12.67	38.25	5
	Mar	808.92	49.91	790.44	13.12	18.48	2
	Apr	882.74	17.86	872.01	12.81	10.73	1
	May	892.19	22.43	881.71	19.20	10.48	1
	Jun	901.86	16.91	896.67	12.85	5.19	1
SAH	Jul	862.90	16.16	884.93	11.29	-22.03	-2
	Aug	819.08	29.02	855.29	11.30	-36.21	-4
	Sep	836.63	14.40	814.75	5.86	21.88	3
	Oct	762.89	24.20	742.08	16.39	20.81	3
	Nov	644.10	31.30	634.00	7.41	10.10	2
	Dec	614.92	19.81	561.95	21.67	52.97	9
	annual	**784.65**	**6.59**	**770.31**	**5.06**	**14.34**	**2**
SAS	**annual**	**735.24**	**19.48**	**706.60**	**11.98**	**28.64**	**4**
SEA	**annual**	**542.78**	**10.80**	**634.59**	**25.56**	**-91.81**	**-14**
	Jan	291.13	11.06	288.67	10.12	2.46	1
	Feb	404.38	9.69	414.17	16.80	-9.79	-2
	Mar	538.65	20.03	537.73	20.03	0.92	0
	Apr	664.90	20.71	615.05	14.76	49.85	8
	May	749.50	9.21	687.15	20.17	62.35	9
	Jun	806.99	12.52	742.50	17.60	64.49	9
SEM	Jul	819.57	22.42	759.62	21.69	59.95	8
	Aug	759.42	14.65	698.66	20.71	60.76	9
	Sep	610.06	22.01	563.32	27.17	46.74	8
	Oct	444.41	19.22	439.06	17.49	5.35	1
	Nov	300.60	14.03	295.76	7.30	4.84	2
	Dec	251.63	13.03	235.37	10.78	16.26	7
	annual	**553.44**	**5.93**	**522.93**	**5.87**	**30.51**	**6**
SSA	**annual**	**589.43**	**6.00**	**552.93**	**7.10**	**36.5**	**7**
(TIB	**annual**	**722.01**	**4.23**	**597.19**	**13.09**	**124.82**	**21)**
WAF	**annual**	**741.06**	**9.07**	**803.87**	**3.24**	**-62.81**	**-8**

Table 3.2: Continuation of table 3.1.

DNI (1995-1999)								
		ISMAD		ISIS				
Region	Month	Mean $[W/m^2]$	STD $[W/m^2]$	Mean $[W/m^2]$	STD $[W/m^2]$	AD $[W/m^2]$	RD [%]	Δd/d [%]/[%]
ACG	**annual**	**187.76**	**4.93**	**232.02**	**3.80**	**-44.26**	**-19**	**-17 / 44**
AMZ	**annual**	**327.53**	**6.89**	**332.30**	**8.05**	**-4.77**	**-1**	**-15 / 70**
AUS	Jan	433.22	63.39	483.43	30.01	-50.21	-10	-20 / 79
	Feb	426.81	89.89	469.18	53.44	-42.37	-9	-20 / 76
	Mar	537.93	56.04	531.98	57.66	5.95	1	-13 / 83
	Apr	527.02	81.27	534.29	52.76	-7.27	-1	-11 / 81
	May	540.64	78.03	484.11	59.21	56.53	12	-4 / 78
	Jun	498.19	52.19	473.59	37.56	24.60	5	-9 / 82
	Jul	402.10	52.02	466.08	54.58	-63.98	-14	-20 / 81
	Aug	516.23	43.85	537.88	39.94	-21.65	-4	-16 / 88
	Sep	564.03	67.16	562.40	40.92	1.63	0	-12 / 88
	Oct	566.01	97.18	542.59	26.44	23.42	4	-8 / 84
	Nov	552.02	31.57	496.28	34.32	55.74	12	-5 / 80
	Dec	471.34	63.75	460.16	12.00	11.18	2	-11 / 75
	annual	**502.96**	**29.89**	**503.74**	**10.94**	**-0.78**	**0**	**-12 / 81**
CAM	Jan	536.46	84.40	523.91	59.76	12.55	2	-9 / 80
	Feb	556.75	54.44	502.22	45.73	54.53	11	-8 / 80
	Mar	615.27	79.16	541.16	33.90	74.11	14	-6 / 84
	Apr	579.42	62.50	561.59	58.16	17.83	3	-12 / 86
	May	552.75	49.06	560.30	40.31	-7.55	-1	-18 / 90
	Jun	494.00	50.05	501.30	35.54	-7.3	-1	-20 / 87
	Jul	432.66	55.35	474.20	22.68	-41.54	-9	-21 / 87
	Aug	511.80	44.81	458.12	46.72	53.68	12	-12 / 85
	Sep	466.07	41.69	449.44	27.66	16.63	4	-14 / 80
	Oct	622.04	73.22	517.88	40.98	104.16	20	-2 / 80
	Nov	537.60	48.38	526.62	45.85	10.98	2	-12 / 82
	Dec	552.21	118.54	499.81	39.12	52.4	10	-8 / 81
	annual	**538.09**	**11.96**	**509.85**	**19.17**	**28.24**	**6**	**-12 / 84**
CAS	**annual**	**396.25**	**12.80**	**393.74**	**10.92**	**2.51**	**1**	**-13 / 74**
EAF	**annual**	**359.15**	**12.56**	**417.48**	**14.99**	**-58.33**	**-14**	**-17 / 78**
EAS	**annual**	**306.24**	**10.85**	**290.71**	**7.34**	**15.53**	**5**	**-4 / 55**
NAM	**annual**	**420.48**	**17.36**	**347.88**	**15.83**	**72.60**	**21**	**-4 / 60**
NAS	**annual**	**190.74**	**5.90**	**217.82**	**8.99**	**-27.08**	**-12**	**-11 / 41**
NEU	**annual**	**177.78**	**9.60**	**189.93**	**12.12**	**12.15**	**6**	**-5 / 36**
SAF	**annual**	**500.87**	**25.06**	**464.99**	**15.38**	**35.88**	**8**	**-8 / 79**

Table 3.3: Comparison of ISMAD and ISIS direct normal irradiance for the years 1995 - 1999.
Notes:
- Be aware of that these are daily local noon data (for explanation see section 3.2.1).
- The abbreviations of the regions are explained in figure 3.12 on page 60.
- The abolute difference (AD) is ISMAD - ISIS, the relative difference (RD) is (ISMAD - ISIS) / ISIS.
- Mean, standard deviation (STD) and significance are defined in chapter 3.2.2.
- Significant differences are illustrated by red colored cells, if ISMAD GHI is bigger than ISIS GHI; blue colored cells for ISMAD GHI smaller than ISIS GHI.
- d refers to the ISIS percentage of days with DNI $> 200\,\mathrm{Wm}^2$. $\Delta d = d_{ISMAD} - d_{ISIS}$.

DNI (1995-1999)								
		ISMAD		ISIS				
Region	Month	Mean [Wm^{-2}]	STD [Wm^{-2}]	Mean [Wm^{-2}]	STD [Wm^2]	AD [Wm^2]	RD [%]	Δd/d [%] / [%]
SAH	Jan	634.04	75.36	571.31	27.28	62.73	11	-4 / 89
	Feb	659.10	51.86	537.24	28.28	121.86	23	-1 / 85
	Mar	582.99	128.04	484.54	58.92	98.45	20	-4 / 83
	Apr	583.26	50.15	512.94	45.52	70.32	14	-4 / 84
	May	593.32	36.70	512.12	45.05	81.20	16	-3 / 85
	Jun	590.89	43.86	561.21	30.86	29.68	5	-3 / 93
	Jul	516.29	26.21	554.86	24.11	-38.57	-7	-9 / 94
	Aug	465.48	49.34	543.40	38.81	-77.92	-14	-11 / 91
	Sep	626.84	41.40	579.51	18.08	47.33	8	-1 / 93
	Oct	692.19	71.60	633.56	61.44	58.63	9	-4 / 92
	Nov	620.27	67.80	625.29	20.84	-5.02	-1	-10 / 91
	Dec	672.74	62.75	548.29	57.57	124.45	23	1 / 84
	annual	**603.12**	**15.50**	**555.33**	**17.66**	**47.79**	**9**	**-4 / 88**
SAS	**annual**	**513.46**	**23.92**	**452.38**	**26.71**	**61.08**	**14**	**-2 / 74**
SEA	**annual**	**193.18**	**8.88**	**289.39**	**25.56**	**-96.21**	**-33**	**-28 / 59**
SEM	Jan	276.02	22.12	276.58	20.27	-0.56	0	-6 / 50
	Feb	330.11	12.90	316.23	27.76	13.88	4	-6 / 55
	Mar	396.06	28.59	321.35	34.26	47.71	15	3 / 54
	Apr	431.17	38.68	308.60	24.08	122.57	40	11 / 53
	May	452.34	8.60	332.57	29.72	119.77	36	11 / 61
	Jun	502.85	25.76	398.68	27.24	104.17	26	9 / 70
	Jul	558.94	29.66	457.20	37.48	101.74	22	8 / 77
	Aug	528.70	32.47	427.53	46.10	101.17	24	9 / 75
	Sep	457.59	30.08	346.59	41.23	111.00	32	11 / 62
	Oct	348.40	37.66	338.21	32.70	10.19	3	0 / 60
	Nov	264.33	26.37	286.99	23.40	-22.66	-8	-6 / 51
	Dec	252.27	22.24	245.89	23.41	6.38	3	-6 / 46
	annual	**399.90**	**8.90**	**337.89**	**10.33**	**62.01**	**18**	**3 / 60**
SSA	**annual**	**498.56**	**6.90**	**398.35**	**10.22**	**100.21**	**25**	**-4 / 70**
(TIB	**annual**	**636.30**	**13.23**	**348.17**	**18.62**	**288.13**	**83**	**8 / 66)**
WAF	**annual**	**344.51**	**12.56**	**421.73**	**8.41**	**-77.22**	**-18**	**-11 / 74**

Table 3.4: Continuation of table 3.3.

irradiances (at midlatitudes). Probably ISMAD is even better than ISIS for some regions. Where ISMAD might have problems is: large latitudes, South-East Asia and the percentage of days with DNI $> 200\,\mathrm{Wm}^{-2}$ (plus Tibet region of course).

4 Results: Estimated Changes of Irradiances

In this chapter the ISMAD (**I**rradiances at the **S**urface derived from **M**odeled **A**tmosphere **D**ata) data set that was generated in this work is presented and discussed. The grid box-resolved irradiance data is shortly presented to identify those atmospheric parameters presented in section 3.2 that lead to changes of the global horizontal and direct normal irradiance. But as ISMAD is based on climate model data, focus lies on 5-yearly regional mean values. The absolute values of the 1995 - 1999 regional means are presented to identify those regions that are most suitable for solar power generation. In order to provide information about future changes of solar resources due to the evolution of the modeled ECHAM4 clouds and ECHAM5 aerosols, the 2035 - 2039 mean global horizontal and direct normal irradiances are compared to their corresponding 1995 - 1999 values. All irradiances are illustrated as local noon data (for explanation see section 3.2.1).

4.1 At the grid box-scale

The grid box-resolved 1995 - 1999 mean maps of the ISMAD global horizontal and direct normal irradiances are shown on the top panels of figure 4.1. Tibet region is again neglected in the following discussion.
The global horizontal irradiance depends more than the direct normal irradiance on the solar zenith angle. Therefore, the pattern of the composition of local noon data out of four daily time steps can be seen clearlier on the left map. Direct normal irradiance instead is more sensitive to clouds and aerosols and hence the spatial distribution of clouds and aerosols (see figures 3.4 and 3.5) is more apparent on the right map. The patterns of very low cloud amount over the Saharan region can for instance clearly be identified, as well as high aerosol optical depths over Central Africa and East Asia.
The 2nd and 3rd rows illustrate absolute and relative differences between future and past mean values, the bottom row shows where differences are significant. Irradiances increase in Europe and Australia. In Europe the maximal difference is around 30 %. In Central and

South Africa irradiances decrease. Here again we find future values up to 30 % smaller than in the past time period. A view on the relative difference between future and past cloud properties (figure 3.4, 3rd row from the top) can explain the increases of GHI and DNI in Australia: total cloud cover (as well as effective optical depth) are smaller in the 2035 - 2039 data than in the 1995 - 1999 data what leads to higher irradiances. The radiation reduction in Africa and the increase in Europe are a result of the evolution of aerosols. The smaller future aerosol optical depth over Europe leads to higher irradiances, the increasing aerosol amount over Africa (up to 150 %) strongly reduces irradiances there. As DNI is more than GHI sensitive to clouds and aerosols, maximal changes in DNI ($\pm$ 30 %) are more than twice as big as maximal changes in GHI ($\pm$ 12 %).
The global mean values of GHI and DNI are reduced in the future time period compared to the past time period: the 2035 - 2039 GHI mean value is with 508 Wm^{-2} 2 % smaller than the 1995 - 1999 value of 517 Wm^{-2}. Future DNI compares with 309 Wm^{-2} to past DNI with 325 Wm^{-2} what gives a decrease of 5 %. This behavior could be expected as the global mean value of the aerosol optical depth strongly increases (14 %); the total cloud cover increases slightly as well (0.3%).

4.2 At the regional scale

Figure 4.2 shows 5-yearly (1995 - 1999) regional mean values of local noon global horizontal and direct normal irradiance (top maps), the relative difference between the future (2035 - 2039) and past (1995 - 1999) mean values (relative to past means, middle maps) and where the differences are significant (bottom maps). The composition of local noon data is described in section 3.2.1. The arrangement of regions is illustrated in figure 3.12.
A comparison in numbers is given by table 4.1 for global horizontal irradiance and by table 4.3 for direct normal irradiance. The tables additionally provide monthly resolutions for four regions that are particularly relevant for solar power generation: Australia, Central America, Saharan Region, Southern Europe and Mediterranean region. The DNI table has an extra column that gives information about the percentage of days with DNI $> 200\,Wm^{-2}$. As explained in the physical background chapter, for a "common" parabolic through power plant 200 Wm^{-2} is the threshold value to run the plant. d denotes the (1995 - 1999) percentage of CSP suitable days. Δd denotes the absolute difference between the future (2035 - 2039) percentage of days with DNI $> 200\,Wm^{-2}$ and the past percentage of days with DNI $> 200\,Wm^{-2}$ ($d_{2035-2039} - d_{1995-1999}$). In the following the Tibet region is not considered as clouds were not included in the calculations there.

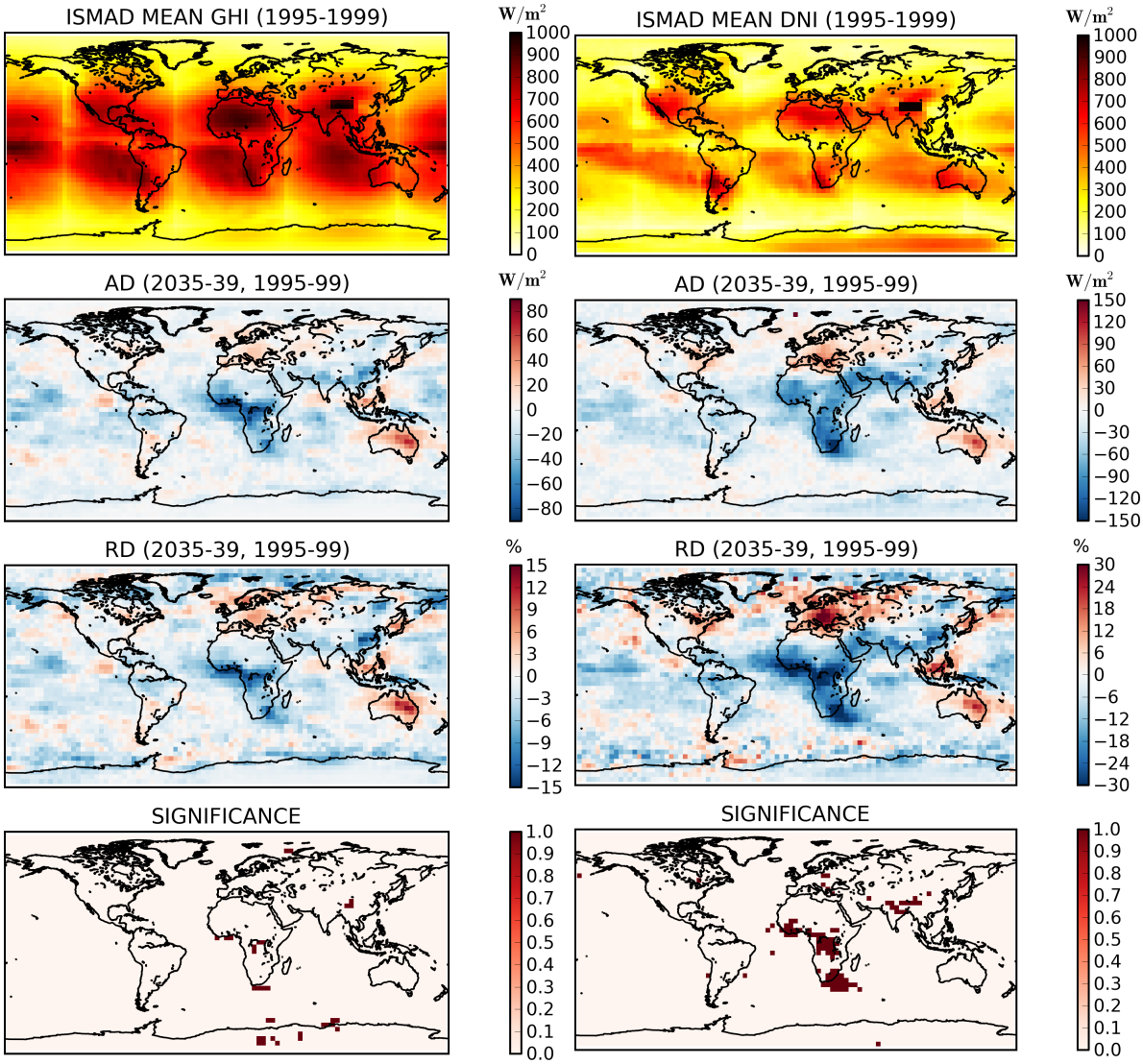

Figure 4.1: Comparison of ISMAD (2035-2039) local noon irradiances to ISMAD (1995 - 1999) local noon iradiances. Left side: Global horizontal irradiance; right side: Direct normal irradiance.

4.2.1 Absolute irradiances

The (1995 - 1999) absolute values of global horizontal irradiance are largest in the Saharan region (785 Wm^{-2}), West Africa (741 Wm^{-2}), Central America (740 Wm^{-2}) and South Asia (735 Wm^{-2}). Most direct normal irradiance can be clearly located again in the Saharan region (603 Wm^{-2}), followed by Central America (538 Wm^{-2}), South Asia (513 Wm^{-2}) and Australia (503 Wm^{-2}). Most days suitable for concentrating solar power plant operation (i.e. DNI $> 200\,Wm^{-2}$) is again found in the Saharan region (84 %). In Central America and South Asia we find 72 %, in Australia CSP works on 69 % of the days.

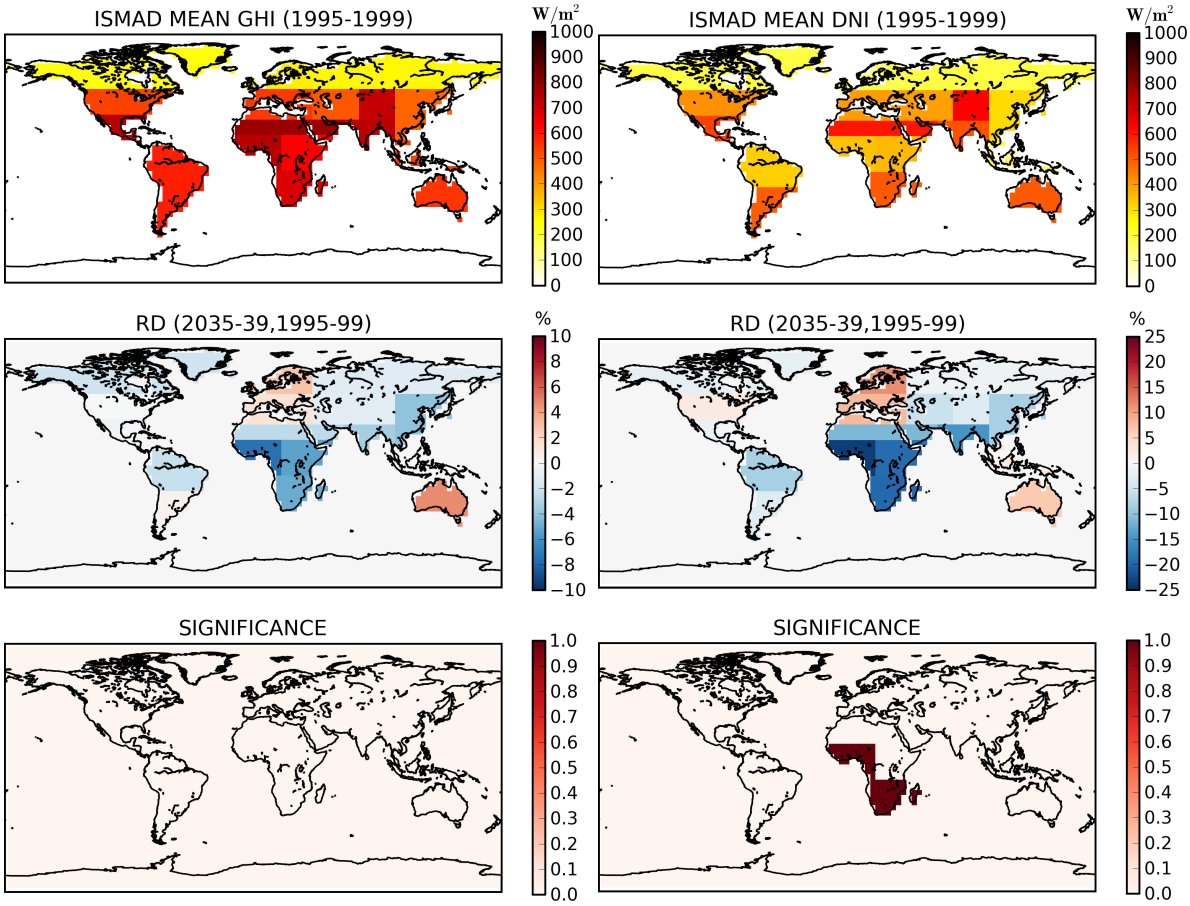

Figure 4.2: Comparison of ISMAD (2035 - 2039) local noon regional means to ISMAD (1995 - 1999) local noon regional means. Left side: Global horizontal irradiance; right side: Direct normal irradiance.

4.2.2 Comparison between future and past irradiances

As can be seen on the mid-left map of figure 4.2 the global horizontal irradiance between 2035 and 2039 is in 10 of the 17 regions smaller than their corresponding value from 1995 to 1999 (Tibet region is not considered). The direct normal irradiance decreases in 12 of the 17 regions. 10 regions have less days with DNI $> 200\,\mathrm{Wm}^{-2}$ in the future than in the past time period, see table 4.3. The strongest decrease of the number of days that are suitable for CSP operation is located in West Africa where the future percentage of days of 52 % compares with a value of 63 % for the past time period.

Largest relative differences of global and direct irradiance are located in Africa. Global horizontal irradiance decreases in West Africa from $741\,\mathrm{Wm}^{-2}$ to $686\,\mathrm{Wm}^{-2}$ (7 %), in South and East Africa a decrease of 5 % is found. The most notable increase of global irradiance

is located in Australia (5 %).
The direct normal irradiance in Africa decreases as well and stronger than the global irradiance does: in West and South Africa changes are significant (-23 % and -20 % respectively). In East Africa a reduction of 19 % is found, in the Saharan region the 2035 - 2039 value (535 Wm^{-2}) is 11 % smaller than the 1995 - 1999 value (603 Wm^{-2}). In Europe the direct normal irradiance increases the most: from 178 Wm^{-2} to 198 Wm^{-2} (12 %) in North Europe and from 340 Wm^{-2} to 432 Wm^{-2} (8 %) in Southern Europe and Mediterranean Region. In Australia the direct normal irradiance increases from 503 Wm^{-2} to 536 Wm^{-2} (7 %).

4.2.3 Saharan region

Most solar resources are located in the Saharan region, direct normal irradiance (1995 - 1999 mean: 603 Wm^{-2}) as well as global horizontal irradiance (785 Wm^{-2}). The DESERTEC project actually considers to implement concentrating solar power plants in this region.
The monthly resolution of the (1995 - 1999) mean values yields that GHI is largest in the months around June (the June value is 902 Wm^{-2}) and lowest in the months around December (the December mean GHI is 615 Wm^{-2}). Contrary, the direct normal irradiance is in all the months from September to February $> 620\,Wm^{-2}$, whereas it is $< 593\,Wm^{-2}$ in the months between March and August. No clear seasonal dependency can be found in the percentage of days suitable for CSP operation (DNI $> 200\,Wm^{-2}$): The biggest (1995 - 1999) mean value is found in September (92 %), the second largest value in June (90 %). The percentage of days is smallest in April and August (both 80 %).
ISMAD provides the same seasonal dependencies (or non-dependencies) for the mean values of the future time period (2035 - 2039), but irradiances are mostly reduced: Highest global irradiance is again found in the months around June (the June value is now 886 Wm^{-2}) and smallest GHI in the months around December (the December value is 585 Wm^{-2}). The seasonal variability of DNI remains reversed with highest values in winter and lowest values in summer.
The annual mean relative difference between (2035 - 2039) GHI and (1995 - 1999) GHI accounts for -5 %. GHI decreases strongest in September (-6 %). March is the only month with a slightly increased future GHI (1 %). The annual mean relative difference between (2035 - 2039) DNI and (1995 - 1999) DNI amounts to -11 %; a look at the monthly resolution reveals the same patterns as described for GHI, but stronger. The reduction is again strongest in September (-21 %) and March is the only month with a non-negative change of DNI (1 %).
The high winter DNI values should not be interpreted equivalently to high daily doses: The Saharan region is located in the Northern hemisphere, thus days are longer in the months

around July than in the months around January. As the ISMAD data were presented as local noon data they do not consider day length. High winter values should be only interpreted as high irradiances at local noontime. In principle, the daily dosis could be approximated with the ISMAD data set by weighting the ISMAD local noon data with day length.

ISMAD GHI							
		(1995-1999)		(2035-2039)			
Region	Month	Mean [Wm^{-2}]	STD [Wm^{-2}]	Mean [Wm^{-2}]	STD [Wm^{-2}]	AD [Wm^{-2}]	RD [%]
ACG	**annual**	**242.73**	**2.65**	**237.78**	**2.06**	**-4.95**	**-2**
AMZ	**annual**	**588.14**	**5.02**	**574.41**	**11.40**	**-13.73**	**-2**
AUS	Jan	642.76	45.10	719.58	54.63	76.82	12
	Feb	581.70	68.40	609.80	63.33	28.10	5
	Mar	600.18	46.04	639.75	62.53	39.57	7
	Apr	517.22	41.34	502.50	41.88	-14.72	-3
	May	450.37	26.68	446.86	40.81	-3.51	-1
	Jun	389.76	22.37	417.96	25.64	28.20	7
	Jul	357.33	20.36	403.79	22.91	46.49	13
	Aug	473.94	28.35	485.84	25.15	11.90	3
	Sep	591.11	38.59	635.68	26.05	44.57	8
	Oct	685.54	74.95	707.54	29.50	22.00	3
	Nov	727.92	26.27	720.91	30.75	-7.01	-1
	Dec	684.01	35.83	728.13	43.89	44.12	6
	annual	**558.49**	**19.53**	**584.86**	**20.77**	**26.37**	**5**
CAM	Jan	600.25	39.30	530.30	25.00	-69.95	-12
	Feb	690.43	42.31	688.72	37.35	-1.71	0
	Mar	817.10	42.12	819.66	30.54	2.56	0
	Apr	861.00	18.22	885.63	29.35	24.63	3
	May	872.75	38.95	861.82	33.86	-10.93	-1
	Jun	795.18	44.07	817.05	44.40	21.87	3
	Jul	795.58	42.76	775.58	47.83	-20.00	-3
	Aug	829.14	36.15	778.55	62.21	-50.59	-6
	Sep	715.06	37.44	769.91	43.46	54.85	8
	Oct	732.32	55.79	746.45	59.26	14.13	2
	Nov	599.78	27.25	637.17	35.05	37.39	6
	Dec	571.29	58.52	527.79	57.46	-43.50	-8
	annual	**739.99**	**6.71**	**736.55**	**20.30**	**-3.44**	**0**
CAS	**annual**	**507.33**	**6.16**	**501.44**	**4.21**	**-5.89**	**-1**
EAF	**annual**	**639.62**	**10.56**	**605.50**	**20.33**	**-34.12**	**-5**
EAS	**annual**	**484.47**	**9.37**	**465.10**	**4.13**	**-19.37**	**-4**
NAM	**annual**	**536.46**	**7.59**	**536.32**	**4.48**	**-0.14**	**0**
NAS	**annual**	**263.72**	**5.07**	**260.61**	**4.38**	**-3.11**	**-1**
NEU	**annual**	**274.22**	**6.05**	**282.20**	**6.56**	**7.98**	**3**
SAF	**annual**	**683.90**	**17.25**	**649.76**	**12.81**	**-34.14**	**-5**

Table 4.1: Comparison of ISMAD global horizontal irradiance for the years (1995 - 1999) and (2035 - 2039).
Notes:
- Be aware of that these are daily local noon data (for explanation see section 3.2.1).
- The Abbreviations of the regions are explained in figure 3.12 on page 60.
- Significance was calculated for annual values. No significant changes were found.

ISMAD GHI							
		(1995-1999)		(2035-2039)			
Region	Month	Mean [W/m^2]	STD [W/m^2]	Mean [W/m^2]	STD [W/m^2]	AD [W/m^2]	RD [%]
	Jan	645.66	14.85	629.74	11.16	-15.92	-2
	Feb	743.91	22.29	734.17	35.31	-9.74	-1
	Mar	808.92	49.91	819.61	33.93	10.69	1
	Apr	882.74	17.86	849.84	36.26	-32.9	-4
	May	892.19	22.43	878.09	21.77	-14.10	-2
	Jun	901.86	16.91	886.39	28.86	-15.47	-2
SAH	Jul	862.90	16.16	857.80	22.98	-5.10	-1
	Aug	819.08	29.02	798.64	23.20	-20.44	-2
	Sep	836.63	14.40	784.40	25.12	-52.23	-6
	Oct	762.89	24.20	722.15	29.22	-40.74	-5
	Nov	644.10	31.30	622.90	22.85	-21.2	-3
	Dec	614.92	19.81	585.10	15.08	-29.82	-5
	annual	**784.65**	**6.59**	**764.07**	**13.05**	**-20.58**	**-3**
SAS	**annual**	**735.24**	**19.48**	**710.42**	**8.91**	**-24.82**	**-3**
SEA	**annual**	**542.78**	**10.80**	**542.50**	**10.90**	**-0.28**	**0**
	Jan	291.13	11.06	293.18	16.41	2.05	1
	Feb	404.38	9.69	415.35	19.41	10.97	3
	Mar	538.65	20.03	553.54	17.26	14.89	3
	Apr	664.90	20.71	660.09	3.76	-4.81	-1
	May	749.50	9.21	759.66	28.61	10.16	1
	Jun	806.99	12.52	807.01	40.16	0.02	0
SEM	Jul	819.57	22.42	825.58	22.30	6.01	1
	Aug	759.42	14.65	770.86	25.55	11.44	1
	Sep	610.06	22.01	630.15	12.35	20.09	3
	Oct	444.41	19.22	465.94	17.31	21.53	5
	Nov	300.60	14.03	300.10	6.59	-0.5	0
	Dec	251.63	13.03	255.96	7.08	4.33	2
	annual	**553.44**	**5.93**	**561.45**	**8.20**	**8.01**	**1**
SSA	**annual**	**589.43**	**6.00**	**592.05**	**4.81**	**2.62**	**0**
(TIB	**annual**	**722.01**	**4.23**	**713.91**	**7.55**	**-8.10**	**-1)**
WAF	**annual**	**741.06**	**9.07**	**685.58**	**20.67**	**-55.48**	**-7**

Table 4.2: Continuation of table 4.1.

ISMAD DNI		(1995-1999)		(2035-2039)				
Region	Month	Mean [Wm^{-2}]	STD [Wm^{-2}]	Mean [Wm^{-2}]	STD [Wm^{-2}]	AD [Wm^{-2}]	RD [%]	Δd/d [%]/[%]
ACG	**annual**	**187.76**	**4.93**	**183.68**	**4.25**	**-4.08**	**-2**	**-1 / 27**
AMZ	**annual**	**327.53**	**6.89**	**300.34**	**10.98**	**-27.19**	**-8**	**-1 / 56**
AUS	Jan	433.22	63.39	510.46	61.28	77.24	18	11 / 59
	Feb	426.81	89.89	443.14	100.08	16.33	4	4 / 56
	Mar	537.93	56.04	601.98	107.13	64.05	12	5 / 70
	Apr	527.02	81.27	507.08	82.60	-19.94	-4	-2 / 70
	May	540.64	78.03	548.37	78.79	7.73	1	3 / 74
	Jun	498.19	52.19	557.22	52.84	59.03	12	9 / 73
	Jul	402.10	52.02	494.21	63.32	92.11	2	12 / 61
	Aug	516.23	43.85	532.32	47.07	16.09	3	3 / 72
	Sep	564.03	67.16	623.23	45.79	59.20	10	6 / 76
	Oct	566.01	97.18	576.81	59.93	10.80	2	3 / 76
	Nov	552.02	31.57	531.00	51.32	-21.02	-4	0 / 75
	Dec	471.34	63.75	507.91	75.81	36.57	8	6 / 64
	annual	**502.96**	**29.89**	**536.14**	**41.31**	**33.18**	**7**	**5 / 69**
CAM	Jan	536.46	84.40	425.65	21.22	-110.81	-21	-12 / 71
	Feb	556.75	54.44	576.98	86.91	20.23	4	1 / 72
	Mar	615.27	79.16	600.14	56.29	-15.13	-2	0 / 78
	Apr	579.42	62.50	575.90	26.74	-3.52	-1	2 / 74
	May	552.75	49.06	542.56	44.68	-10.19	-2	0 / 72
	Jun	494.00	50.05	509.61	48.50	15.61	3	4 / 67
	Jul	432.66	55.35	423.16	48.88	-9.50	-2	-3 / 66
	Aug	511.80	44.81	437.08	68.74	-74.72	-15	-7 / 73
	Sep	466.07	41.69	536.66	56.44	70.59	15	7 / 66
	Oct	622.04	73.22	627.14	112.69	5.1	1	3 / 78
	Nov	537.60	48.38	576.35	86.58	38.75	7	5 / 70
	Dec	552.21	118.54	472.49	95.28	-79.72	-14	-11 / 73
	annual	**538.09**	**11.96**	**529.06**	**29.48**	**-9.03**	**-2**	**-1 / 72**
CAS	**annual**	**396.25**	**12.80**	**374.32**	**6.49**	**-21.93**	**-6**	**0 / 61**
EAF	**annual**	**359.15**	**12.56**	**289.73**	**25.04**	**-69.42**	**-19**	**-6 / 61**
EAS	**annual**	**306.24**	**10.85**	**281.10**	**3.65**	**-25.14**	**-8**	**-4 / 51**
NAM	**annual**	**420.48**	**17.36**	**430.25**	**8.33**	**9.77**	**2**	**0 / 56**
NAS	**annual**	**190.74**	**5.90**	**188.43**	**6.72**	**-2.31**	**-1**	**-1 / 30**
NEU	**annual**	**177.78**	**9.60**	**198.31**	**8.97**	**20.53**	**12**	**2 / 31**
SAF	**annual**	**500.87**	**25.06**	**402.56**	**17.08**	**-98.31**	**-20**	**-3 / 71**

Table 4.3: Comparison of ISMAD direct normal irradiance for the years (1995 - 1999) and (2035 - 2039).
Notes:
- Be aware of that these are daily local noon data (for explanation see section 3.2.1).
- The abbreviations of the regions are explained in figure 3.12 on page 60.
- Significance was calculated for annual values. Blue colored cells illustrate a significant decrease of future DNI.
- d refers to the 1995 - 1999 mean number of days with DNI $> 200\,Wm^{-2}$. Δd is the difference between the 2035 - 2039 mean number and the 1995 - 1999 mean number.

ISMAD DNI								
		(1995-1999)		(2035-2039)				
Region	Month	Mean [Wm^{-2}]	STD [Wm^{-2}]	Mean [Wm^{-2}]	STD [Wm^{-2}]	AD [Wm^{-2}]	RD [%]	Δd/d [%]/[%]
	Jan	634.04	75.36	571.14	34.21	-62.90	-10	-2 / 85
	Feb	659.10	51.86	606.46	102.89	-52.64	-8	-2 / 84
	Mar	582.99	128.04	588.72	81.72	5.73	1	1 / 79
	Apr	583.26	50.15	509.24	78.27	-74.02	-13	-1 / 80
	May	593.32	36.70	535.33	40.23	-57.99	-10	0 / 82
	Jun	590.89	43.86	551.54	57.25	-39.35	-7	1 / 90
SAH	Jul	516.29	26.21	467.20	48.68	-49.09	-10	4 / 85
	Aug	465.48	49.34	399.26	40.53	-66.22	-14	2 / 80
	Sep	626.84	41.40	497.18	64.62	-129.66	-21	-6 / 92
	Oct	692.19	71.60	591.00	55.54	-101.19	-15	-6 / 88
	Nov	620.27	67.80	543.85	55.02	-76.42	-12	-4 / 81
	Dec	672.74	62.75	558.67	68.72	-114.07	-17	-7 / 85
	annual	**603.12**	**15.50**	**534.97**	**26.36**	**-68.15**	**-11**	**-2 / 84**
SAS	**annual**	**513.46**	**23.92**	**437.73**	**14.28**	**-75.73**	**-15**	**-2 / 72**
SEA	**annual**	**193.18**	**8.88**	**199.06**	**23.73**	**5.88**	**3**	**2 / 31**
	Jan	276.02	22.12	287.74	40.28	11.72	4	0 / 45
	Feb	330.11	12.90	366.78	42.63	36.67	11	4 / 49
	Mar	396.06	28.59	422.41	38.83	26.35	7	2 / 57
	Apr	431.17	38.68	437.02	29.33	5.83	1	0 / 64
	May	452.34	8.60	480.41	33.48	28.07	6	1 / 72
	Jun	502.85	25.76	537.34	62.49	34.49	7	-1 / 79
SEM	Jul	558.94	29.66	601.61	29.65	42.67	8	0 / 85
	Aug	528.70	32.47	590.45	55.26	61.75	12	1 / 84
	Sep	457.59	30.08	511.46	23.56	53.87	12	3 / 73
	Oct	348.40	37.66	409.90	39.17	61.50	18	3 / 60
	Nov	264.33	26.37	275.16	27.88	10.83	4	1 / 45
	Dec	252.27	22.24	264.65	19.00	12.38	5	3 / 40
	annual	**399.90**	**8.90**	**432.08**	**11.78**	**32.18**	**8**	**1 / 63**
SSA	**annual**	**498.56**	**6.90**	**483.35**	**11.55**	**-15.21**	**-3**	**1 / 66**
(TIB	**annual**	**636.30**	**13.23**	**614.38**	**14.18**	**-21.92**	**-3**	**-1 / 74)**
WAF	**annual**	**344.51**	**12.56**	**263.56**	**19.49**	**-80.95**	**-23**	**-11 / 63**

Table 4.4: Continuation of table 4.3.

5 Summary and Outlook

A method to derive global horizontal and particularly direct normal irradiance from global climate model (GCM) data was presented. Particular emphasis was on ECHAM4 clouds for which an effective optical depth was introduced. Radiative transfer calculations were performed with an atmosphere composite of ECHAM4 clouds and ECHAM5 aerosols. The performed offline calculations were found to be consistent with the online calculations apart from a small systematic deviation of $\approx 10\,\mathrm{Wm}^{-2}$ (5 %). The produced data set has been named ISMAD (**I**rradiances at the **S**urface derived from **M**odeled **A**tmosphere **D**ata). ISMAD provides 6-hourly values of global horizontal and direct normal irradiances for the years 1995 - 1999 and 2035 - 2039. Its spatial resolution is about 3.75° x 3.75°. A comparison between ISMAD local noon irradiances and local noon irradiances derived from satellite measurements (Lohmann, 2006, ISIS) for the years 1995 - 1999 revealed a very good agreement for global mean values: ISMAD GHI is only 2 % smaller than ISIS GHI and ISMAD DNI is 3 % smaller. Nevertheless, the spatially resolved comparison between ISMAD and ISIS irradiances showed significant differences for various regions. These differences could partly be traced back to the distinct aerosols used by the two methods and to systematic errors in the satellite-retrieved ISIS clouds.

According to the ISMAD data set the Saharan region is clearly the region with the most solar resources, GHI as well as DNI. But for the years 2035 - 2039 ISMAD projects a strong reduction of solar resources in Africa compared to the years 1995 - 1999 (significant for DNI in West and Southern Africa). In the Saharan region, where the DESERTEC project actually considers to implement concentrating solar power plants, the reduction of DNI amounts to 11 % (not significant). The reason for this reduction lies in the increasing aerosol optical depth over Africa. In contrast, the smaller aerosol optical depth over Europe leads to larger future irradiances there. In Northern Europe DNI is 12 % larger in the future time period, in Southern Europe and Mediterranean region the increase of DNI amounts to 8 % (not significant). In Australia ISMAD provides higher future irradiances (GHI 5 % and DNI 7 %, not significant). A reduction of clouds could be identified as the cause of this increase. Globally, ISMAD projects 2 % less GHI and 5 % less DNI. This is a result of increased aerosol optical depth (14 %) and slightly higher cloud amount in the future time period.

The validity of the projected changes of solar resources stands and falls with the quality of the clouds and aerosols projected by the climate models. The evaluation of data projected by global climate model simulations covering a future time period is a challenging task and can of course not be a "real" evaluation, i.e. a comparison to measurements. Model performance as well as the likelihood of emission scenarios have to be taken into account (for details see e.g. IPCC (2007, Chapter 8: Climate Models and Their Evaluation)). In IPCC (2007) error intervals of projected atmospheric data are estimated by comparing the results of various climate simulations of different climate models applying distinct emission scenarios. Such an ensemble intercomparison would be required to evaluate ISMAD irradiances.
As was illustrated in this work particularly the preparation as well as the performance of offline radiative transfer calculations with climate model data is very laborious and the presented method to produce suitable cloud data online cannot simply be assigned to other GCMs that may apply other radiation algorithms than ECHAM4. The evaluation of ISMAD irradiances is beyond the scope of this work and must be left to possible further studies. With growing demand for projected direct irradiance data from the side of the energy meteorologists, maybe the radiation codes of global climate models will be replaced by algorithms that can compute direct irradiances online. Then, additional offline calculations will no longer be necessary.

Appendix

A1 Uvspec input file template

uvspec template to calculate irradiances at the surface with climate model input data (ECHAM4 clouds, ECHAM5 aerosols)

RTE SOLVER:
rte_solver rodents # radiative transfer equation solver rodents (Roberts delta-Eddington two-stream)
rte_solver disort2
nstr 6
SPACE AND TIME: (TO CALCULATE SZA)
time 2035 MONTH DAY HOUR 00 00
latitude LAT
longitude LON
SPECTRAL REGION:
wavelength 250 4000 # solar spectrum as used in ECHAM4
MOLECULAR ABSORPTION:
correlated_k fu # correlated-k method fu, 6 spectral bands
output sum
H2O, ALBEDO, ALTITUDE INPUT:
atmosphere_file # giving no atmosphere file means: uvspec chooses a standard atmosphere according to the specified time and location
dens_column H2O H2O_COLUMN # default units: molecules/cm^2
albedo ALB
altitude ALT
AEROSOL INPUT:
aerosol_default
aerosol_species_library OPAC
aerosol_species_file desert # because it's desert regions we are most interested in for CSP
aerosol_set_tau550 TAU_AER
CLOUD INPUT:
wc_file wc.dat
wc_set_tau550 TAU
wc_properties echam4 # use the same optical cloud properties as ECHAM4

wc_cloudcover C_TOT
OUTPUT:
output_user lambda edir edn eup
zout 0 # output altitude above surface in km, here = 0 km
quiet
verbose

A2 Python loop for one year

```
# -*- coding: iso-8859-1 -*-
from pylab import *
from scipy.io.netcdf import *
import os, string
# import subprocess, shutil
import numpy
import time
import math


# Don't forget to insert year in uvspec_template and zenith function below!!!


month_list=[ '01', '02', '03', '04', '05', '06', '07', '08', '09', '10', '11', '12']


for m in month_list:


  # Write number of month into uvspec template
  dummy=os.popen('sed \'s/MONTH/'+str(m)+'/\' uvspec_template.inp > uvspec_template_monthly.inp')
  dummy.close()
  # Open ECHAM5 tau_aerosol_file
  echam_aerosol_file=netcdf_file('../data/ECHAM5/ECHAM5_aero_2035'+str(m)+'.nc', 'r') # insert
  year!!!!
  # Open echam_cloud_file
  echam_cloud_file=netcdf_file('../data/ECHAM4/original_data/Mayerext_inst_85'+str(m)+'_14107.nc',
  'r') # insert year!!!
  # Open echam_geopotential_file
  echam_geopotential_file=netcdf_file('../data/ECHAM4/first_run/uvdata_850101_orig_grid.nc', 'r')


  # Number of latitudes, longitudes, time steps per month
  Nlat=len(echam_cloud_file.variables['lat'][:])
  Nlon=len(echam_cloud_file.variables['lon'][:])
  Ntime=len(echam_cloud_file.variables['time'][:])


  # define gravitational constant [m/s^2] (will be used later):
  g=9.80665 # gravitational constant as used in ECHAM Code


  # Write monthly results to netcdf file
  results=netcdf_file('ISMAD_2035'+str(m)+'.nc', 'w') # insert year!!!
```

results.description='GHI and DNI data set. Offline Calculations out of GCM atmosphere data (clouds,H2O,altitude,albedo of ECHAM4-L39/CHEM/ATTILA; Aerosols of ECHAM5-HAM'
# results.history='Created ' + time.ctime(time.time())
results.createDimension('latitude', Nlat)
results.createDimension('longitude', Nlon)
results.createDimension('time', Ntime)
latitude=results.createVariable('latitude', 'd', ('latitude',))
longitude=results.createVariable('longitude', 'd', ('longitude',))
time=results.createVariable('time', 'd', ('time',))
altitude=results.createVariable('altitude', 'd', ('time', 'latitude', 'longitude',))
albedo=results.createVariable('albedo', 'd', ('time', 'latitude', 'longitude',))
tau_eff=results.createVariable('tau_eff', 'd', ('time', 'latitude', 'longitude',)) # (tau_eff as introduced by B. Mayer (LMU))
tau_eff_max=results.createVariable('tau_eff_max', 'd', ('time', 'latitude', 'longitude',)) # (tau_eff as defined in this work)
tau_aerosol=results.createVariable('tau_aerosol', 'd', ('time', 'latitude', 'longitude',))
c_tot=results.createVariable('c_tot', 'd', ('time', 'latitude', 'longitude',))
H2O_Column=results.createVariable('H2O_Column', 'd', ('time', 'latitude', 'longitude',))
sza=results.createVariable('sza', 'd', ('time', 'latitude', 'longitude',))
ghi_ECHAM=results.createVariable('ghi_ECHAM', 'd', ('time', 'latitude', 'longitude',))
ghi_tau_eff=results.createVariable('ghi_tau_eff', 'd', ('time', 'latitude', 'longitude',))
ghi_tau_eff_max=results.createVariable('ghi_tau_eff_max', 'd', ('time', 'latitude', 'longitude',))
dhi_tau_eff=results.createVariable('dhi_tau_eff', 'd', ('time', 'latitude', 'longitude',))
dhi_tau_eff_max=results.createVariable('dhi_tau_eff_max', 'd', ('time', 'latitude', 'longitude',))
dni_tau_eff=results.createVariable('dni_tau_eff', 'd', ('time', 'latitude', 'longitude',))
dni_tau_eff_max=results.createVariable('dni_tau_eff_max', 'd', ('time', 'latitude', 'longitude',))
net_tau_eff=results.createVariable('net_tau_eff', 'd', ('time', 'latitude', 'longitude',))
net_tau_eff_max=results.createVariable('net_tau_eff_max', 'd', ('time', 'latitude', 'longitude',))
eup_tau_eff=results.createVariable('eup_tau_eff', 'd', ('time', 'latitude', 'longitude',))
eup_tau_eff_max=results.createVariable('eup_tau_eff_max', 'd', ('time', 'latitude', 'longitude',))
latitude.units='degrees_north'
longitude.units='degrees_east'
time.units='day as %Y%m%d.%f'
altitude.units='km'
albedo.units='fraction'
c_tot.units='fraction'
H2O_Column.units='molecules/cm^2'
sza_units =' degrees'
ghi_ECHAM.units =' W/m^2'
ghi_tau_eff.units='W/m^2'
ghi_tau_eff_max.units='W/m^2'
dhi_tau_eff.units='W/m^2'
dhi_tau_eff_max.units='W/m^2'

```
dni_tau_eff.units='W/m2'
dni_tau_eff_max.units='W/m2'
net_tau_eff.units='W/m2'
net_tau_eff_max.units='W/m2'
eup_tau_eff.units='W/m2'
eup_tau_eff_max.units='W/m2'
# ghi_ECHAM.name='global horizontal irradiance of ECHAM4 (E39C-A SCN-B2d)'
ghi_tau_eff.name='global horizontal irradiance at surface calculated by LibRadtran with effective opt. depth'
ghi_tau_eff_max.name='global horizontal irradiance at surface calculated by LibRadtran with max. effective opt. depth and total cloud cover'
dni_tau_eff.name='direct normal irradiance at surface calculated by LibRadtran with effective opt. depth'
dni_tau_eff_max.name='direct normal irradiance at surface calculated by LibRadtran with max. effective opt. depth and total cloud cover'
sza.name='solar zenith angle'
results.variables['latitude'][:]=echam_cloud_file.variables['lat'][:]
results.variables['longitude'][:]=echam_cloud_file.variables['lon'][:]
results.variables['time'][:]=echam_cloud_file.variables['time'][:]


# Now loop over all the ECHAM boxes and the monthly time steps
for i in range(Nlat):


  for j in range(Nlon):
  # zenith function needs longitudes with degrees West positive:
  if(echam_cloud_file.variables['lon'][j]<180.):
  lon_zenith=-echam_cloud_file.variables['lon'][j]
  else:
  lon_zenith=(360.-echam_cloud_file.variables['lon'][j])


  lat=echam_cloud_file.variables['lat'][i]
  lon=echam_cloud_file.variables['lon'][j]
  # print 'lon_zenith', lon_zenith
  # print 'lon', lon


  alt=echam_geopotential_file.variables['surface_geopotential'][0,i,j]/g/1000
  if(alt<0.):
  alt=0.
  alt=round(alt, 1) # we have to round, otherwise problems with vertical resolution of OPAC aerosol
  # print 'alt', alt
  tau_aer=echam_aerosol_file.variables['TAU_2D'][0,i,j]
```

```
# print 'tau_aer', tau_aer
dummy=os.popen('sed \' s/LAT/'+str(lat)+'/\' uvspec_template_monthly.inp
| sed \'s/LON/'+str(lon)+'/\'
| sed \'s/ALT/'+str(alt)+'/\'
| sed \'s/TAU_AER/'+str(tau_aer)+'/\'
> uvspec_template_monthly_boxly.inp ')
dummy.close()


for k in range(Ntime):



  # print 'lat', lat
  # print 'lon', lon  day=k/4+1
  # print 'day', day


  if (k%4==0):
  hour='00'
  elif (k%4==1):
  hour='06'
  elif (k%4==2):
  hour='12' elif (k%4==3):
  hour='18'
  # print k%4
  # print 'hour', hour


  # (only necessary for consistency check with -24 min time shift:)
  #if (hour=='00'):
  # hour_zenith='23'
  # else:
  # hour_zenith=float(hour)-1.
  # print 'hour_zenith', hour_zenith


  cmd='zenith -q -s 0 -a '+str(lat)+' -o '\+str(lon_zenith)+' -y '+str(2035)+' '+str(day)+' '+str(m)+'
  '+str(hour)+' '+str(00)
  dummy=os.popen(cmd, 'r')
  sza=dummy.read()[10:18]
  sza=float(sza)
  # print 'sza', sza # unit: degrees
  # print math.cos(sza*math.pi/180) # math.cos() calculates in radians, therefore: radians=degrees*pi/180
  alb=echam_cloud_file.variables['var175'][k,i,j]
  tau_eff=echam_cloud_file.variables['var76'][k,i,j]
  tau_eff_max=echam_cloud_file.variables['var93'][k,i,j]
```

```
c_tot=echam_cloud_file.variables['var77'][k,i,j]
H2O_column=(echam_cloud_file.variables['var98'][k,i,j]/21600.)*(1000./10000.)*3.34*10**22 # Division by 21600: in ECHAM Code it was forgotten to divide by the 6 hours =21600seconds output interval
# *(1000./10000.)*3.34*10**22: change units from kg/m**2 to molecules/cm**2


results.variables['altitude'][k,i,j]=alt
results.variables['albedo'][k,i,j]=alb
results.variables['tau_eff'][k,i,j]=tau_eff
results.variables['tau_eff_max'][k,i,j]=tau_eff_max
results.variables['c_tot'][k,i,j]=c_tot
results.variables['tau_aerosol'][k,i,j]=tau_aer
results.variables['H2O_Column'][k,i,j]=H2O_column
results.variables['sza'][k,i,j]=sza
# results.variables['ghi_ECHAM'][k,i,j]=echam_cloud_file.variables['var96'][k,i,j]


if (sza>90.): # Don't start radiation calculation when it is dark anyway!


  results.variables['ghi_tau_eff'][k,i,j]=0.
  results.variables['dhi_tau_eff'][k,i,j]=0.
  results.variables['net_tau_eff'][k,i,j]=0.
  results.variables['eup_tau_eff'][k,i,j]=0.
  results.variables['dni_tau_eff'][k,i,j]=0.
  results.variables['ghi_tau_eff_max'][k,i,j]=0.
  results.variables['dhi_tau_eff_max'][k,i,j]=0.
  results.variables['dni_tau_eff_max'][k,i,j]=0.
  results.variables['net_tau_eff_max'][k,i,j]=0.
  results.variables['eup_tau_eff_max'][k,i,j]=0.


else:


  dummy=os.popen('sed \'s/DAY/'+str(day)+'/\' uvspec_template_monthly_boxly.inp
  | sed \'s/HOUR/'+str(hour)+'/'
  | sed \'s/H2O_COLUMN/'+str(H2O_column)+'/\'
  | sed \'s/ALB/'+str(alb)+'/\'
  > uvspec_template_timely_boxly.inp ')
  dummy.close()


  # Do the uvspec run for tau_eff (effective opt. depth for the whole layer as introduced by B. Mayer (LMU)):
```

```
dummy=os.popen('sed \'s/C_TOT/'+str(1)+'/úvspec_template_timely_boxly.inp
| sed \'s/TAU/'+str(tau_eff)+'/\' | ../uvspec', 'r')
uvspec_out1=dummy.read()
edir1=string.atof(uvspec_out1[9:23])
# print 'edir1', edir1
edn1=string.atof(uvspec_out1[24:37])
eup1=string.atof(uvspec_out1[38:51])
ghi1=edir1+edn1
dni1=edir1/math.cos(sza*math.pi/180) # math.cos() calculates in radians, therefore: radi-
ans=degrees*pi/180
net1=ghi1-eup1
results.variables['ghi_tau_eff'][k,i,j]=ghi1
results.variables['dhi_tau_eff'][k,i,j]=edir1
results.variables['dni_tau_eff'][k,i,j]=dni1
results.variables['net_tau_eff'][k,i,j]=net1
results.variables['eup_tau_eff'][k,i,j]=eup1


# Do the uvspec run for tau_eff_max and c_tot: (these results are finally used in this work!)
dummy=os.popen('sed \'s/C_TOT/'+str(c_tot)+'/\' uvspec_template_timely_boxly.inp | sed
\'s/TAU/'+str(tau_eff_max)+'/\' | ../uvspec', 'r')
uvspec_out2=dummy.read()
edir2=string.atof(uvspec_out2[9:23])
edn2=string.atof(uvspec_out2[24:37])
eup2=string.atof(uvspec_out2[38:51])
ghi2=edir2+edn2
dni2=edir2/(math.cos(sza*math.pi/180))
net2=ghi2-eup2
results.variables['ghi_tau_eff_max'][k,i,j]=ghi2
results.variables['dhi_tau_eff_max'][k,i,j]=edir2
results.variables['dni_tau_eff_max'][k,i,j]=dni2
results.variables['net_tau_eff_max'][k,i,j]=net2
results.variables['eup_tau_eff_max'][k,i,j]=eup2


dummy=os.popen('rm uvspec_template_monthly.inp')
dummy=os.popen('rm uvspec_template_monthly_boxly.inp')
dummy=os.popen('rm uvspec_template_timely_boxly.inp')
results.close()
```

What the python loop for a specified year esentially does:
For each month the files containing monthly data of ECHAM4 clouds and ECHAM5 aerosols are opened and a NetCDF file for the results is created. The month is written into the uvspec

template file. Then, a loop over all ECHAM4 latitudes and longitudes is performed to account for every grid box. All values that are the same over the whole month (like latitude and longitude, altitude, aerosol optical depth) are written into the uvspec template. Within the loop over the grid boxes it is looped over all time steps of the month. The cloud cover, effective optical depth, albedo and H_2O-column are additionally given to uvspec for each time step and uvspec is called to perform the calculation of irradiances. Results are successively written to the initially created NetCDF-file. When having finished the calculations for all boxes, the results file is closed and the whole procedure repeats for the next month. It was chosen to loop over time inside the space loop (instead of looping over space inside the time loop) because this way, less input had to be given to uvspec at a single time step. For a given grid box, information about latitude, longitude, aerosol and altitude are the same for every time step within one month and could therefore be written in the uvspec input file before starting the time loop. The other way around only the time would have been the same for all grid boxes and it would have been necessary to read and write more data for every single calculation. Due to the large number of calculations, this would have enlarged computational time.

Bibliography

Albrecht, B. A. (1989). Aerosols, cloud microphysics, and fractional cloudiness. *Science* (245), 1227–1230.

Anderson, G., Clough, S., Kneizys, F., Chetwynd, J. & Shettle, E. (1986). AFGL Atmospheric Constituent Profiles (0-120 km). *AFGL-TR-86-0110, AFGL (OPI), Hanscom AFB, MA 01736* .

Angstroem, A. (1962). Atmospheric turbidity, global illumination and planetary albedo of the earth. *Tellus* (14), 435–450.

Blanco-Muriel, M., Alarcón-Padilla, D. C., López-Moratella, T. & Lara-Coira, M. (2001). Computing the solar vector. *Solar Energy* (70), 431–441.

Bodhaine, B., Wood, N., Dutton, E. & Slusser, J. (1999). On Raighley Optical Depth Calculations. *J. of Atmospheric and Oceanic Technology* **16**, 1854–1861.

Bugliaro, L., Mayer, B., Meerkötter, R. & Verdebout, J. (2006). Potential and limitations of space-based methods for the retrieval of surface UV-B daily doses: A numerical study. *J. Geophys. Res.* **111**.

Chandrasekhar, S. (1960). *Radiative Transfer*. Oxford: Clarendon Press.

Foyntonont, F., Dumortier, D., Heinemann, D., Hammer, A., Olseth, J., Skartveit, A., Ineichen, P., Reise, C., Page, J., Roche, L., Beyer, H., Wald, L. & Santos, A. (1997). *SATELLIGHT: a european programme dedicated to serving daylight data computed from METEOSAT images*. Amsterdam: Proc. LUX-EUROPA'97.

Fröhlich, C. & Lean, J. (1998). The sun's total irradiance: cycles, trends and related climate change. *Geophys. Res. Lett.* **25**, 4377–4380.

Fu, Q. & Liou, K. (1992). On the correlated k-distribution method for radiative transfer in nonhomogeneous atmospheres. *J. Atmos. Sci.* (49), 2139–2156.

Garny, H. (2011). Forschungsbericht 2011-03: Causes and impacts of changes in the stratospheric meridional circulation in a chemistry-climate model. Tech. rep., Deutsches Zentrum für Luft- und Raumfahrt.

Grassl, H. (1975). Albedo reduction and radiative heating of clouds by absorbing aerosol-particles. *Contributions Atmospheric Physics* (48), 199–210.

Hansen, J., Sato, M. & Ruedy, R. (1997). Radiative forcing and climate response. *J. Geophys. Res.* (102), 6831–6864.

Hein, R., Dameris, M., Schnadt, C., Land, C., Grewe, V., Köhler, I., Ponater, M., Suasen, R., Steil, B., Landgraf, J. & Brühl, C. (2001). Results of an interactively coupled atmospheric chemistry-general circulation model: Comparison with observations. *Ann. Geophys.* **19**, 435–457.

Hess, M., Koepke, P. & Schult, I. (1998). Optical properties of aerosols and clouds: the software package OPAC. *Bull. Am. Met. Soc.* **79**, 831–844.

IFS (2008). IFS DOCUMENTATION - Cy33r1 (Operational implementation 3 June 2008). Tech. rep., ECMWF, http: www.ecmwf.int/research/ifsdocs/CY33r1/PHYSICS/IFSPart4.pdf.

IPCC (2001). IPCC Third Assessment Report: Climate Change 2001 (TAR). Tech. rep., International Panel on Climate Change.

IPCC (2007). *Climate Change 2007: the physical science basis: contribution of Working Group I to the Fourth Assessment Report of the Intergovernmental Panel on Climate Change*. Cambridge Univ. Press.

Jones, P. (1999). First- and Second-Order Conservative Remapping Schemes for Grids in Spherical Coordinates. *Mon. Wea. Rev.* **127**, 2204–2210.

Kato, S., Ackermann, T., Mather, J. H. & Clothiaux, E. (1999). The k-distribution method and correlated-k approximation for a shortwave radiative transfer model. *J. Quant. Spectrosc. Radiat. Transfer* (62), 109–121.

Kloster, S., Feichter, J., Maier-Reimer, E., Six, K., Stier, P. & Wtzel, P. (2006). DMS cycle in the marine ocean-atmosphere system - a global model study. *Biogeosci.* **3**, 29–51.

Kraus, H. (2004). *Die Atmosphäre der Erde*. Springer-Verlag.

Kurudz, R. (1992). Synthetic infrared spectra. *Infrared solar physics: proceedings of the 154th Symposium of the International Astronomical Union* , 1365–1368.

Kylling, A., Stmanes, K. & Tsay, S. (1995). A reliable and efficient two-stream algorithm for radiative transfer; Documentation of accuracy in realistic layered media. *J. Atmos. Chem.* **21**, 115.150.

Lacis, A. A. & Oinas, V. (1991). A description of the correlated k distribution method for modeling nongray gaseous absorption, thermal emission, and multiple scattering in vertially inhomogeneous atmospheres. *J. Geophys. Res.* (96), 9027–9063.

Land, C., Ponater, M., Sausen, R. & Roeckner, E. (1999). The ECHAM4.L39(DLR) Atmosphere GCM - Technical Description and Model Climatology. Tech. rep., Deutsches Zentrum für Luft- und Raumfahrt.

Lohmann, S. (2006). *Langzeitvariabilität der globalen und direkten Solarstrahlung für Solarenergieanwendungen*. Ph.D. thesis, Ludwig-Maximilians-Universität München.

Lohmann, U. & Kärcher, B. (2002). First interactive simulations of cirrus clouds formed by homogeneous freezing in the ECHAM general circulation model. *J. Geophys. Res* (107), 4105.

Mayer, B. & Kylling, A. (2005). Technical note: The libRadtran software package for radiative transfer calculations - description and examples of use. *Atmos. Chem. Phys. Discuss.* (5), 1319–1381.

Mayer, R., Hoyer, C., Dietrich, E., Schillings, C., Schroedter, M., Büll, R. & Trieb, F. (2004). Solar Energy Mining: High-Resolution Meteosat-based Service for Solar Radiation Products for Europe, Africa and Asia. In: *Deutsche Gesellschaft für Sonnenenergie e.V. - DGS Munich PSE GmbH - Forschung Entwicklung Marketing*. 14. Intern. Sonnenforum, Freiburg: EuroSun.

McCormic, R. A. & Ludwig, J. H. (1967). Climate modifications by atmospheric aerosols. *Science* (156), 1358–1359.

Meerkötter, R., König, C., Bissoli, P., Gesell, G. & Mannstein, H. (2004). A 14-year European cloud climatology from NOAA/AVHRR data in comparison to surface observations. *Geophys. Res. Letters* **31**, doi:10.1029/2004GL020098.

Meteonorm (2012). www.meteonorm.de.

Meyer, R., Beyer, H., Fanslau, J., Geuder, N., Hammer, A., Hirsch, T., Hoyer-Click, C., Schmidt, N. & Schwandt, M. (2009). Towards Standardization of CSP Yield Assessments. In: *Solar Paces*.

Morcrette, J. (1991). Radiation and cloud radiative properties in the european center for medium range weather forecasts forecasting system. *J. Geophys. Res.* **96**, 9121–9132.

Paltridge, G. & Platt, C. (1976). *Radiative Processes in Meteorology and Climatology*. Elsevier.

Petty, G. W. (2006). *A First Course in Atmospheric Radiation*. Sundog Publishing.

Pierluissi, J. & Peng, G.-S. (1985). New molecular transmission band models for LOWTRAN. *Opt. Eng.* **24**(3), 541–547.

Ponater, M., Marquart, S. & Sausen, R. (2002). Contrails in a comprehensive global climate model: Parameterization and radiative forcing results. *J. Geophys. Res.* **107**.

Reithmeier, C. & Sausen, R. (2002). ATTILA: atmospheric tracer transport in a Lagrangian model. *Tellus* **54**, 278–299.

Renewable Energy Policy Network for the 21st Century (2010). *Renewables 2010, Global Status Report*.

Roeckner, E., Arpe, K., Bengtsson, L., Christoph, M., Claussen, M., Dümenil, L., Esch, M., Giorgetta, M., Schlese, U. & Schulzweida, U. (1996). The atmospheric general circulation model ECHAM-4: Model description and simulation of present-day climate. Tech. Rep. No. 218, Max-Planck-Institut fur Meteorologie.

Roeckner, E., Bäuml, G., Bonaventura, L., Brokopf, R., Esch, M., Giorgetta, M., Hagemann, S., Kirchner, I., Kornblueh, L., Manzini, E., Rhodin, A., Schlese, U., Schulzweida, U. & Tompkins, A. (2003). The atmospheric general circulation model ECHAM5. Tech. Rep. No. 349, Max-Planck-Institut fur Meteorologie.

Roelofs, G.-J., ten Brink, H., Kiendler-Scharr, A., de Leeuw, G., Mensah, A., Minikin, A. & Otjes, R. (2010). Evaluation of simulated aerosol properties with the aerosol-climate model ECHAM5-HAM using observations from IMPACT field campaign. *Atmos. Chem. Phys.* **10**, 7709–7722.

Rossow, W. & Garder, L. (1993). Validation of ISCCP cloud detections. *J. Climate* **6**, 2370–2393.

Rothmann, L. & et al. (1992). HITRAN molecular database: Editions of 1991 and 1992. *J. Quant. Spectros. Radiat. Transfer* **48**, 469–507.

Räisänen, P. (1997). Effective Longwave Cloud Fraction and Maximum-Random Overlap of CLouds: A problem and a Solution. *Monthly Waether Rev.* **126**, 3336–3340.

Sato, M., Hansen, J., McCormick, M. & Pollack, J. (1993). Stratospheric aerosol optical depths. *J. Geophys. Res.* **98(D12)**, 22987–22994.

Scharmer, K., Greif, J., Page, J., Dogniaux, R., Czeplak, G., Terzenbach, U., Bernhardt, I., Wald, L., Antoine, S., Bauer, O., Beaudoin, L., Beyer, H., Francois, E., Lefevre, M., Poloubinski, N., Rigollier, C., Lund, H., Möller-Jensen, J., Joukoff, A., Temples, J., Borisenko, E., Tsvetkov, A., Aguiar, R., Carvalho, M., Collares Pereira, M., Littlefair, P., Albuisson, M., Bourges, B. & Kadi, L. (2000). *The European Solar Radiation Atlas*, vol. Vol. 1-2 +CD. Paris: Les Presses de l'Ecole des Mines.

Steil, B., Dameris, M., Brühl, C., Crutzen, P., Grewe, V., Ponater, M. & Sausen, R. (1998). Development of a chemistry module for GCMs: first results of a multiannual integration. *Ann. Geophys.* **16**, 205–228.

Stenke, A., Dameris, M., Grewe, V. & Garny, H. (2009). Implications of Lagrangian transport for simulations with a coupled chemistry-climate model. *Atmos. Chem. Phys.* **9**, 5489–5504.

Stier, P., Feichter, J., Kinne, S., Kloster, S., Vignati, E., Wilson, J., Ganzewald, L., Tegen, I., Werner, M., Balkanski, Y., Schulz, M., Boucher, O., Minikin, A. & Petzold, A. (2005). The aerosol-climate model ECHAM5-HAM. *Atmos. Chem. Phys.* **5**, 1125–1156.

Stier, P., Feichter, S., Roeckner, E., Kloster, S. & Esch, M. (2006). The evolution of the global aerosol system in a transient climate simulation from 1860 to 2100. *Atmos. Chem. Phys.* **6**, 3059–3076.

Stubenrauch, C., Rossow, W., Cheruy, A., Chedin, A. & Scott, N. (1999). Clouds as seen by satellite sounders (3I) and imagers (ISCCP). Part I: Evaluation of cloud parameters. *J. Climate* **12**, 2189–2213.

Sundqvist, H. (1978). A parameterization scheme for non convective condensation including prediction of cloud water content. *Q. J. R. Meteorol. Soc.* **104**, 677–690.

Tanré, D., Geleyn, J.-F. & Slingo, J. (1984). *Aerosols and Their Climatic Effects*, chap. First results of the introduction of an advanced aerosol-radiation interaction in the ecmwf low resolution global model. pp. 133–177.

Tegen, I., Hollrig, P., Chin, M., Fung, I., Jacob, D. & Penner, J. (1997). Contribution of different aerosol species to the global aerosol extinction optical thickness: Estimates from model results. *J. Geophys. Res.* **102 (D20)**, 23895–23915.

Thomas, G. E. & Stamnes, K. (1999). *Radiative Transfer in the Atmosphere and Ocean*. Cambridge Univ. Press.

Twomey, S. (1974). Pollution and the planetary albedo. *Atmos. Environ.* (8), 1251–1256.

Twomey, S. (1977). The Influence of Pollution on the Shortwave Albedo of Clouds. *J. Atmos. Sci.* (34), 1149–1152.

Wapler, K. (2007). Forschungsbericht 2007-11: Der Einfluss des dreidimensionalen Strahlungstransports auf Wolkenbildung und -entwicklung. Tech. rep., Deutsches Zentrum für Luft- und Raumfahrt, Institut für Physik der Atmosphäre, Oberpfaffenhofen.

Warren, S., Hahn, C., London, J., Chervin, R. & Jenne, R. (1996). Global distribution of total cloud cover and cloud type amounts over land. *DOE/ER/60085-H1, NCAR/TN-273 + STR* .

Wielicki, B. & Parker, L. (1992). On the determination of cloud cover from satellite sensors: The effect of sensor spatial resolution. *J. Geophys. Res.* **97**, 12799–12823.

Wild, M., Ohmura, A., Gilgen, H. & Roeckner, E. (1998). The disposition of radiative energy in the global climate system: GCM-calculated versus observational estimates. *Climate Dynamics* **14**, 853–869.

Yang, P., Liou, K., Wyser, K. & Mitchell, D. (2000). Parameterization of the scattering and absorption properties of individual ice crystals. *J. Geophys. Res.* (105), 4699–4718.

Zdunkowski, W., Trautmann, T. & Bott, A. (2007). *Radiation in the Atmosphere*. Cambridge Univ. Press.

Unless otherwise indicated in the text or references, or acknowledged above, this thesis is entirely the product of my own scholarly work.

Ich versichere, die Arbeit selbstständig angefertigt und dazu nur die im Literaturverzeichnis angegebenen Quellen benutzt zu haben.

München, den 14. April 2012